Curvilinear Structure Enhancement in Biomedical Images

CIGDEM SAZAK

SAZAK, CIGDEM (2019) Curvilinear Structure Enhancement in Biomedical Images. Doctoral thesis, Durham University.

Curvilinear Structure Enhancement in Biomedical Images

Çiğdem Sazak

A thesis presented for the degree of
Doctor of Philosophy at Durham University

Department of Computer Science
Durham University
United Kingdom

14th March 2019

Dedications

To my better half, who enlighten my entire life with his unwavering love. To the selfless hero who stood by my side and gave me a strength I never knew I had.

To my beloved husband “***Emre Can Turgut***”

***

To whose love, friendship, hope and earning an honest living for our day and night make me able to get such an accomplishment and honour.

To my kindhearted king, my father “***Ahmet Sazak***”.

***

To whose the paradise beneath her feet. To the most ambitious person who was the ultimate source of motivation and inspiration. A strong and gentle soul who taught me to trust in Allah, believe in hard work and that so much could be done with little.

To my role model in this life, my mother “***Gŭlfiye Sazak***”.

***

To who make me feel powerful beyond my limits, and astonish me with a stunning love and endless support.

To my sweetheart sister “***Aycan Sazak***”.

To the light of my eyes, my adorable big sister, “***Özlem Sazak***”.

***

To every individual who was generously supportive .. I dedicate this achievement to each one of you, with love.

Curvilinear Structure Enhancement in Biomedical Images

Çiğdem Sazak

Submitted for the degree of Doctor of Philosophy
July 2018

Curvilinear structures can appear in many different areas and at a variety of scales. They can be axons and dendrites in the brain, blood vessels in the fundus, streets, rivers or fractures in buildings, and others. So, it is essential to study curvilinear structures in many fields such as neuroscience, biology, and cartography regarding image processing. Image processing is an important field for the help to aid in biomedical imaging especially the diagnosing the disease. Image enhancement is the early step of image analysis.

In this thesis, I focus on the research, development, implementation, and validation of 2D and 3D curvilinear structure enhancement methods, recently established. The proposed methods are based on phase congruency, mathematical morphology, and tensor representation concepts.

First, I have introduced a 3D contrast independent phase congruency-based enhancement approach. The obtained results demonstrate the proposed approach is robust against the contrast variations in 3D biomedical images.

Second, I have proposed a new mathematical morphology-based approach called the bowler-hat transform. In this approach, I have combined the mathematical morphology with a local tensor representation of curvilinear structures in images. The bowler-hat transform is shown to give better results than comparison methods on challenging data such as retinal/fundus images. The bowler-hat transform is shown to give better results than comparison methods on challenging data such as retinal/fundus images. Especially the proposed method is quite successful while enhancing of curvilinear structures at junctions.

Finally, I have extended the bowler-hat approach to the 3D version to prove the applicability, reliability, and ability of it in 3D.

Declaration

The work in this thesis is based on research carried out Department of Computer Science, University of Durham, United Kingdom. No part of this thesis has been submitted elsewhere for any other degree or qualification and it is all my own work unless referenced to the contrary in the text.

Note on Publications Included in this Thesis

At the time of submission, four Chapters of this thesis had been submitted for publication or published in journals.

Chapter 4

Chapter 5

Chapter 6

Chapter 7

These Chapters are presented as published, although referencing and notation has been altered and cross-referencing added for consistency throughout this thesis. Some stylistic changes have been made for consistency. The majority of the text is verbatim; however, additions to the body of text are included along with footnotes and, where appropriate. The Chapter 4 to Chapter 7 and can be considered self-contained since they have been written in the style of papers/proceedings.

The implementation, literature review and writing for Chapter 5 (*p.* 55) and Chapter 6 (*p.* 86) were completed in partnership with Carl J. Nelson and for the Chapter 7 (*p.* 103) with Shuaa S. Alharbi. Also, Carl J. Nelson helps to revise and supervise the Chapter 7 (*p.* 103). All other aspects of this research, including implementation, data analysis and writing, were carried out by the author.

Chapter 5 Çiğdem Sazak and Carl J. Nelson contributed equally to this work. Çiğdem Sazak, Carl J. Nelson and Boguslaw Obara are with the Department of Computer Science, Durham University, Durham, UK. Çiğdem Sazak is funded by the Turkey Ministry of National Education.

Chapter 7 Çiğdem Sazak and Shuaa S. Alharbi.contributed equally to this work. Çiğdem Sazak, Shuaa S. Alharbi, and Boguslaw Obara are with the Department of Computer Science, Durham University, Durham, UK. Çiğdem Sazak is funded by the Turkey Ministry of National Education.

Çiğdem Sazak is funded by the Turkey Ministry of National Education for all the research presented in this thesis.

Acknowledgements

El hamdulillah, I wholeheartedly praise and thank ALLAH (SWT), the Almighty, for HIS uncountable blessings, I am thoroughly thankful to ALLAH (SWT) to giving me the strength and power to keep going on this research, allow me to see my thesis go through, and making my dream come true. Maybe my name is written on the front cover of this work, however, doesn't mean that I am the only one who contributes. There are many people behind this piece of work who deserve to be both acknowledged and thanked here. First and foremost, I am very fortunate and grateful to my supervisor, Dr. Boguslaw Obara, who has meticulously supported me throughout my study with his patience, continuous guidance, knowledge, suggestions and astute criticism. I am extremely grateful to my husband Emre, my beloved parents, sister Aycan who have been a constant source of love, my friend Adnan to his inspiration and encouragement during the challenges of my PhD life. My sincere gratitude to the rest of my family and friends everywhere, who were always encouraging me in all of my pursuits. I especially acknowledge one of my best friend who is Sibel because of her patient and extraordinary support. I convey my sincere appreciation and respect for my colleagues, without whom my ambition could not be accomplished.

Contents

List of Figures

List of Tables

List of Acronyms

SE	Structuring Element
SN	Sensitivity
SP	Specificity
SF	Structuring Function
1D	One-Dimensional
2D	Two-Dimensional
3D	Three-Dimensional
4D	Four-Dimensional
N**D**	N-Dimensional
US	Ultrasonography
CT	Computed Tomography
MR	Magnetic Resonance
MRA	Magnetic Resonance Angiography
RVR	Regularised Volume Ratio
PCT	Phase Congruency Tensor
ROC	Receiver Operating Characteristic
AUC	Area Under the Curve
ACC	Accuracy
LoG	Laplacian of Gaussian
BHT	Bowler Hat Transform
DRIVE	Digital Retinal Images for Vessel Extraction
STARE	STructured Analysis of the REtina
CLAHE	Contrast Limited Adaptive Histogram Equalisation
X-RAY	Energetic High-Frequency Radiation
MTHT	Multiscale Top-Hat Tensor
DIADEM	Digital Reconstruction of Axonal and Dendritic Morphology
RORPO	Ranking the Orientation Responses of Path Operators
RWTH	Rheinisch-Westfalische Technische Hochschule

Chapter 1

Introduction

Prologue

In this Chapter, I have introduced biomedical imaging and image enhancement concepts followed by the thesis outline.

1.1 Introduction

In this thesis, I have investigated a wide range of biomedical image enhancement approaches [4–11], especially the approaches focused on the curvilinear or curvilinear structures enhancement. These approaches are designed to work with a wide range of biomedical images and to be robust against the noise and varying intensity across the image.

I have studied mainly, phase congruency [10, 12], mathematical morphology [13–15] and tensor-based [16] approaches. In this thesis, first, I present an extension of the phase congruency tensor approach proposed in [10], which explores the phase congruency concept combined with the tensor representation of an image to enhance curvilinear structures in 3D biomedical images [17] in Chapter 4. Second, I introduce a novel use of combined mathematical morphology structuring elements

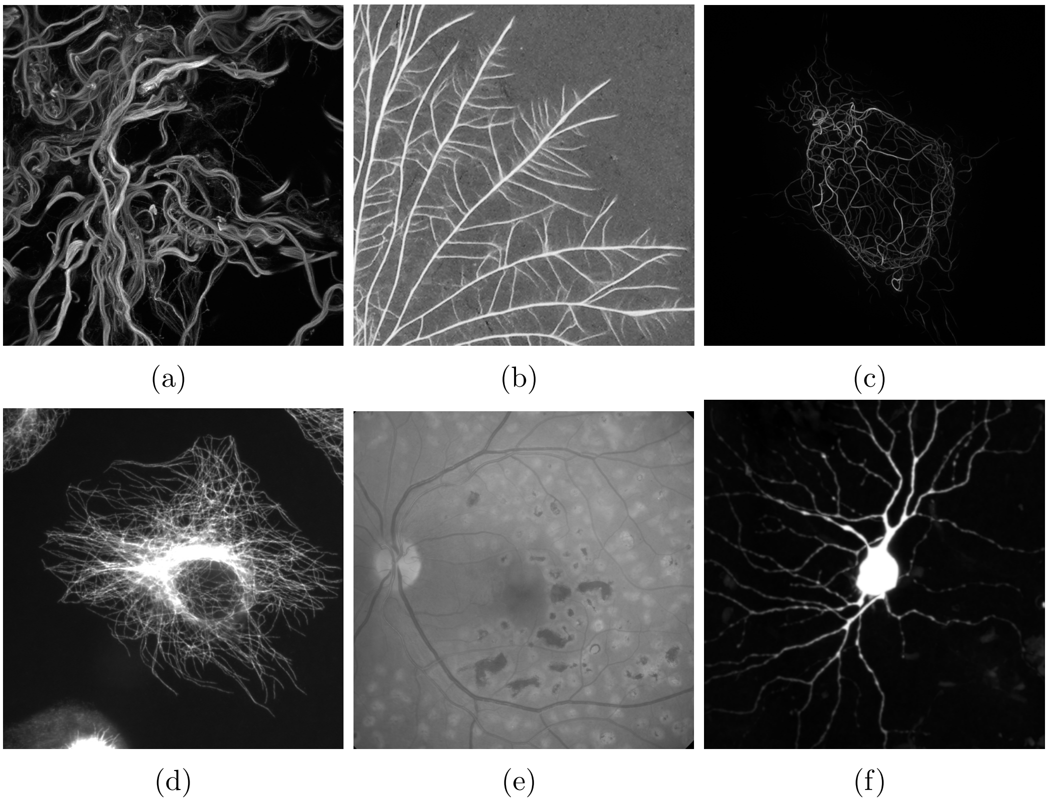

Figure 1.1: Biomedical imaging can help to observe curvilinear structures; (a) is a collagen network (provided by Dr. Tim Hawkins, Durham University, UK), (b) is a fungal network [1], (c) is a keratin network in skin cell (provided by Dr. Tim Hawkins, Durham University, UK), (d) is a microtubules network in plant cell [2], (e) is a vascular network (HRF dataset [3]), (f) is a neuronal network (image provided by Dr. Chris Banna, UC Santa Barbara, USA).

for the enhancement of curvilinear structures in 2D biomedical imaging [18], particularly retinal imaging in Chapter 5. Third, I extend the proposed mathematical morphology-based approach into [19] 3D see Chapter 6. Finally, I develop a novel 2D and 3D curvilinear structures enhancement method based on a combination of mathematical morphology top-hat transforms with the tensor representation of an image, see Chapter 7.

Before diving into details of the new proposed approaches, I present a review of the state-of-the-art image enhancement methods in the Chapter 2.

1.2 Biomedical Image Analysis

A wide range of biomedical imaging techniques are being used to image biomedical curvilinear structures, including: optical microscopy [20], scanning probe microscopy [21], electron microscopy [22], X-Ray [23], computed tomography [5], magnetic resonance [24], ultrasonography [25], optical coherence tomography [26], etc., to date (see Figure 1.1). These imaging technologies constantly improve the quality of image data captured in terms of format, type, size, resolution, and quantity [27]. To handle such biomedical image data, fully or partly automate image processing, analysis, quantification, and visualisation approaches are needed [28, 29].

In general, biomedical image analysis divides into few categories such as: image registration [30] (see Figure 1.2), image enhancement [17] (see Figure 1.3), image segmentation [31, 32], image classification [33], objects quantification, and objects visualisation [34]. In this thesis, I focus on image enhancement, specially strengthening and enrichment of curvilinear structures in grayscale images (see Figure 1.3)

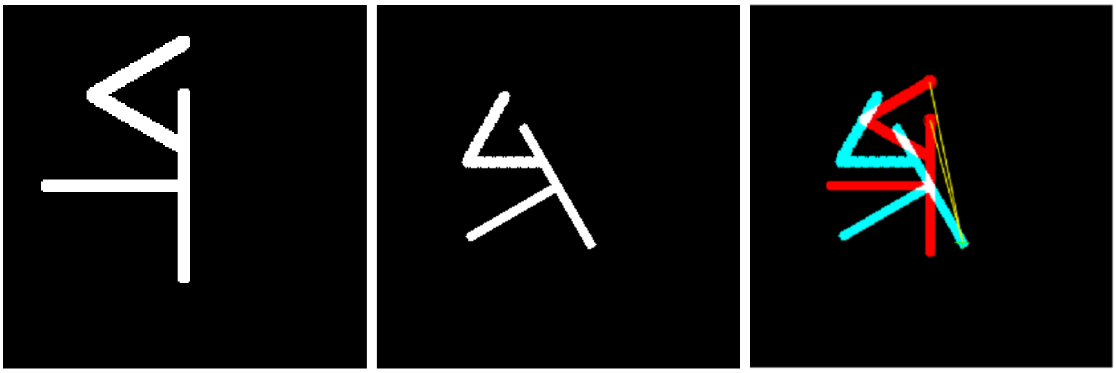

(a) Original (b) Rotated and scaled (c) Matched points

Figure 1.2: Registration of two binary images; (a) is original image and (b) is an affine transform of (a). (c) illustrates matched feature points from (a) (red) and (b) (green) used for the image registration.

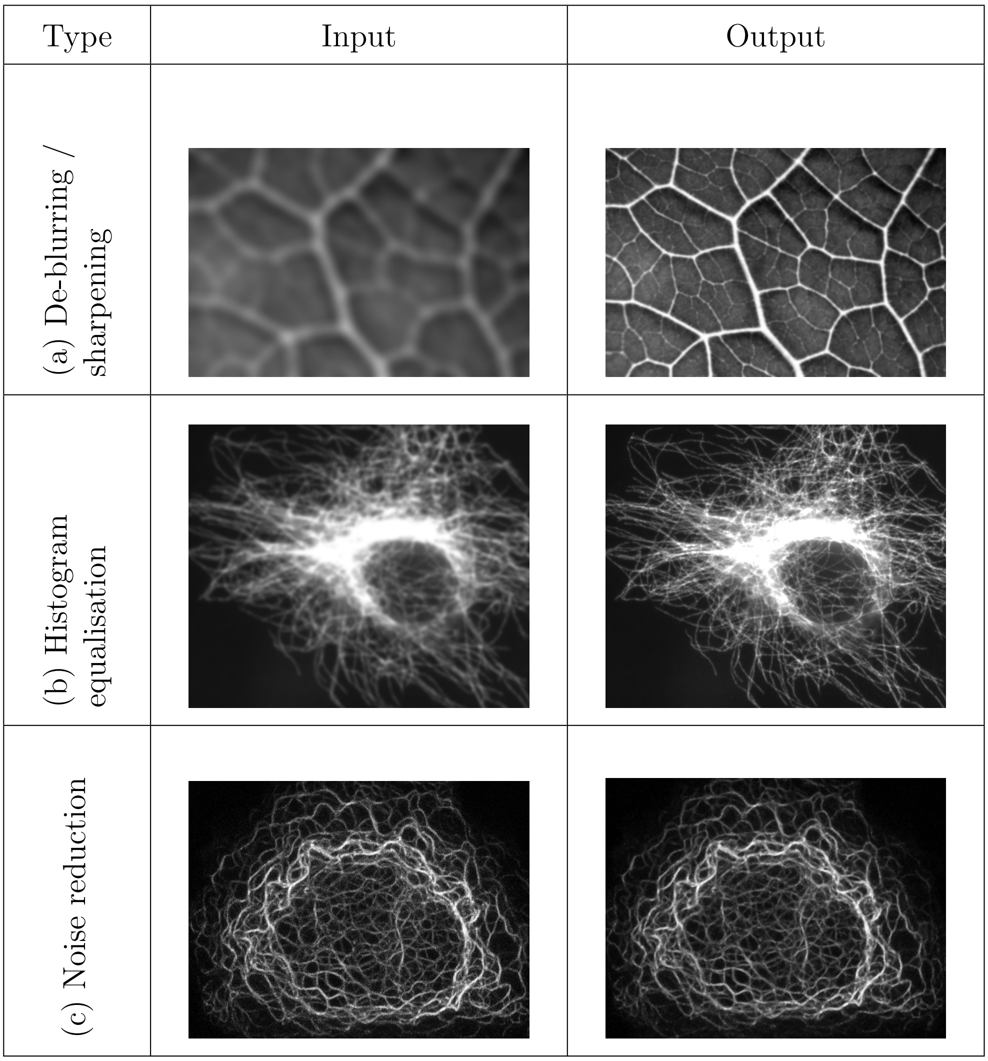

Figure 1.3: Curvilinear structure enhancement approaches can improve visualisation, detection and quantification of curvilinear structures by: (a) deblurring/sharpening image (leaf veins network image from [10]), (b) histogram equalisation (microtubules network image from [2]), (c) noise reduction (cytoskeletal network in a skin cell image provided by Prof. Dr. Med. Rudolf Leube, Institute of Molecular and Cellular Anatomy, RWTH Aachen University, Germany).

1.3 Image Enhancement

Any biomedical image data may suffered from a wide rang of imaging problems such as high noise [35, 36], low contrast [37], high intensity variation [38], or overlapping objects (when working with 2D image representation of 3D real structure, see Figure 1.4). In most of the cases, an image enhancement approach is often an early stage in the image analysis work-flow [39].

In general, image enhancement has been widely used in image processing to improve the quality of an image and increase human observation [40]. It aims to aid human interpretation and automated quantitative analyses of features/objects in the image [39]. It can improve image quality by reducing noise, enhancing particular features, and reducing intensity variations; see Figure 1.3.

In this thesis, I propose a set of novel image enhancement approaches for curvilinear features enhancement in 2D and 3D images. These approaches are robust against the loss of signals at curvilinear feature junctions, unwanted enhancement of non-curvilinear features, and difficulty in dealing with the intrinsically multiscale nature of curvilinear features in biological images.

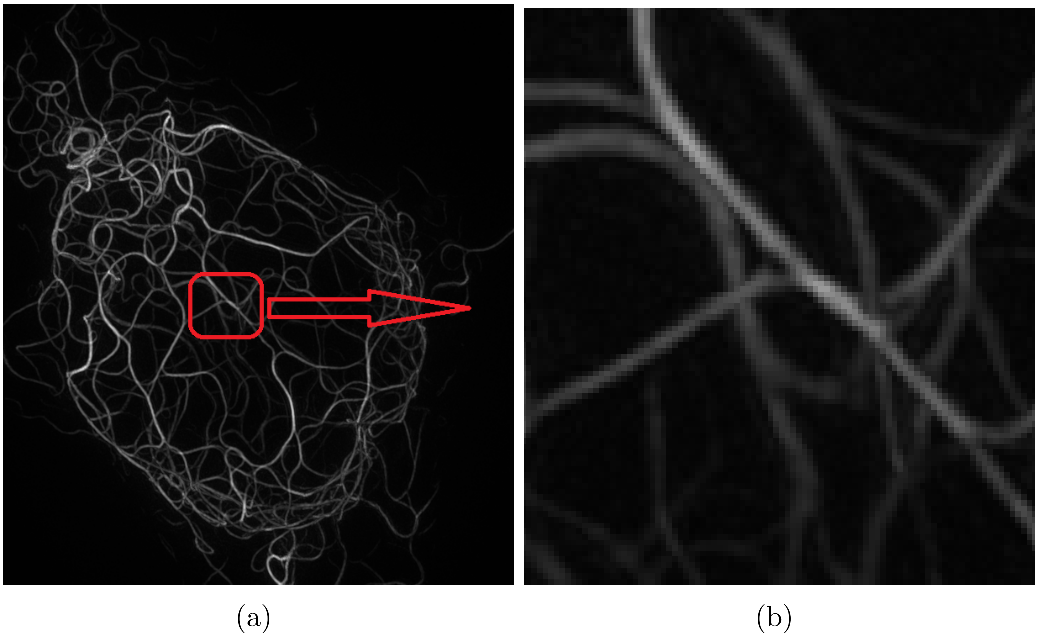
(a) (b)

Figure 1.4: Overlapping curvilinear structures can be complicated and challenging for curvilinear feature enhancement, especially when deciding which vessel belongs to which branch. (a) is a 2D max projection of a 3D keratin network in a skin cell provided by Dr. Tim Hawkins, Durham University. The red box indicates a region with overlapping vessels, which is shown in greater detail in (b).

1.4 Overview of Thesis and Research Contributions

This thesis is divided as follows:

Chapter 2 : In this Chapter, I provide the background knowledge of the existing methods related to the enhancement of curvilinear features in the literature. I demonstrate what kind of challenges the current approaches faced so far in 2D and 3D. These methods are also used as comparator methods.

Chapter 4 : Here, I propose a 3D extension of the contrast independent phase congruency-based approach to enhance 3D curvilinear structures based on oriented phase congruency concept, called 3D Phase Congruency Tensor. I illustrate that the proposed method is mostly insensitive to intensity variations along the curvilinear structures and provides successful enhancement within noisy regions.

Chapter 3 : In this Chapter, I introduce basic concepts behind mathematical morphology, including morphological erosion, dilation, opening, closing, and top-hat transform.

Chapter 5 : In this Chapter, I introduce the bowler-hat transform, a new approach based on mathematical morphology for curvilinear structures enhancement. The proposed method combines different mathematical morphology structuring elements to detect natural features of curve-like structures. In this Chapter, I propose an extension of the bowler-hat transform-based method to 3D. The proposed 3D approach combines two different 3D mathematical morphology structuring elements. It is robust at curvilinear structures junctions and able to cope with variations in thickness throughout complex curvilinear networks.

Chapter 7 : In this Chapter, I propose the Multiscale Top-Hat Tensor (MTHT) approach, which combines multiscale morphological filtering with a local tensor representation of curvilinear structures in 2D and 3D images. I then propose MTHT equivalent representations of the commonly used curvilinear measures, such as vesselness and neuriteness.

Chapter 8 : Finally, I summarise this thesis, highlighting the main contributions to the image enhancement research field and suggest possible future work for extending the use of mathematical morphology and tensor representation concept to other image processing and analysis problems in the biological and medical imaging domains.

Chapter 2

Previous Research Work on Curvilinear Feature Enhancement Techniques

Prologue

This Chapter presents an overview of curvilinear feature enhancement concepts in biomedical images.

2.1 Introduction

The enhancement, detection, and quantification of different types of structures/features in 2D and 3D images is a very popular challenge in image processing applications in astronomy [42], aerial and satellite imaging [43], material sciences [44], and biology and medicine [30, 45–47].

A wide range of biomedical curvilinear structures, including vessels [48, 49], cancer spicule [50], and cytoskeleton network [51] and may more, are enhanced, detected, and then analysed using a stream of image processing approaches [9, 52–54]. In

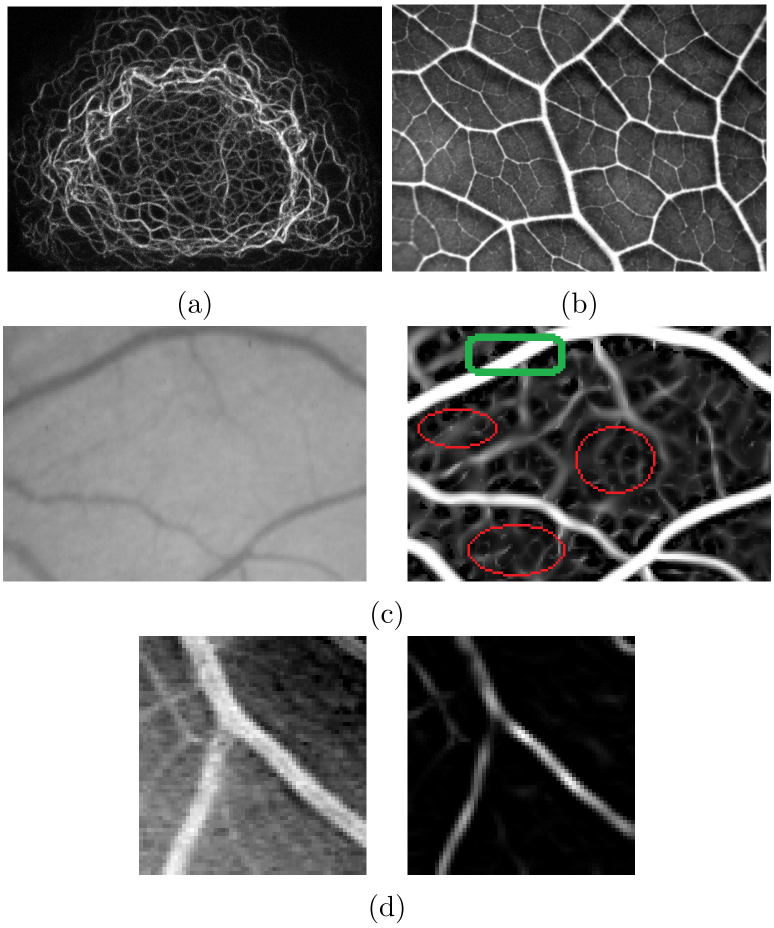

(a) (b)

(c)

(d)

Figure 2.1: Some of the challenges faced by state-of-the-art curvilinear structure enhancement methods include: (a) high level of noise (cytoskeletal network in a skin cell image provided by Prof. Dr. Med. Rudolf Leube, Institute of Molecular and Cellular Anatomy, RWTH Aachen University, Germany), (b) uneven background illumination (leaf veins network image from [10]), (c) introduction of false curvilinear structures by the enhancement methods (*e.g.* Regularized Volume Ratio approach [9]; vascular network image from [41]); red circles indicate the false vessels and green square indicates the true vessel, (d) enhancement at junctions (*e.g.* vesselness approach [4]; a vascular network image from DRIVE dataset [41]).

general, image processing researchers focus on the development of faster, more robust and more reliable approaches for processing. All the up-to-date methods have their advantages and disadvantages with the respect of their performance, complexity, implementation, and computational performance [55].

This Chapter aims to provide a comprehensive review of existing curvilinear features enhancement methods, starting from conventional Gaussian derivatives-based methods [4] and finishing with phase congruency-based methods [56].

2.1.1 Curvilinear Structures Enhancement Challenges

In general, any novel curvilinear structure enhancement approach must deal with the following challenges we face in the biomedical images: inhomogeneous background, high noise level, low contrast/intensity, junctions, and multiscale characteristic [4, 35, 57, 58] (see Figure 2.1).

2.2 Literature Review

In the following Section, I review existing image processing approaches for curvilinear structures enhancement in images. My aim is to highlight the weakness and strengths of these approaches.

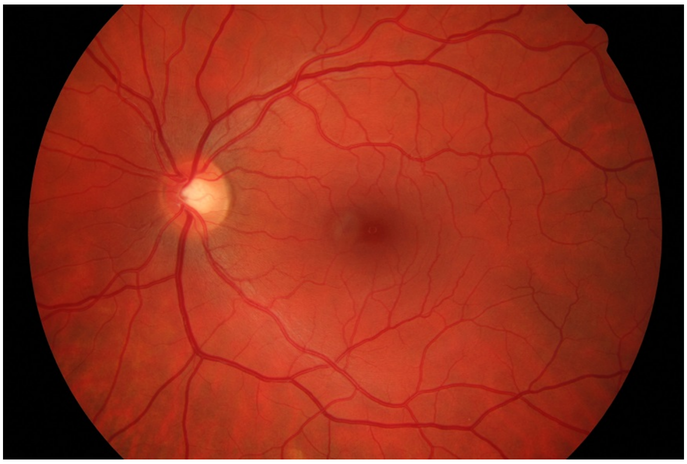

Figure 2.2: Curvilinear structures can be present in different sizes in the biomedical images. An image is shown here, a vascular network from HRF dataset [3].

2.2.1 Multiscale Concept in Image Processing

Since curvilinear structures in biomedical images can also appear in different scales/sizes (see Figure 2.2), a multiscale concept for curvilinear structures enhancement has been extensively investigated in the literature [4, 5, 7, 57, 59].

In order to enhance, detect and then quantify structures in images, at both low and high spatial frequencies, images are processed at different scales either by altering the image size or by altering the filter size [60] (*e.g.* using a concept in [61]).

There are many different fields definitions of the multiscale concepts, such as, time [47, 62], information complexity [63], signal frequency [64], smoothing degree [65], or scale space [66, 67], among others.

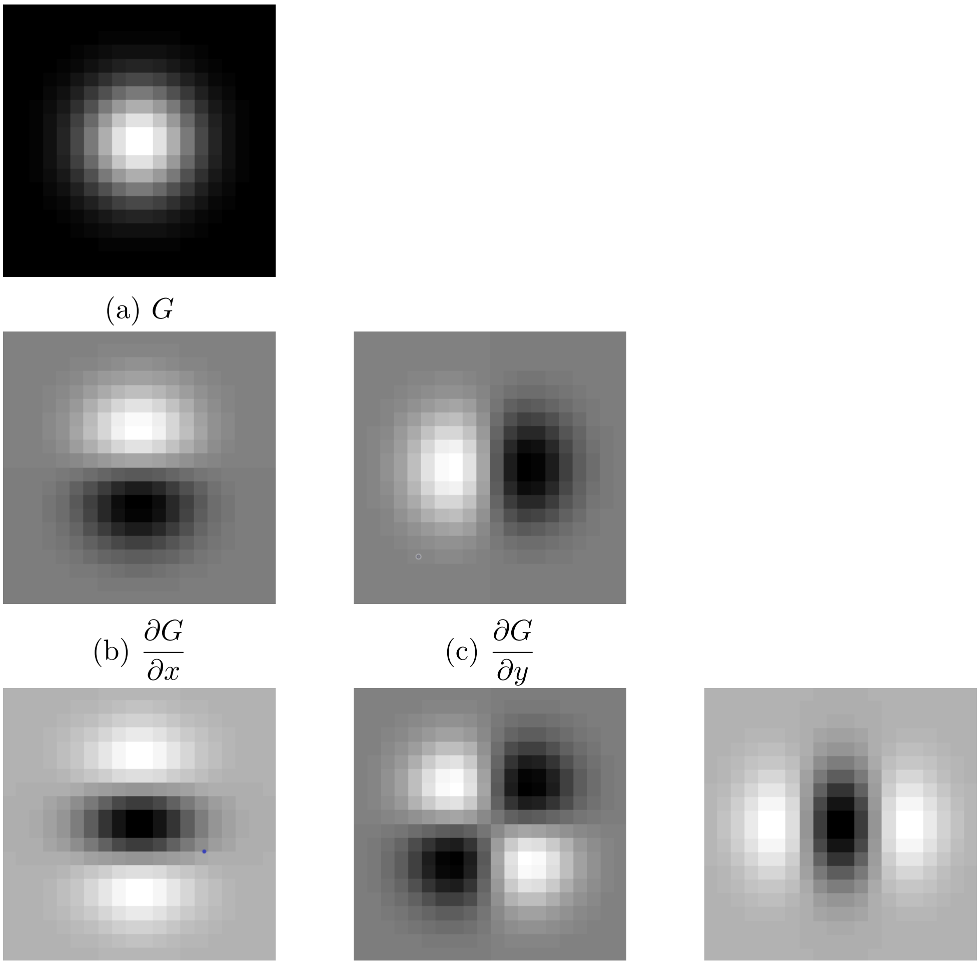

(a) G

(b) $\frac{\partial G}{\partial x}$

(c) $\frac{\partial G}{\partial y}$

(d) $\frac{\partial^2 G}{\partial x^2}$

(e) $\frac{\partial^2 G}{\partial x \partial y}$

(f) $\frac{\partial^2 G}{\partial y^2}$

Figure 2.3: Two dimensional Gaussian kernels up to 2^{nd} order derivatives. (a) a 2D Gaussian kernel G, the first order Gaussian partial derivative in x (b) and y (c); second order Gaussian partial derivatives in xx (d), xy (e), and yy (f).

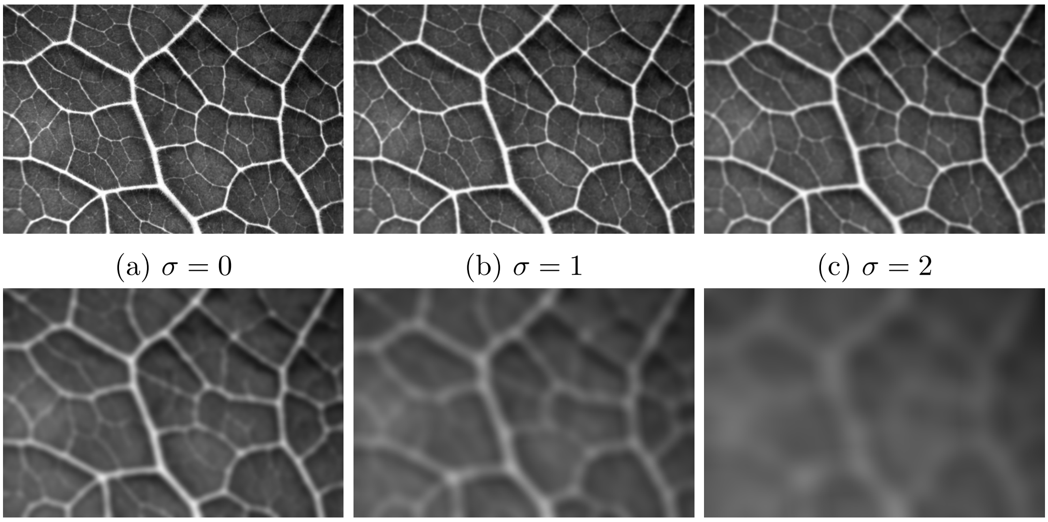

(a) $\sigma = 0$ (b) $\sigma = 1$ (c) $\sigma = 2$

(d) $\sigma = 4$ (e) $\sigma = 8$ (f) $\sigma = 16$

Figure 2.4: Gaussian scale space representation of the image (leaf veins network image from [10]). The scale space is formed by convolving the original image (a) with a Gaussian kernel of increasing standard deviation (ranging in $\sigma = 0, 1, 2, 4, 8, 16$).

Scale space

Curvilinear features can be observed in various sizes / scales in images [4]. The essential idea is to insert the original image inside a group of progressively smoothed images, in which fine-scale details are successively suppressed. This approach is usually accomplished by the use of Gaussian filters, or their derivatives (see Figure 2.3), with multiple scales obtained by varying the standard deviation σ (see Figure 2.4). Such multiscale concept is used in a wide range of image enhancement approaches, including wavelets decomposition [68], time-evolving snakes [69, 70], increasing smoothing [71, 72], steerable filters [7].

For a given 3D image $I_\sigma(\vec{p})$ and given scale σ, the neighbourhood of a point $\vec{p}$ can be estimated by its Taylor expansion;

$$I_\sigma(\vec{p} + \Delta\vec{p}) \approx I_\sigma(\vec{p}) + \Delta\vec{p}^T \nabla I_\sigma(\vec{p}) + \Delta\vec{p}^T H_\sigma(\vec{p}) \Delta\vec{p}, \tag{2.1}$$

where $H_\sigma(\vec{p})$ is the Hessian matrix, a tensor of second order partial derivatives of I

at point $\vec{p}$ and scale σ. Δ is a gradient operator. In three dimensions, a spherical neighbourhood met at the point $\vec{p}$ is outlined by $H_\sigma(\vec{p})$ over an ellipsoid whose axes are along the eigenvectors $\mathbf{v}_{\sigma,i}$ of the Hessian and the respective semi-lengths are the magnitudes of the eigenvalues $\lambda_{\sigma,i}$. Therefore, the detection of curvilinear structures can be performed by an analysis of the eigenvalues and eigenvectors. Two of the most well-known ways in this area that have been called vesselness [4] and neuriteness [8].

2D			**3D**			
λ_1	λ_2	Structure	λ_1	λ_2	λ_3	Structure
L	L	Background	L	L	L	Background
L	H-	Bright curve	L	L	H-	Bright sheet
L	H+	Dark curve	L	L	H+	Dark sheet
H-	H-	Bright blob	L	H-	H-	Bright tubular
H+	H+	Dark blob	L	H+	H+	Dark tubular
			H-	H-	H-	Bright blob
			H+	H+	H+	Dark blob

Table 2.1: 2D and 3D local image structure representation by the Hessian matrix-based eigenvalues (L low, H+ high positive, H- high low).

2.2.2 Hessian-based Methods

In [4], Frangi *et al.* introduced a novel Hessian-based multiscale concept for 2D curvilinear/3D tubular structure enhancement in images. They construct the Hessian matrix using second-order Gaussian derivatives. The eigenvectors and eigenvalues of the Hessian matrix then define the principal directions of local image features. These can then be combined to form different measures of vesselness or blobness [73] in biomedical images.

2D Vesselness

The $\lambda_{1,2}$ eigenvalues are defined by the elements of the Hessian matrix calculated for a given image I;

$$H = \begin{bmatrix} H_{11} & H_{12} \\ H_{12} & H_{22} \end{bmatrix} = \begin{bmatrix} \dfrac{\partial^2 I}{\partial x^2} & \dfrac{\partial^2 I}{\partial x \partial y} \\ \dfrac{\partial^2 I}{\partial x \partial y} & \dfrac{\partial^2 I}{\partial y^2} \end{bmatrix}. \tag{2.2}$$

Then eigenvalues can be calculated by the use of H_{ij} and $(i, j) \in [1, 2]$, such that;

$$\lambda_{1,2} = \frac{1}{2}\left(H_{11} + H_{22} \pm \sqrt{\left(H_{11} - H_{22}\right)^2 + 4H_{12}^2}\right). \tag{2.3}$$

For curvilinear structures, *i.e.* elongated, smooth structures, I define the following eigenvalue relationship;

$$\lambda_2 \gg \lambda_1, \tag{2.4}$$

If the magnitude of both eigenvalues is small, *i.e.* the local image structure is likely to be background. If one eigenvalue is small and the other large then the local image structure is likely to be a curvilinear feature. Finally, if both eigenvalues are high, then the local image structure is likely to be blob-like feature.

Initially, vesselness measurement, exploring relationships of the eigenvalues, was proposed by Frangi and colleagues [4] as follows;

$$\mathcal{V}_o = \begin{cases} 0 & \text{if } \lambda_2 > 0, \\ \left(e^{-\dfrac{\mathcal{R}_{\mathcal{B}}^2}{2\beta^2}}\right)\left(1 - e^{-\dfrac{\mathcal{S}^2}{2c^2}}\right) & , otherwise \end{cases}, \tag{2.5}$$

where

$$\mathcal{R}_{\mathcal{B}} = \lambda_1/\lambda_2, \quad \mathcal{S} = \sqrt{\lambda_1^2 + \lambda_2^2}, \tag{2.6}$$

where generally β is fixed to 0.5 and c is equal to half of the maximum Frobenius norm ($\mathcal{S}$). This approach, however, leads to a failure at the intersection of curvilinear features as both eigenvalues have similarly large values leading to a vesselness measure close to zero. Thus, curvilinear structures at junctions can be lost at the segmentation stage and therefore curvilinear network connectivity may be lost [74]. An extension of this approach can be found in [75] where a multiscale filter is combined with multiscale Hessian measurement to enhance the curvilinear features and reduce noise.

3D Vesselness

Vesselness measure [4] can be defined for 3D images by using 3D Hessian matrix;

$$H = \begin{bmatrix} H_{11} & H_{12} & H_{13} \\ H_{21} & H_{22} & H_{23} \\ H_{31} & H_{32} & H_{33} \end{bmatrix} = \begin{bmatrix} \frac{\partial^2 I}{\partial x^2} & \frac{\partial^2 I}{\partial x \partial y} & \frac{\partial^2 I}{\partial x \partial z} \\ \frac{\partial^2 I}{\partial x \partial y} & \frac{\partial^2 I}{\partial y^2} & \frac{\partial^2 I}{\partial y \partial z} \\ \frac{\partial^2 I}{\partial x \partial z} & \frac{\partial^2 I}{\partial y \partial z} & \frac{\partial^2 I}{\partial z^2} \end{bmatrix}. \tag{2.7}$$

3D vesselness measure is defined as;

$$V_0 = \begin{cases} 0, & \lambda_2, \lambda_3 < 0 \\ \left(e^{-\frac{R_\beta^2}{2\beta^2}}\right)\left(1 - e^{-\frac{R_\alpha^2}{2\alpha^2}}\right)\left(1 - e^{-\frac{S^2}{2c^2}}\right), & \text{otherwise} \end{cases}, \tag{2.8}$$

where

$$S = \sqrt{\lambda_1^2 + \lambda_2^2 + \lambda_3^2}, \quad R_\beta = \frac{\lambda_1}{\sqrt{\lambda_2 \lambda_3}}, \quad R_\alpha = \frac{|\lambda_2|}{|\lambda_3|}.$$

R_β ratio indicates tubular features. R_α ratio that $\lambda_2 \approx \lambda_3$ and thus helps to discriminate between plate-like and line-like structures. Lastly, S evaluates whether the eigenvalues are large compared to noise. α, β and c are real positive parameters that are user-defined. Several 2D and 3D image structure models have been used to express the relationships between the eigenvalues [6], see Table 2.1.

2D Neuriteness

As an alternative to vesselness measurement of Frangi, Meijering and colleagues [8] introduce a neuriteness measurement to enhance low contrast and highly inhomogeneous curvilinear structures in biomedical images. Using a modified Hessian matrix, with a tuning parameter, and a new combination of eigenvalues, neuriteness infers putative curvilinear features in the image. A modified Hessian matrix, H', is defined as follows;

$$H' = \begin{bmatrix} H_{11} + \alpha H_{22} & (1-\alpha)H_{12} \\ (1-\alpha)H_{12} & H_{22} + \alpha H_{11} \end{bmatrix}, \tag{2.9}$$

where α is a tunable parameter, to calculate a measure of neuriteness such that,

$$N = \begin{cases} \dfrac{\lambda_{\max}}{\lambda_{\min}} & \text{if} \quad \lambda_{\max} < 0 \\ 0 & \text{if} \quad \lambda_{\max} \geq 0 \end{cases}, \tag{2.10}$$

where

$$\lambda_{\max} = \max(|\lambda_1{}'|, |\lambda_2{}'|), \tag{2.11}$$

$$\lambda_{\min} = \min(\lambda_{\max}), \tag{2.12}$$

$$\lambda_1^{'} = \lambda_1 + \alpha\lambda_2, \tag{2.13}$$

$$\lambda_2^{'} = \lambda_2 + \alpha\lambda_1, \tag{2.14}$$

where $\lambda_i^{'}$ are the normalized eigenvalues of H'; $\lambda_{\max}$ is the largest eigenvalue at each pixel; and $\lambda_{\min}$ the smallest value of all $\lambda_{\max}$ [8]. In the neuriteness measurement, background intensity discontinuities that are immune to first order derivatives are suppressed by the use of second-order derivatives, since the first-order derivative reacts wherever there is a discontinuity in intensity level.

3D Neuriteness

Neuriteness measure was extended into 3D with use of 3D second-order modified Hessian matrix [76];

$$H^{'} = \begin{bmatrix} H_{11} + \frac{\alpha}{2}H_{22} + \frac{\alpha}{2}H_{33} & (1-\alpha)H_{12} & (1-\alpha)H_{13} \\ (1-\alpha)H_{12} & H_{22} + \frac{\alpha}{2}H_{11} + \frac{\alpha}{2}H_{33} & (1-\alpha)H_{23} \\ (1-\alpha)H_{13} & (1-\alpha)H_{23} & H_{33} + \frac{\alpha}{2}H_{11} + \frac{\alpha}{2}H_{22} \end{bmatrix}, \quad (2.15)$$

where α is a parameter whose optimal value will be chosen such that the equivalent steerable filter in [77]. The 3D neuriteness measurement is defined as;

$$\lambda_{\max} = \max(|\lambda_1{}'|, |\lambda_2{}'|, |\lambda_3{}'), \quad (2.16)$$

$$\lambda_{\min} = \min(\lambda_{\max}), \quad (2.17)$$

$$\lambda_1^{'} = \lambda_1 + \alpha\lambda_2 + \alpha\lambda_3, \quad (2.18)$$

$$\lambda_2^{'} = \lambda_2 + \alpha\lambda_1 + \alpha\lambda_3, \quad (2.19)$$

$$\lambda_3^{'} = \lambda_3 + \alpha\lambda_1 + \alpha\lambda_2. \quad (2.20)$$

A major failing for the neuriteness measure is that background noise signals are enhanced as if they are curvilinear structures (see Figure 2.1c). In the original paper [8] this is solved with a tracing stage; however, as an enhancer only, this can cause serious problems for further analysis. The neuriteness measure also leads to a failure at the intersection of vessels as both eigenvalues have similarly large values leading to a neuriteness measure close to zero (see Figure 2.8). A further example of their work is found in [78].

Regularized Volume Ratio

Recently, Jerman and colleagues [9] proposed a new Hessian-based curvilinear feature enhancement method, which is able to resolve the drawbacks found in most of the previous Hessian-based methods, which are directly proportional to λ_2 2D and

3D or λ_3 (3D only). These drawbacks are: 1. eigenvalues are non-uniform throughout and an elongated or rounded structure that has uniform intensity; 2. eigenvalues vary with image intensity; and 3. curvilinear structure enhancement is not uniform across scales. Jerman *et al.* [9] attempt to solve this by modifying the vesselness to indicate elongated structures, such as vessels, and regularising λ_3 (where $\lambda_3 = \lambda_2$ in 2D) to ensure robustness to low magnitude changes, *e.g.* noise in regions of uniform intensity. The 2D version of the method is defined as;

$$\mathcal{V}_P = \begin{cases} 0 & \text{if } \lambda_2 \leq 0 \vee \lambda_\rho \leq 0 \\ 1 & \text{if } \lambda_2 \geq \lambda_\rho/2 > 0 \\ \lambda_2^2(\lambda_\rho - \lambda_2)\left(\frac{3}{\lambda_2+\lambda_\rho}\right)^3 & \text{otherwise} \end{cases}, \tag{2.21}$$

where λ_ρ is the regularised form of λ_2, and is calculated;

$$\lambda_\rho(s) = \begin{cases} \lambda_2 & \text{if } \lambda_2 > \tau \max_{\vec{p}} \lambda_2(\vec{p}, s) \\ \tau \max_{\vec{p}} \lambda_2(\vec{p}, s) & \text{if } 0 < \lambda_2 \leq \tau \max_{\vec{p}} \lambda_2(\vec{p}, s) \\ 0 & \text{otherwise} \end{cases}, \tag{2.22}$$

for scale s, where τ is a cut-off threshold between zero and one and for any pixel $\vec{p} = (x, y)$. A major issue of this method is the false vessel effect and noise sensitivity (see Figure 2.1c). Throughout this thesis, I refer to this approach as the RVR.

2.2.3 Phase Congruency

A major issue with many image enhancement methods is that they depend on image intensity and, therefore, fine, and usually lower intensity, vessels may be missed. To address this issue a contrast-independent method, based on Phase Congruency (PC), was introduced in [56]. A 2D phase congruency tensor-based approach for curvilinear structures enhancement was proposed by [10] and then extended to 3D by [17].

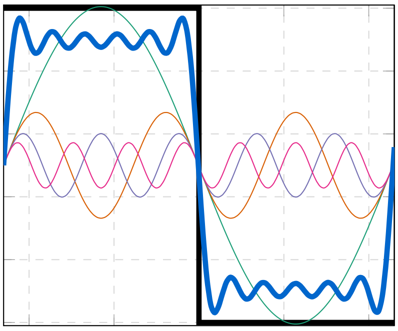

Figure 2.5: First four Fourier series (green, pink, purple and orange) of a 1D square wave signal (bold black) and the sum of them (bold blue).

Phase Congruency based Methods

In image processing, phase congruency is intensity- and contrast-independent feature metric that can be used for edge, corner and other feature detection. Phase congruency relies on the feature phases in the frequency domain of the image (Figure 2.5). Features such as edges and corners, many frequency components are in phase regardless of the contrast between foreground and background in the intensity domain.

2D Phase Congruency For the calculation of the local phase is needed a quadrature pair of filters which are polar separable filters. To obtain localised frequency information, Gabor filters are the most popular option. Gabor filters were first presented in [79], then used as a traditional choice of quadrature filters. These filters provide the best simultaneous localization of spatial and frequency information. Though, they have two main constraints. The maximum bandwidth of a Gabor filter is limited to around one octave and Gabor filters are not optimal if one is endeavouring broad spectral information with maximal spatial localization. Another choice to the Gabor function is the log-Gabor function proposed by [80]. log-Gabor filters can be created with arbitrary bandwidth and the bandwidth can be optimised to produce a filter with minimal spatial extent. Since then, log-Gabor filters have been chosen as a quadrature filters. So, let assume that $I(\vec{p})$ is a given image where

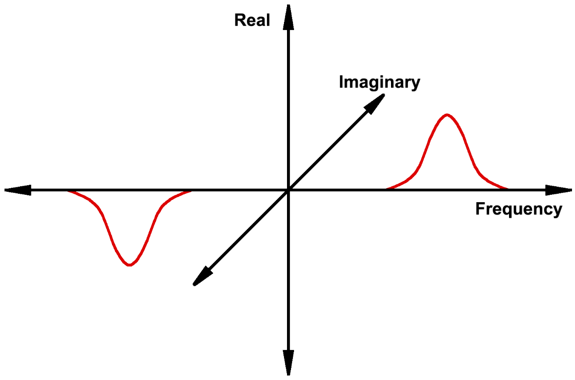

(a) Even filter

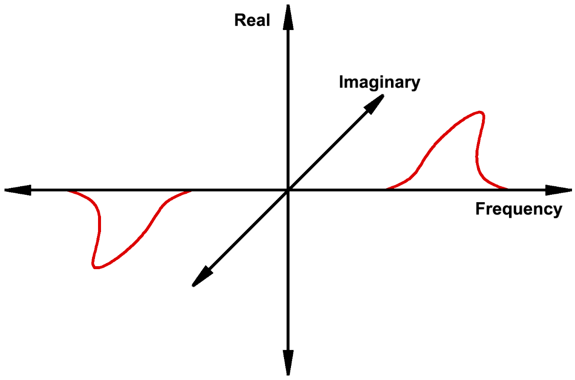

(b) Odd filter

Figure 2.6: Even (a) and odd (b) symmetric filter transfer function used to calculate the phase congruency.

$\vec{p} = (x, y)$ is a specific pixel position, and a quadrature pair of even, $F^e_{s,\theta}$, and odd, $F^o_{s,\theta}$ (see Figure 2.6), filters at scale s and orientation θ. The response vector is a given by its even and odd components $e_{s,\theta}(\vec{p})$ and $o_{s,\theta}(\vec{p})$;

$$\left[e_{s,\theta}\left(\vec{p}\right), o_{s,\theta}\left(\vec{p}\right)\right] = \left[I\left(\vec{p}\right) * F^e_{s,\theta}, I\left(\vec{p}\right) * F^o_{s,\theta}\right]. \tag{2.23}$$

The amplitude of the s^{th} component is defined as;

$$A_{s,\theta}\left(\vec{p}\right) = \sqrt{e_{s,\theta}\left(\vec{p}\right)^2 + o_{s,\theta}\left(\vec{p}\right)^2}, \tag{2.24}$$

and the local phase is given by;

$$\varphi_{s,\theta}\left(\vec{p}\right) = atan\left(\frac{o_{s,\theta}\left(\vec{p}\right)}{e_{s,\theta}\left(\vec{p}\right)}\right). \tag{2.25}$$

The oriented log-Gabor filter in the frequency domain can be determined in polar coordinates as the product of two components,

$$\hat{G}(\omega,\theta) = e^{\left(-\frac{\left(\log\left(\frac{\omega}{\omega_0}\right)\right)^2}{2\log\left(\frac{\sigma_\omega}{\omega_0}\right)}\right)}.e^{\left(-\frac{(\theta-\theta_0)^2}{2\sigma_\theta}\right)}, \tag{2.26}$$

where ω_0 is central radial frequency of filter and σ_ω is the standard deviation controlling the filter bandwidth in [80]. θ is the orientation of the filter and σ_θ determines the angular spread.

Mathematically in 2D case, I define the phase congruency, $PC_s(\vec{p})$, for a set of scale, s, over several orientations, θ and at a specific pixel, $\vec{p} = (x, y)$, as;

$$PC_s(\vec{p}) = \sum_\theta PC_{s,\theta}(\vec{p}), \tag{2.27}$$

where $PC_{s,\theta}(\vec{p})$, the phase congruency for each orientation, is defined as;

$$PC_\theta(\vec{p}) = \frac{\sum_s W_s(\vec{p})\lfloor A_{s,\theta}(\vec{p})\Delta\varphi_{s,\theta}(\vec{p}) - t\rfloor}{\sum_s A_{s,\theta}(\vec{p}) + \epsilon}. \tag{2.28}$$

Here $A_{s,\theta}(\vec{p})$ is the amplitude of the image component at scale s, t is a noise reducing threshold and ϵ a small factor to prevent division by zero. Here $\lfloor . \rfloor$ is defined as;

$$\lfloor f(x)\rfloor = \begin{cases} f(x) & f(x) >= 0 \\ 0 & \text{otherwise} \end{cases}. \tag{2.29}$$

The phase deviation, $\Delta\varphi_{s,\theta}(\vec{p})$, quantifies the difference between the phase at scale s, $\varphi_{s,\theta}(\vec{p})$, and the mean phase over all scales, $\bar{\varphi}_\theta(\vec{p})$, such that;

$$\Delta\varphi_{s,\theta}(\vec{p}) = \left|\cos\left(\varphi_{s,\theta}(\vec{p}) - \bar{\varphi}_{\theta}(\vec{p})\right) - \sin\left(\varphi_{s,\theta}(\vec{p}) - \bar{\varphi}_{\theta}(\vec{p})\right)\right|. \tag{2.30}$$

Finally, $W(\vec{p})$ is a sigmoid weighting term penalising narrow frequency regions based on γ and c, gain and cut-off, respectively, $A_{\max}(\vec{p})$, which is the maximum response over all scales and S, the total number of scales. Mathematically;

$$W_s(\vec{p}) = \left(1 + e^{\gamma\left(c - \frac{1}{S}\left(\frac{\sum_s A_s(\vec{p})}{A_{\max}(\vec{p}) + \epsilon}\right)\right)}\right). \tag{2.31}$$

Phase Congruency Tensor-based Methods

The Phase Congruency Tensor (PCT) is built upon PC principles, but the tensor is decomposed [10]. For a given set of scales s and a given set of phase congruency measures $PC_s(\vec{p}, \theta)$ for each orientation θ, the proposed phase congruency tensor is;

$$T_{PC_s}(\vec{p}) = \sum_{\theta} PC_s(\vec{p}, \theta)(\vec{n}_\theta \vec{n}_\theta^T), \tag{2.32}$$

where $\vec{n}_\theta$ is the normalised column vector for each orientation and $\alpha = 1/N - 1$, with N is the image dimensionality.

The eigenvalues of the tensor can then be used in the same way as the Hessian matrix eigenvalues are used in Equations (2.5) and (2.10) to define PCT-neuriteness and PCT-vesselness. An extension of this method into 3D has recently been shown in [17] (for the detailed steps of the phase-based tensor see Figure 2.7).

A major drawback of the PC-based concept is the complexity of its parameter space. Moreover, as with Hessian-based measures, the PCT-based measures also lead to a failure at the intersection of curvilinear structures as both eigenvalues have similar, large values leading to PCT-based vesselness and neuriteness measures close to zero (see Figure 2.8).

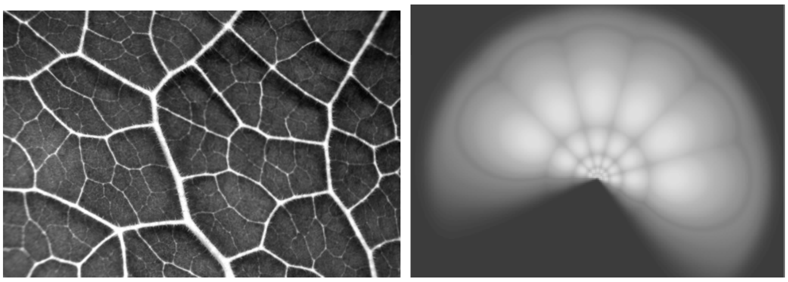

(a) Input (b) log-Gabor filter

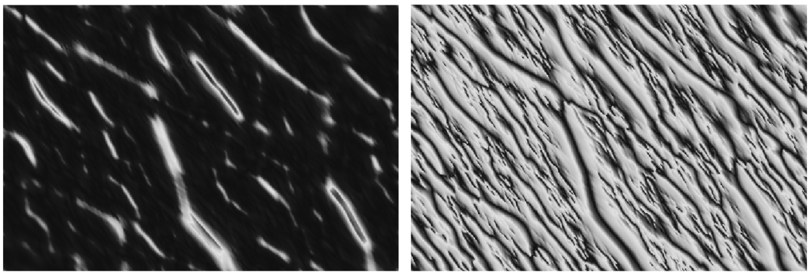

(c) F^o(odd) (d) F^e (even)

(e) PC_1 (f) PC_2 (g) PC_3

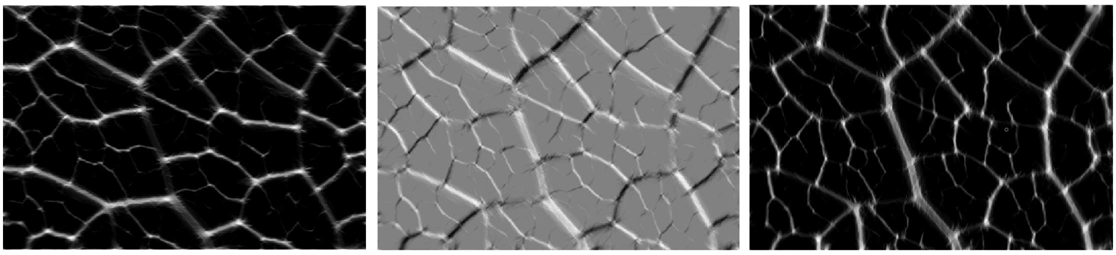

(h) PCT_{xx} (i) PCT_{xy} (j) PCT_{yy}

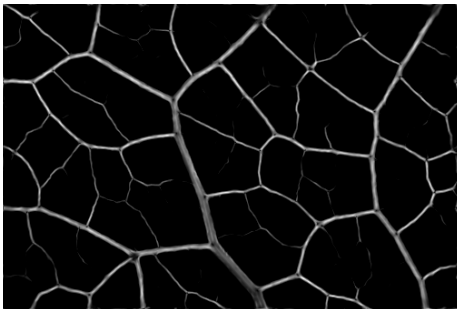

(k) PCT-neuriteness

Figure 2.7: Step by step explanation of the Phase Congruency Tensor. A leaf vein network image [10] is used as an input and is shown in (a). (b) a bank of log-Gabor filters for 6 scales and 6 orientations, (c, d) odd and even filter responses for 3^{rd} scale and 3^{rd} orientation, (e-g) phase congruency for first 3 scales, (h-j) phase congruency tensor components, (k) phase congruency tensor-based neuriteness.

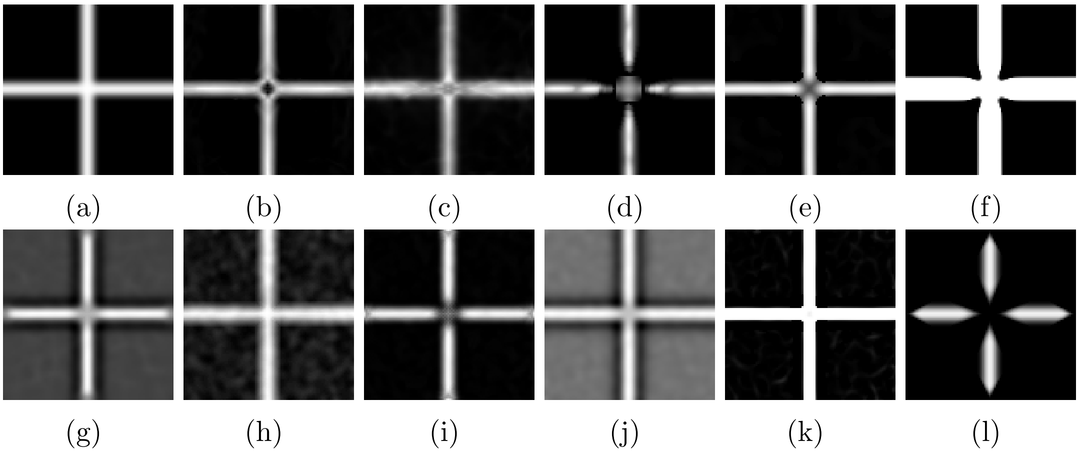

Figure 2.8: Lost of the curvilinear structure enhancement methods response at the junction. (a) an input image. Results for: (b) PCT-neuriteness, (c) PCT-vesselness, (d) vesselness, (e) neuriteness, (f) SCIRD-TS, (g) line detector, (h) CLAHE, (i) Zana's top-hat, (j) wavelet, (k) volume ratio, (l) RORPO. Since both eigenvalues have similar values at the junction, it leads to any of the tensor-based methods failure at the junctions.

2.2.4 Adaptive Histogram Equalisation-based Methods

Contrast Limited Adaptive Histogram Equalisation (CLAHE), proposed by [81], is widely used for curvilinear structures enhancement. In this simple, histogram-based method an image is first divided into small regions, each of which then undergoes a histogram equalisation. To avoid over-enhancement of noise, a contrast limiting procedure is applied between regions. Further development of this method is demonstrated in [82] where CLAHE is combined with an anisotropic diffusion filter to smooth the image and preserve vessel boundaries. A major drawback of this method is noise sensitivity (see Figure 2.9).

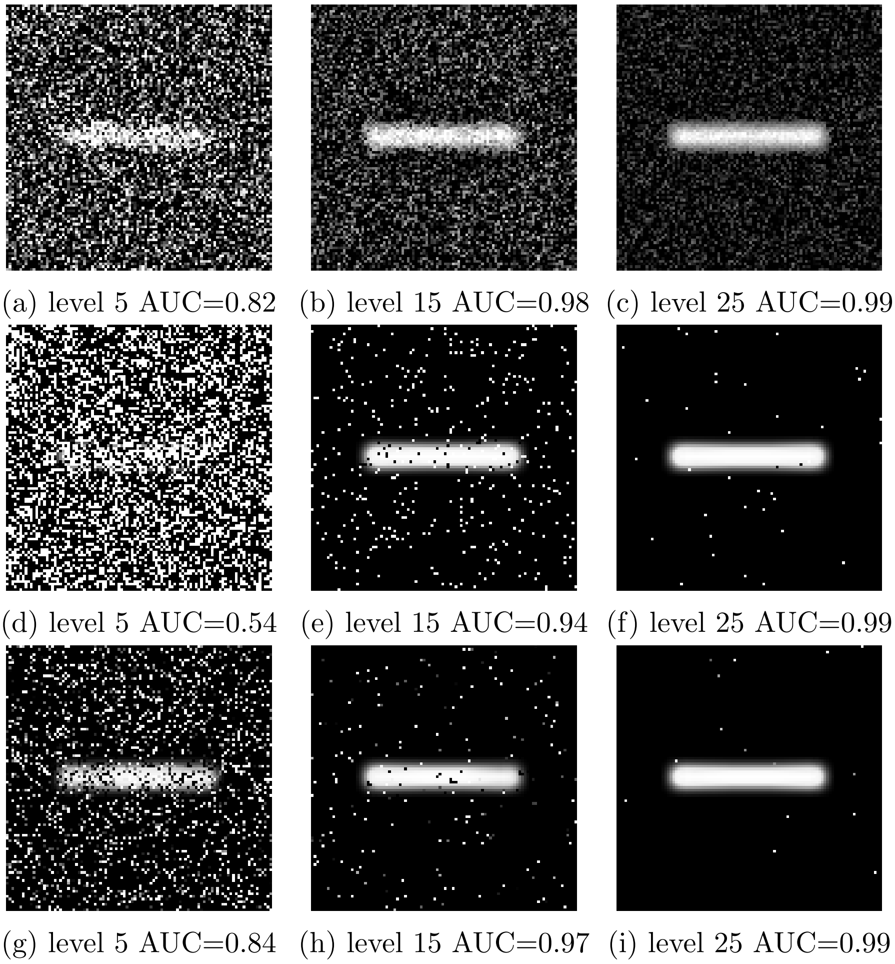

(a) level 5 AUC=0.82 (b) level 15 AUC=0.98 (c) level 25 AUC=0.99

(d) level 5 AUC=0.54 (e) level 15 AUC=0.94 (f) level 25 AUC=0.99

(g) level 5 AUC=0.84 (h) level 15 AUC=0.97 (i) level 25 AUC=0.99

Figure 2.9: Demonstration of the effect of different types and levels of noise on the performance of curvilinear structures enhancement using CLAHE approach. (a to c) demonstrate additive Gaussian noise, (d to f) show salt and pepper noise, (g to i) illustrate speckle noise.

2.2.5 Wavelet Transform-based Enhancement Methods

Bankhead and colleagues [11] proposed the use of wavelets for curvilinear structure enhancement and segmentation. They calculate anisotropic, undecimated wavelet transform using the cubic B-spline mother wavelet, and employ the coefficients to the threshold steps for enhancement, followed by vessel segmentation (see the workflow in Figure 2.10 for detailed steps). Further improvement of this approach is demonstrated in [83] where multi-orientation and multiscale features from the vessel filtering and the wavelet transform stages are combined and then used for training

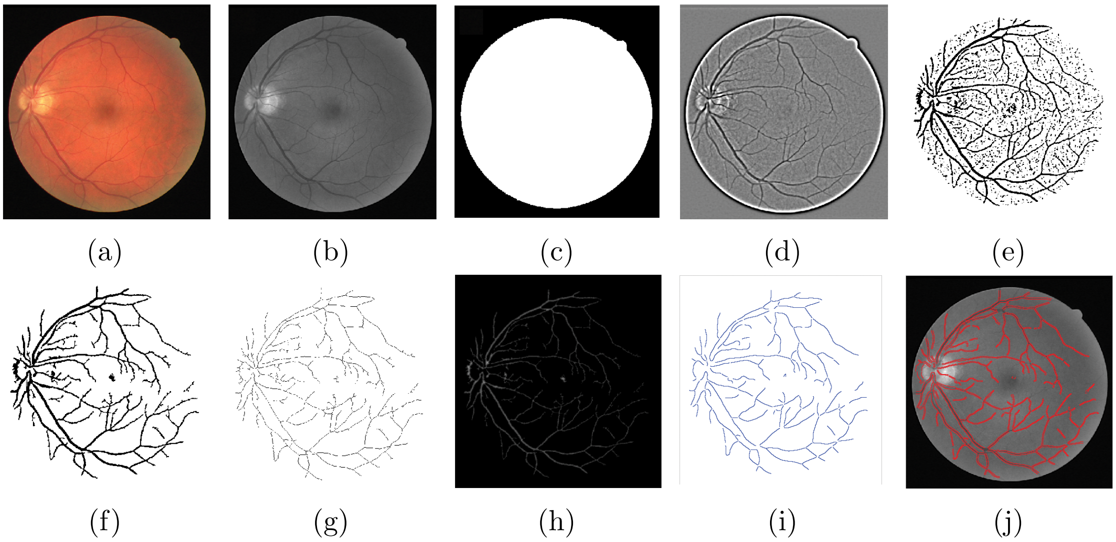

Figure 2.10: A wavelet transform-based curvilinear features enhancement approach workflow: (a) An RGB input image (from the DRIVE database) is loaded. (b) A green channel is selected for later processing. (c) A mask is produced by global thresholding. (d) The wavelet transform is applied to (b). (e) Wavelet coefficients are thresholded. (f) Small objects are removed and holes are filled in (e). (g) Morphological thinning is applied to (f). (h) Distance transform is applied to (f) to assist with estimating diameters and removing erroneously detected segments. (i) Branches are removed from (g) and spline fitting applied to determine centrelines. (j) Edges are detected perpendicular to the centrelines. (this Figure is adopted from [11]).

the random forest classifier. A major drawback of this method is the complexity of its parameter space. Since it is difficult to determine optimal parameters for each type of data. Also, it is not capable to work with the different type of objects to be enhanced.

2.2.6 Line Detector-based Enhancement Methods

Curvilinear feature enhancement has also been done using multiscale line detectors [84]. The approach is carried out by changing the length of a primary line detector with varying scales. The line response, identified by subtraction of average value and the maximum value of each pixel, is computed at 12 different line directions. The main idea behind this method is that line detectors with smaller lengths

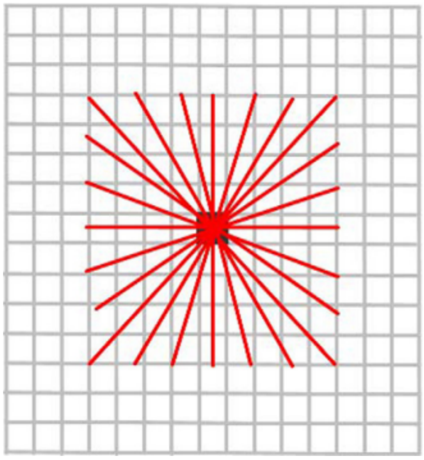

Figure 2.11: A generalized line detector. (this Figure is adopted from [84]).

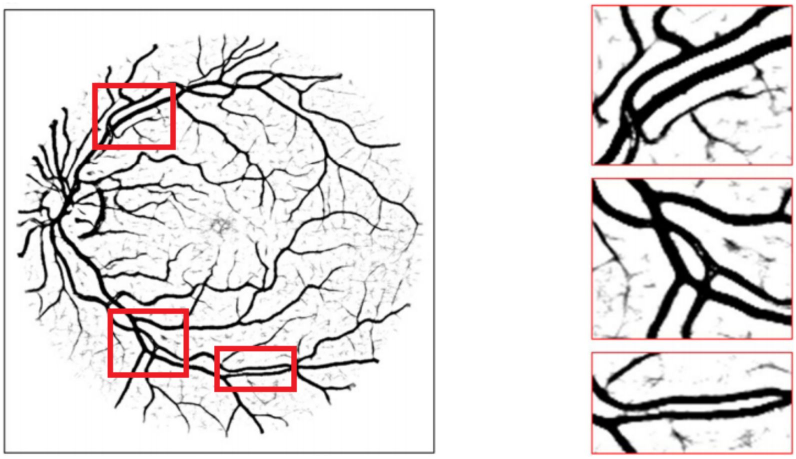

(a) (b)

Figure 2.12: (a) Line strength image obtained after the linear combination process on retinal image, and (b) is the result at the some image patches showing merging nearby curvilinear structures (this Figure is adopted from [84]).

will avoid the combination of the region of curvilinear structure pixels and therefore, provide correct responses (see Figure 2.11). A major drawback of this method is at junctions, where the method produces 'false curvilinear structures' by merging nearby curvilinear structures (see Figure 2.12). Further improvement of this method is demonstrated in [85] where a linear combination of all the line responses at varying scales is proposed to produce the final enhancement and segmentation.

Enhancement Approach	Time [seconds]		
	DRIVE	STARE	HRF
Size/per-image	[584 × 565]	[605 × 700]	[2336 × 3504]
Vesselness	7.853	5.1	90.094
Zana's top-hat	0.717	1.168	12.663
Neuriteness	1.043	1.423	72.296
PCT-vesselness	2.170	2.145	297.691
PCT-neuriteness	1.620	2.005	217.41
Line detector	1.784	1.28	16.323
SCIRD	8.513	5.009	136.407
RORPO	11.787	16.562	259.322

Table 2.2: An average computation time for the state-of-the-art curvilinear structure enhancement approaches across the DRIVE, STARE and HRF datasets.

2.2.7 Mathematical Morphology-based Enhancement Methods

Mathematical morphology has been used by many researchers to enhance and segment curvilinear structures [86–91]. Zana and Klein [86] proposed a novel method which combines morphological transforms and cross-curvature evaluation for curvilinear structure enhancement and segmentation. This method relies on the assumption that vessels are linear, connected and have smooth variations of curvature along the ridge of the curvilinear feature. First, a sum of mathematical morphology top-hats is calculated using linear structuring elements with the single size (15-pixels long for images used in [86]) at different orientations, and after enhancement step, a curvature measure is calculated using a Laplacian of Gaussian, and finally, both of them are combined to reduce noise and enhance curvilinear structures in an image. Further improvement of this method is demonstrated in [75, 92, 93]. In particular, in [92], an advanced morphological directional filter called path openings is linked with data fusion based on fuzzy set theory. This approach has four steps; First is preprocessing, where the image undergoes histogram equalisation, and then

Gaussian filtering to improve the effectiveness of the second step (see Figure 2 in [92]). The second step involves feature extraction by detection of local minima and edges in the image (see Figure 1; (b) and (c) in [92]). The third step preserves connected vessels and suppresses noise by path opening (see Figure 1; (d) and (e) in [92]), and the final step combines the features and possible paths into a fuzzy classification problem - identifying pixels as likely vessels or likely background (see Figure 3 in [92]).

And most recently, in [93], a multiscale morphological top-hats transform (see Chapter 3 (*p.* 31)) is combined with Gabor and a matched filter. A major issue with this method is that it is quite sensitive to noise, this problem inherits from the mathematical morphology and CLAHE.

A mathematical morphology-based path opening and closing operation to detect the curvilinear structures in retinal images was introduced by [33]. Recently, a new path operator called Ranking the Orientation Responses of Path Operators (RORPO) has been proposed to distinguish curvilinear objects from blob-like and planar structures in images [94, 95]. The main disadvantage of the RORPO approach is its high computation cost when applied to large volume image datasets (see Table 2.2).

2.2.8 Other Approaches

Recently, deep learning approaches have shown great potential for curvilinear structure enhancement and segmentation [96–101]. In particular, a new regression architecture based on the filter banks learned by sparse convolutional coding is proposed by [100]. The approach is based on a novel initialisation strategy, using carefully designed hand-crafted filters (SCIRD-TS) which are modelling appearance properties of curvilinear structures.

Epilogue

Image enhancement aims to improve the visual quality of an image to aid human qualitative analyses and automated quantitative analyses of features/objects in the image. In this Chapter, I presented the state-of-the-art curvilinear feature enhancement methods. All these methods have been used as comparator methods and have been tested on the synthetic and real-world biomedical image data in the following Chapters.

Chapter 3

An Introduction to Mathematical Morphology

Morphology is a term in biology that used to explain the structures in plants and animals, also in imaging, it resembles in many aspects [102]. It is a branch of image processing that allows detecting specific geometric structures in images. The first time, it was proposed by Georges Matheron, and Jean Serra proposed to use it to measure the distribution of particles in binary images [13]. Later on, it has been used for the grayscale images for a great variety of problems such as; noise suppression [103], edge detection [14], skeletonisation [104], granulometry [105], and the watershed transform-based segmentation [106].

In this Chapter, I will introduce the mathematical morphology concept which behind the image enhancement methods that I have studied in this thesis. First, I will identify the two fundamental operations which are the dilation and erosion in a binary image to increase the perceptibility, followed by opening and closing, which are the combination of dilation and erosion. I will discuss the extension of these four operators to grayscale before going on to explain the more complex method created by mathematical morphology: the top-hat transform.

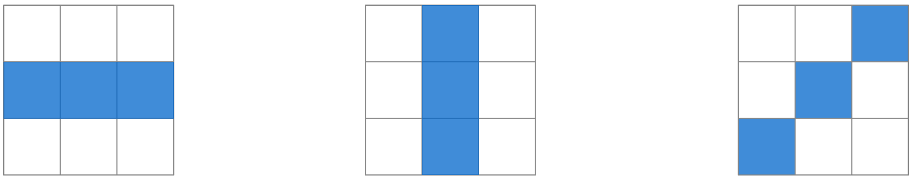

(a) Horizontal line 0°   (b) Vertical line 90°   (c) Diagonal line 45°

(d) Square   (e) Cross

Figure 3.1: Different shape of structuring elements (a-e).

3.1 Mathematical Morphology in Binary Images

Let us assume that the binary image $I(\vec{p})$ is a set of points embedded into $\mathbb{Z}^2$ and the structuring element (SE) that equivalent to the kernel used for convolution. The structuring element should be smaller than the object of interest, binary, have a shape that distinguishes features of interest in the image (see Figure 3.1). To give an example, if we would like to enhance and then detect curvilinear structures in an image, rotated line structuring element should be used. To choice of type and size may impact on the transform either operations (Figure 3.2). Since the target region is normally different from the background that is surrounding the region of features, it is essential to choose the right structuring element.

Two basic mathematical morphology operations, dilation and erosion, are proposed by [102]. Dilation expands or dilates features that equal to SE used. Mathematically, binary dilation, $\oplus$, on an image I with SE b is defined as;

$$(I \oplus b) = \left\{ \vec{p} \in \mathbb{Z}^2 | (b^s)_{\vec{p}} \cap I \neq \varnothing \right\}, \tag{3.1}$$

where b^s is the symmetric of b, $b^s = \{x| - x \in b\}$, and $(b^s)_{\vec{p}}$ is a translation of b^s by vector $\vec{p}$ which is the all points in space. To understand the binary dilation visually,

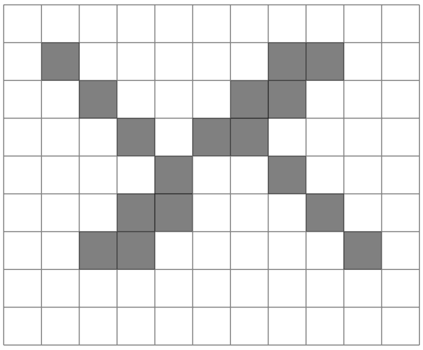

(a) Input image dilated by square and cross structuring element

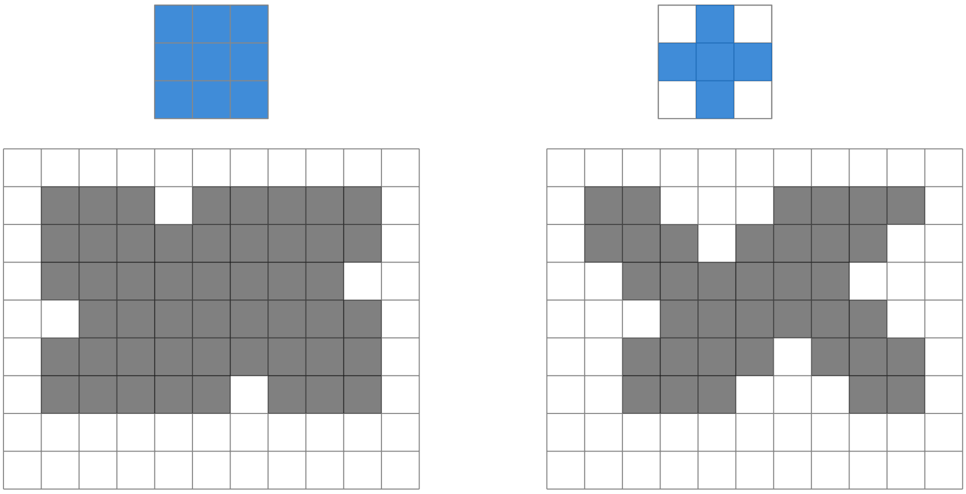

(b) Dilated by square

(c) Dilated by cross

Figure 3.2: Comparison of dilation results obtained by use of two different types of structuring elements. (a) An input binary image. Dilation of the image with (b) square structuring element and with (c) cross structuring element.

see Figure 3.3, where the feature in the binary image is dilated based on the square shape of the SE.

On the contrary to the dilation, mathematical morphology erosion operation erodes the image. Mathematically, binary erosion, $\ominus$, of an image I with SE b is defined as;

$$(I \ominus b) = \left\{\vec{p} \in \mathbb{Z}^2 | b_{\vec{p}} \subseteq I\right\}, \tag{3.2}$$

where $b_{\vec{p}}$ is a translation of b by vector $\vec{p}$. Figure 3.4 illustrates the erosion of a

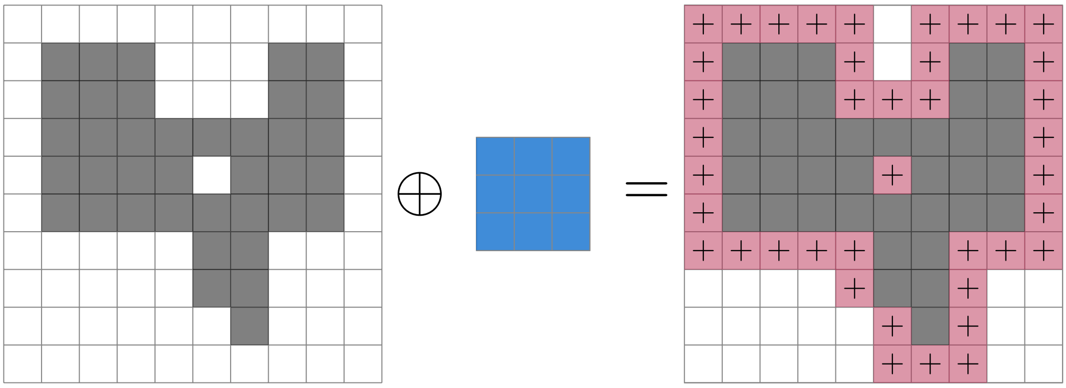

Figure 3.3: Dilation of a binary image with a square structuring element. '+' sign illustrates the pixels are added.

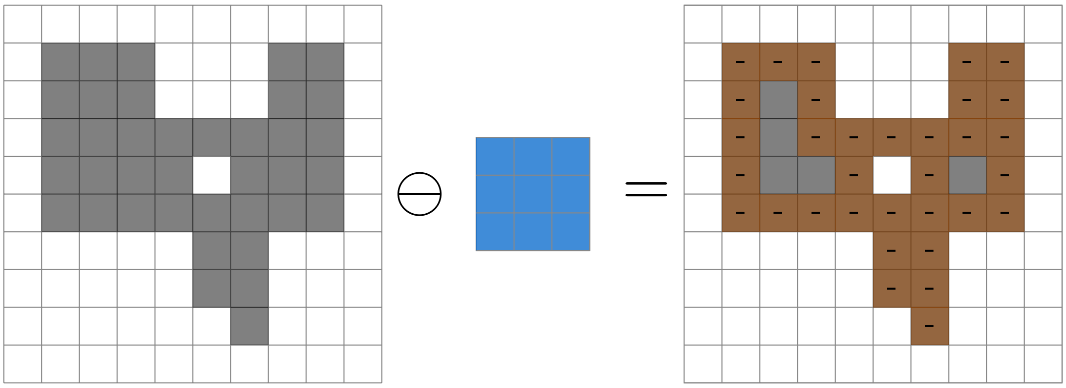

Figure 3.4: Erosion of a binary image with a square structuring element. '-' sign illustrates the pixels are removed.

binary image. Note how the boundaries of the original object are eroded based on the square shape of the SE.

More complex mathematical morphology operations, called opening and closing, were proposed by [102]. An opening is an erosion followed by a dilation of an image I with SE b defined as;

$$(I \circ b) = ((I \ominus b) \oplus b). \tag{3.3}$$

Vice versa, closing is a dilation followed by erosion as;

$$(I \bullet b) = ((I \oplus b) \ominus b). \tag{3.4}$$

Figure 3.7 shows an example of opening and closing of the same input image with a

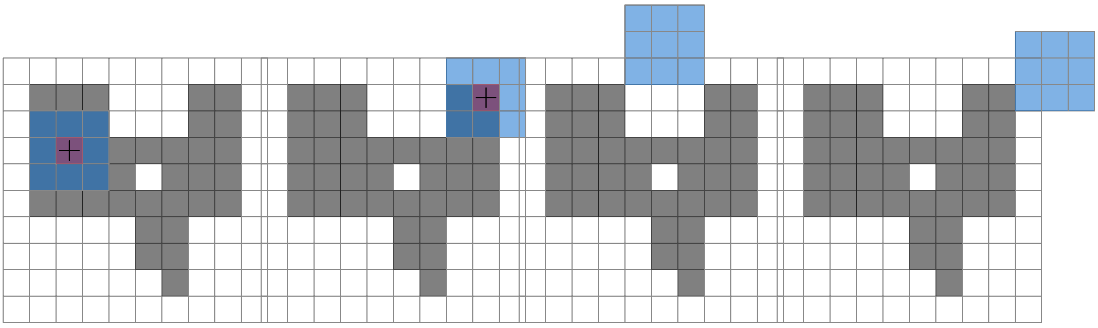
(a) (b) (c) (d)

Figure 3.5: Dilation on a pixel-by-pixel basis where structuring elements cover non-empty and empty pixels. Pixels are added (illustrated with '+' sign) when there is a non-empty pixel under the SE when centered on that pixel even when the majority of pixels are empty (a-b). Pixels are left empty when there are no non-empty pixels under the SE which, with this SE is mostly the border pixels (c-d).

square structuring element. The opening and closing are non-linear morphological operations, where opening opens the objects/regions in an image (as in Figure 3.7a and Figure 3.8) and closing closes objects/regions in an image (as in Figure 3.7b).

3.2 Mathematical Morphology in Grayscale Images

3.2.1 Grayscale Dilation and Erosion

To extend from binary to grayscale mathematical morphology, grayscale structuring element b contains a finite number of pixels to account for the embedding of the image in $\mathbb{R}$ as opposed to $\mathbb{Z}$ as for the binary case. Grayscale dilation is defined as;

$$(I \oplus b)(\vec{p}) = \sup_{\vec{q} \in \mathbb{R}^2} \left(I(\vec{q}) + b(\vec{p} - \vec{q}) \right), \tag{3.5}$$

and, grayscale erosion as;

$$(I \ominus b)(\vec{p}) = \inf_{\vec{q} \in \mathbb{R}^2} \left(I(\vec{q}) - b(\vec{q} - \vec{p}) \right), \tag{3.6}$$

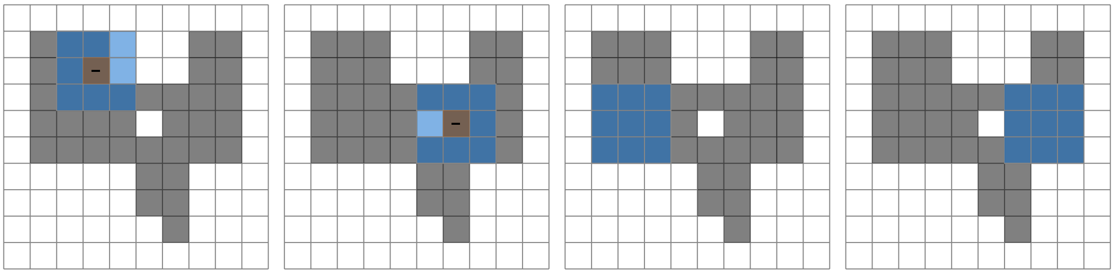

(a) (b) (c) (d)

Figure 3.6: Erosion on a pixel-by-pixel basis where structuring elements cover empty and non-empty pixels. Pixels are removed (illustrated with '−' sign) when there is an empty pixel under the SE when centered on that pixel even when the majority of pixels are non-empty (a-b). Pixels are kept when there are no empty pixels under the SE which, with this SE is rare(c-d).

where $\sup_{\vec{q}}$ is the supremum over all $\vec{q}$, for image processing this is the equivalent to the weighted maximum over the SE centered at $\vec{q}$, and $\inf_{\vec{q}}$ is the infimum over all $\vec{q}$, equivalent to the weighted minimum over the SE centered at $\vec{q}$.

Figure 3.8 demonstrates grayscale dilation and erosion of a simple grayscale image. Dilation expands the image while erosion decreases the feature of interest. Grayscale opening and closing are demonstrated in Figure 3.8. Opening smooths the image and removes narrow ridges. By the same manner, closing smooths the image by filling valleys.

3.2.2 Grayscale Opening, Closing, and Top-Hat

Grayscale dilation and erosion are used to defined grayscale opening, closing and top-hat operations as follows;

$$\text{opening}: \quad (I \circ b)(\vec{p}) = ((I \ominus b) \oplus b)(\vec{p}), \tag{3.7}$$

$$\text{closing}: \quad (I \bullet b)(\vec{p}) = ((I \oplus b) \ominus b)(\vec{p}), \tag{3.8}$$

$$\text{top-hat}: \quad TH(I,b) = I(\vec{p}) - (I \circ b)(\vec{p}), \tag{3.9}$$

$$\text{bottom-hat}: \quad BH(I,b) = I(\vec{p}) - (I \bullet b)(\vec{p}). \tag{3.10}$$

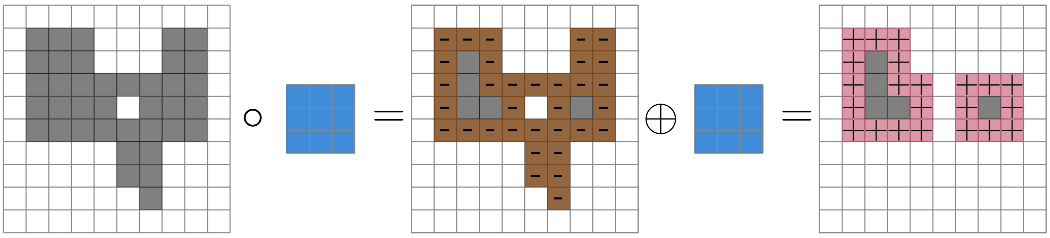
(a) Opening

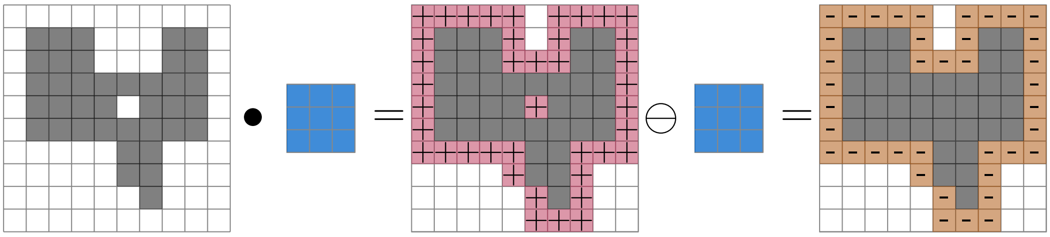
(b) Closing

Figure 3.7: Opening (a) and closing (b) of a binary image with a square SE. Note that, '+' sign illustrates the pixels are added and '-' sign illustrates the pixels are removed.

In general, grayscale opening (∘) preserves dark features and suppresses bright features, where closing (•) preserves bright features and suppresses dark features in an image. Grayscale top-hat enhances light features and bottom-hat enhances dark features in an image. Examples of how these operations work can be seen in Figure 3.8 and Figure 3.9.

3.3 Other Binary and Grayscale Operations

In this Chapter, my aim is to introduce mathematical morphology and the operations used throughout this thesis. Morphological operations are not limited to those operations I mentioned earlier: since many image analysis and processing, concepts rely on extracting features of objects, describing shapes, and recognizing patterns, many image processing methods can be described in the form of morphological operations.

In this Section, I will present several fundamental morphological operations and

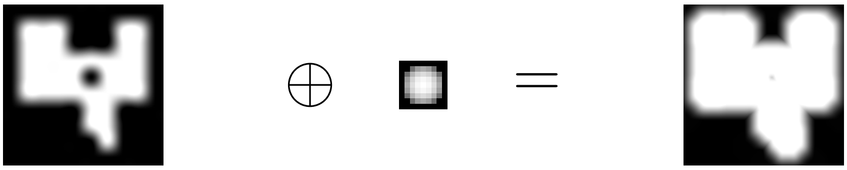

(a) Dilation.

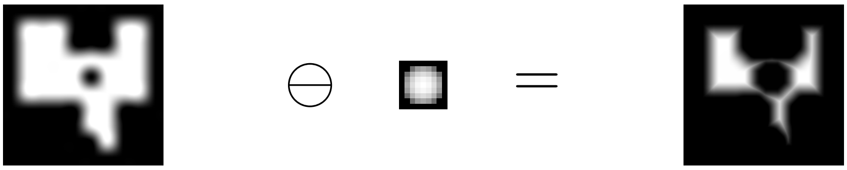

(b) Erosion.

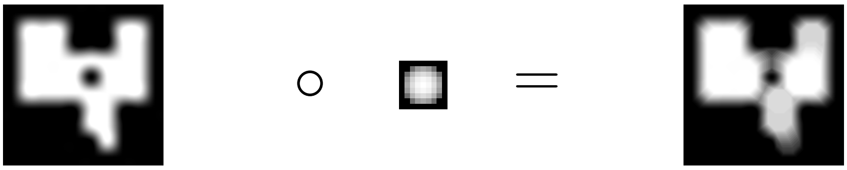

(c) Opening.

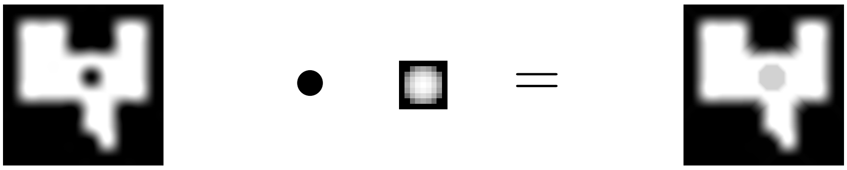

(d) Closing.

Figure 3.8: Grayscale mathematical morphology operations applied to a simple grayscale image. (a) Dilation, (b) erosion, (c) opening, and (d) closing.

where/how to use them, including boundary extraction, region filling, connected components extraction, convex hull, thinning, thickening, skeletonisation, pruning, and morphological edge operators. For an extensive summary of morphological operations, see [108], Table 9.1.

The hit-or-miss transform (HMT) is an operation for pattern recognition and analysing of binary images by using morphological erosion with a pair of disjoint structuring elements. HMT is a straightforward and powerful morphological tool and has been in lots of image processing research. Bloomberg and Maragos [109] proposed a generalization of HMT to process grayscale images that relied on grayscale erosion.

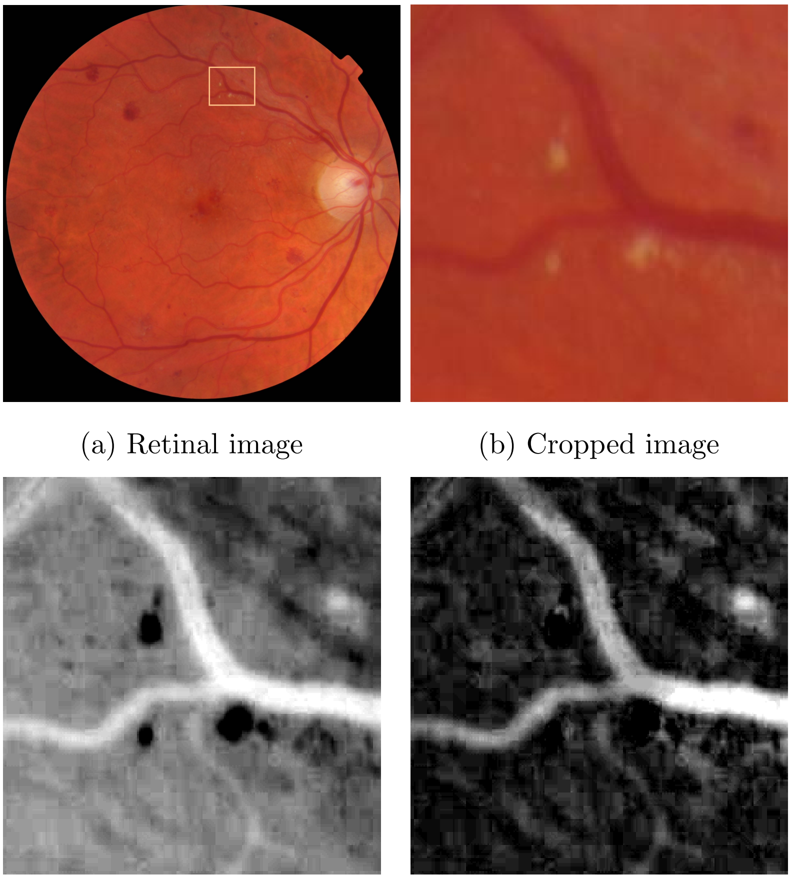

(a) Retinal image (b) Cropped image

(c) Green channel (d) Top-hat result

Figure 3.9: Top-hat transform. (a) A retinal image from the DR HAGIS [107] dataset. A top-hat transform with the disk shape SE radius 15 pixel result (d) when applied to a grayscale version (c) of the cropped image (b).

Grey-level HMTs was applied angiogram processing by [110, 111]. A class of rank-based template matching criteria by using grayscale HMT was proposed by [112]. A modified version of morphological HMT for object detection was presented by [113]. Whilst Raducanu and Grana [114] propose a modified HMT based on level sets to obtain a translation invariant recognition tool, with some robustness regarding small deformations and variations in illumination.

Boundary extraction and edge detection can also be done using mathematical morphology. Wood *et al.* [115] proposed a vessel segmentation algorithm using a morphological filtering method to locate vessel segments. Mendonca and Campilho

[116] offered a shape-based approach for the segmentation of the vascular network in retinal images that comprises of ridge detection, morphological curvilinear-object enhancement and, curvilinear-object reconstruction. Figueiredo and Leitao [117] represented anon-smoothing method for estimating vessel contours in angiograms. Under the assumptions of curvilinear features, edge detection was achieved by adopting a morphological grayscale edge operator.

Eiho and Qian [118] proposed a method based on only morphological operators (top-hat transform, erosion, etc.) for the detection of the coronary artery tree in angiograms. First, the top-hat transform was used to enhance curvilinear structures, then erosion operators were applied to remove the unwanted areas, leaving only the coronary artery area. After that, the extracted curvilinear structures were skeletonised by thinning. Eventually, the edges were extracted by applying the watershed transformation on the binary image obtained from a dilation operation on the binary skeleton already extracted.

Donizelli [119] combined mathematical morphology and region growing algorithms to segment large vessels in angiography images. First, the top-hat transform was applied to extract large vessels, then a binary region growing algorithm was used to eliminate some remaining fine vessels and background noise artefacts. Afterwards, regions smaller than a given threshold were removed leaving only the large vessels. Others implemented two similar mathematical morphology-based approaches; region splitting approach [120], and morphological-thresholding [121]. Fetita *et al.* [122] proposed a method based on region-based morphology to extract airways from CT. Another region-based method was proposed by Fraz *et al.* [123] where centrelines were detected with a first-order Gaussian filter, and then vessels were reconstructed by means of the top-hat transform. Roychowdhury *et al.* [124] presented an iterative method that relies on region growing. The method obtains a first estimation by performing a top hat transform of the inverted green channel and getting a rough estimation of regions by thresholding it.

Chapter 4

Contrast-Independent Curvilinear Structure Enhancement in 3D Biomedical Images

Prologue

A wide range of biomedical applications require detection, quantification and modelling of curvilinear structures in 3D images. In this Chapter, I will propose a 3D contrast-independent approach to enhance curvilinear structures based on the 3D Phase Congruency Tensor concept proposed by [16]. The obtained results show that the proposed method is insensitive to intensity variations along the 3D curve, and provides successful enhancement within noisy regions. The quality of the 3D Phase Congruency Tensor-based method is evaluated by comparing it with state-of-the-art intensity-based approaches on both synthetic and real biomedical images.

Declaration: This Chapter is based on the following publication: Sazak, Ç. & Obara, B. *Contrast-independent curvilinear structure enhancement in 3D biomedical images* in *IEEE International Symposium on Biomedical Imaging* (2017), 1165–1168. This Chapter is presented as published, although referencing and notation has been altered and cross-referencing added for consistency throughout this thesis. Some stylistic changes have been made for consistency. The majority of the text is verbatim; however, additions to the body of text are included where they are appropriate.

4.1 Introduction

The explosive growth in size and complexity of biomedical imaging data and the need for extracting quantitative information increasingly requires sophisticated bioimage analysis methods. As a common requirement of strong and durable image enhancement, segmentation and analysing of curve-like features are essential in bioimaging. Accordingly, a significant number of image processing solutions has been propounded to enhance and extract 3D curve-like structures such as blood vessels [4, 49], airways in lung images [125], dendritic spines [126], neurons[76], microtubules [127], and others as reviewed in [128]. Despite such a wide range of approaches, the robust enhancement of 3D curvilinear structures remains challenging due to the intensity variations along the 3D curve. To overcome this challenge, I propose a 3D contrast-independent approach to enhance curvilinear structures based on the Phase Congruency Tensor (PCT) concept [10]. Also, it will be shown that by replacing the Hessian tensor with PCT, I may actively reduce the dependence on local image contrast which has hampered other tensor-based methods. In particular, I show how the PCT concept may be used to improve standard 3D curvilinear feature measurement techniques, like vesselness and neuriteness. The Chapter is organized as follows; In Section 4.2, I formulate the 3D PCT concept. Experimental results for 3D synthetic and real biological images are presented in Section 4.4. Section 4.5 is dedicated to conclusions.

4.1.1 3D Intensity-based Curvilinear Structure Enhancement

Using Tensors for Local Feature Representation

The tensor representation of the local image structure almost provides the most information about how much the image structures change through and across the dominant directions and, is generated by combining the outputs from polar separable quadrature filters [16]. Assume that an image $I(\vec{p})$, that $\vec{p}$ is pixel representation of the 3D spatial location. A suitable notation of the local structure of the surface in the region of $\vec{p}$ is given by the tensor defined as follows;

$$T = \sum_{\Theta} \|q_\Theta\| (\vec{n}_\Theta \vec{n}_\Theta^T), \tag{4.1}$$

where q_Θ is the output from an oriented quadrature filter applied to an image $I(\vec{p})$, as defined in Equation (2.27) (*p.* 21) and Equation (2.32) (*p.* 22), and $\vec{n}_\Theta$ is the column vector in the direction Θ. In the 3D case, an orientation $\Theta = (\theta, \phi)$ can be specified by elevation θ and azimuth ϕ angles on a sphere of unit radius [129], and $\vec{n}_\Theta$ is the column vector;

$$\vec{n}_\Theta = \vec{n}_{\theta,\phi} = [sin(\theta)cos(\phi), sin(\theta)sin(\phi), cos(\theta)]^T. \tag{4.2}$$

4.2 Method

Our 3D extension of a 2D Phase Congruency Tensor (PCT) concept introduced by [10] is proposed here. The 3D PCT concept is then used to define 3D curvilinear feature enhancement methods which are PCT-vesselness and PCT-neuriteness.

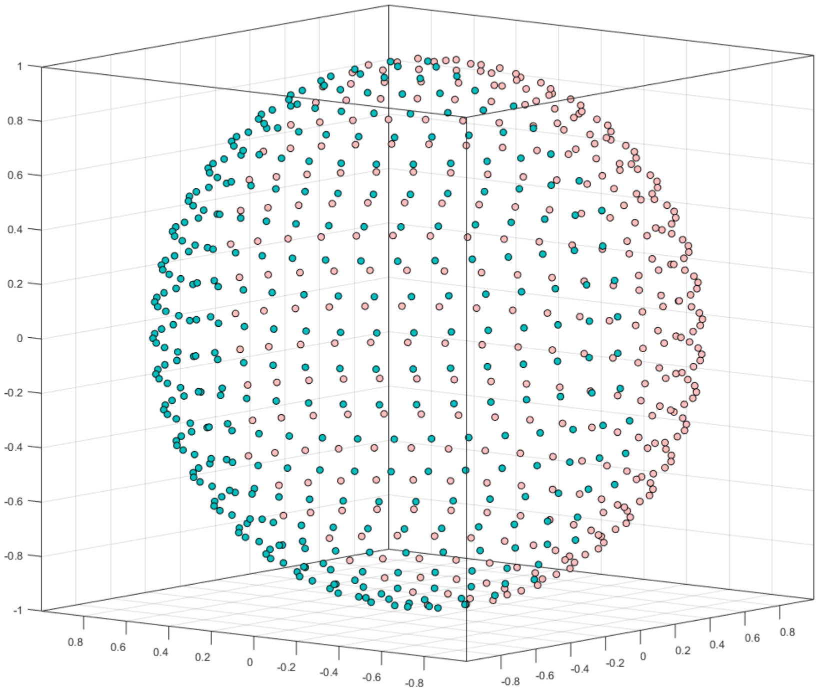

Figure 4.1: Uniform distribution of $N = 250$ points on the unit sphere calculated with an approach proposed by [130].

4.2.1 Orientation

In order to calculate the 3D PCT, a set of N oriented quadrature filters (see Equation (2.27) (*p.* 21) and Equation (2.32) (*p.* 22)) are defined by a set of N 3D orientations;

$$\{\Theta\} = \{(\theta_k, \phi_k)\}_{k=1}^{N}. \tag{4.3}$$

Such a set of 3D orientation is calculated using a concept of uniformly distributed points on the unit sphere proposed by [130, 131] (see Figure 4.1). Each point (θ_k, ϕ_k) on the sphere is generated by a 'spiral scheme' as follows;

$$\theta_k = \arccos\left(h_k = -1 + \frac{2\,(k-1)}{(N-1)}\right), \quad 1 \le k \le N, \tag{4.4}$$

$$\phi_k = \left(\phi_{k-1} + \frac{3.6}{\sqrt{N}} \frac{1}{\sqrt{1-h_k^2}} \right) (\mathrm{mod}\ 2\pi) , \tag{4.5}$$
$$2 \leq k \leq N-1, \phi_1 = \phi_N = 0.$$

where $0 \leq \theta \leq \pi$, $0 \leq \phi \leq 2\pi$.

4.2.2 3D Phase-based Detection

In terms of the local image phase approach that is contrast-independent curvilinear enhancement has been investigated by [132]. The calculation of local phases needs the use of quadrature pairs of filters to the image. Consequently, for a given image $I(\vec{p})$ and a quadrature pair of even $F^e_{s,\Theta}$ and odd $F^o_{s,\Theta}$ filters at scale s and orientation Θ, the response vector is given by its even and odd components $e_{s,\Theta}(\vec{p})$ and $o_{s,\Theta}(\vec{p})$;

$$\left[e_{s,\Theta} \left(\vec{p} \right), o_{s,\Theta} \left(\vec{p} \right) \right] = \left[I \left(\vec{p} \right) * F^e_{s,\Theta}, I \left(\vec{p} \right) * F^o_{s,\Theta} \right] . \tag{4.6}$$

The amplitude of the s^{th} component is defined as;

$$A_{s,\Theta} \left(\vec{p} \right) = \sqrt{ e_{s,\Theta} \left(\vec{p} \right)^2 + o_{s,\Theta} \left(\vec{p} \right)^2 }, \tag{4.7}$$

and the local phase given by;

$$\varphi_{s,\Theta} \left(\vec{p} \right) = atan \left(\frac{o_{s,\Theta} \left(\vec{p} \right)}{e_{s,\Theta} \left(\vec{p} \right)} \right) , \tag{4.8}$$

To implement phase enhancement, several quadrature filters have been proposed, especially the log-Gabor filter [133].

For our method, a 3D log-Gabor filter has been used. Log-Gabor has two components, and they are obtained by multiplying the angular and radial components of the Gaussian transfer function on the logarithmic frequency domain [133];

$$\hat{\mathcal{L}}(\omega, \Theta) = \mathrm{e}^{\left(-\frac{\ln\left(\frac{\omega}{\omega_0}\right)^2}{2\ln\left(\frac{\sigma_\omega}{\omega_0}\right)^2}\right)} \cdot \mathrm{e}^{\left(-\frac{\Theta^2}{2\sigma_\Theta^2}\right)}, \tag{4.9}$$

where ω_0 is the central radial frequency of the filter and σ_ω is the standard deviation controlling the filter bandwidth. Θ is the orientation of the filter and σ_Θ determines the angular spread.

4.2.3 Phase Congruency

Phase congruency has been used to find a wide range of low-contrast features including step edges, line and roof edges [134]. The phase congruency design assumes that features are recognized at points where the Fourier components are maximally in phase. In 3D, the phase congruency at several orientations is defined as [134];

$$PC_{s,\Theta}(\vec{p}) = \sum_{\Theta} \left(PC_\Theta(\vec{p})\right), \tag{4.10}$$

and the phase congruency at each orientation Θ is defined as;

$$PC_\Theta(\vec{p}) = \frac{\sum_s w_\Theta(\vec{p}) \max(A_{s,\Theta}(\vec{p})\Delta\Phi_{s,\Theta}(\vec{p}) - t, 0)}{\sum_s A_{s,\Theta}(\vec{p}) + \varepsilon}. \tag{4.11}$$

$A_{s,\Theta}(\vec{p})$ is the amplitude of the image component at the location $\vec{p}$ through the use of a 3D log-Gabor filter with the scale s and orientation Θ. The t is a noise threshold and ε a factor that ensures against the division of zero [132]. The weight of frequency spread $w_\Theta(\vec{p})$ is defined as;

$$w_\Theta(\vec{p}) = \frac{1}{1 + \mathrm{e}^{(\mu(b - l_\Theta(\vec{p})))}}, \tag{4.12}$$

which penalizes frequency distributions that are expressly narrow. The parameters μ and b in this function are constants describing a gain factor and a cut-off value, respectively. A measure of filter response spread is defined as;

$$l_{\Theta}(\vec{p}) = \frac{1}{\aleph}\left(\frac{\sum_s A_{s,\Theta}(\vec{p})}{A_{\max}(\vec{p}) + \epsilon}\right), \tag{4.13}$$

where $\aleph$ is a total number of scales. Finally, a phase deviation $\Delta\Phi_{s,\Theta}(\vec{p})$ in Equation 4.11 is defined as;

$$\begin{aligned}\Delta\Phi_{s,\Theta}(\vec{p}) = {} & e_{s,\Theta}(\vec{p})\bar{\varphi}^{e}_{s,\Theta}(\vec{p}) + o_{s,\Theta}(\vec{p})\bar{\varphi}^{o}_{s,\Theta}(\vec{p}) \\ & - |e_{s,\Theta}(\vec{p})\bar{\varphi}^{o}_{s,\Theta}(\vec{p}) - o_{s,\Theta}(\vec{p})\bar{\varphi}^{e}_{s,\Theta}(\vec{p})|,\end{aligned} \tag{4.14}$$

where $\bar{\varphi}^{\{e,o\}}_{s,\Theta}(\vec{p}) = \sum_s \{e,o\}_{s,\Theta}(\vec{p})/E_{\Theta}(\vec{p})$, and

$$E_{\Theta}(\vec{p}) = \sqrt{\left(\sum_s e_{s,\Theta}(\vec{p})\right)^2 + \left(\sum_s o_{s,\Theta}(\vec{p})\right)^2}, \tag{4.15}$$

where $E_{\Theta}(\vec{p})$ is the local energy and $\varphi_{s,\Theta}(\vec{p})$ is the cosine of the deviation of the phase while $\bar{\varphi}_{s,\Theta}(\vec{p})$ is the overall mean phase angle. Phase congruency is explained step by step in the Chapter 2: Section 2.2.3 (*p.* 19) and Figure 2.7.

4.2.4 3D PCT-Vesselness and -Neuriteness

3D piecewise curvilinear segments can be enhanced by analysing the relations between eigenvalues and eigenvectors of the 3D Hessian. In a similar way, using Equations 4.16 and 4.18, our 3D PCT-based vesselness and 3D PCT-based neuriteness are defined where the eigenvalues of 3D Hessian are substituted with those of the 3D Phase Congruency Tensor T.

3D PCT-Vesselness

PCT-vesselness, as defined in [4], is computed as the ratio of the eigenvalues of $T_\sigma(\vec{p})$ as;

$$V_\sigma = \begin{cases} 0 & \lambda_{\sigma,2}, \lambda_{\sigma,3} < 0 \\ \left(\mathrm{e}^{\left(-\dfrac{R_\beta^2}{2\beta^2}\right)}\right)\left(1-\mathrm{e}^{\left(-\dfrac{R_\alpha^2}{2\alpha^2}\right)}\right)\left(1-\mathrm{e}^{\left(-\dfrac{S^2}{2c^2}\right)}\right) & \text{otherwise} \end{cases}, \tag{4.16}$$

where

$$S = \sqrt{\lambda_{\sigma,1}^2 + \lambda_{\sigma,2}^2 + \lambda_{\sigma,3}^2}, \quad R_\beta = \frac{|\lambda_{\sigma,1}|}{\sqrt{|\lambda_{\sigma,2}\lambda_{\sigma,3}|}}, \quad R_\alpha = \frac{|\lambda_{\sigma,2}|}{|\lambda_{\sigma,3}|},$$

where α, β and c are positive real user-defined parameters. The R_β ratio calculates blob-like features [4] and the R_α ratio helps to discriminate between plate-like and line-like structures [59]. S is equal to half of the maximum Frobenius norm and evaluates whether the eigenvalues are large compared to noise. Finally, multiscale vesselness, for a given set of scales $\sum = \{\sigma_i\}$ and $i = 1, 2, 3...$, can be calculated as [10];

$$V_{\sum} = \max_{\sigma \in \sum} (V_\sigma) \,. \tag{4.17}$$

3D PCT-Neuriteness

3D PCT-neuriteness, an equivalent of the Hessian matrix-based neuriteness proposed by [8] for 2D and extended in [76] for 3D, is calculated based on eigenvalues of $T_\sigma(\vec{p})$ as follows;

$$N_\sigma = \begin{cases} \dfrac{\lambda_{\sigma,max}}{\lambda_{\sigma,min}} & \lambda_{\sigma,max} < 0 \\ 0 & \lambda_{\sigma,max} \geq 0 \end{cases}, \tag{4.18}$$

where

$$\begin{aligned}
&\lambda_{\sigma,max} = \max(|\lambda'_{\sigma,1}|, |\lambda'_{\sigma,2}|, |\lambda'_{\sigma,3}|), \\
&\lambda_{\sigma,min} = \min(\lambda_{\sigma,max}), \\
&\lambda'_{\sigma,1} = \lambda_{\sigma,1} + \gamma\lambda_{\sigma,2} + \gamma\lambda_{\sigma,3}, \\
&\lambda'_{\sigma,2} = \gamma\lambda_{\sigma,1} + \lambda_{\sigma,2} + \gamma\lambda_{\sigma,3}, \\
&\lambda'_{\sigma,3} = \gamma\lambda_{\sigma,1} + \gamma\lambda_{\sigma,2} + \lambda_{\sigma,3}.
\end{aligned}$$

where $\lambda_{\sigma,min}$ denotes the smallest value of $\lambda_{\sigma,max}$ over all the pixels while $\lambda_{\sigma,max}$ largest one of eigenvalues $\lambda_{\sigma,i}$. Parameter γ is chosen by 1/3 as in [76].

4.3 Implementation

All codes were implemented and written in MATLAB 2015a on Windows 8.1 pro 64-bit PC running an Intel Core i7-4790 CPU (3.60 GHz) with 16 GB RAM. The source code is available in a GitHub repository https://github.com/CigdemSazak/phase-congruency-tensor-3d.

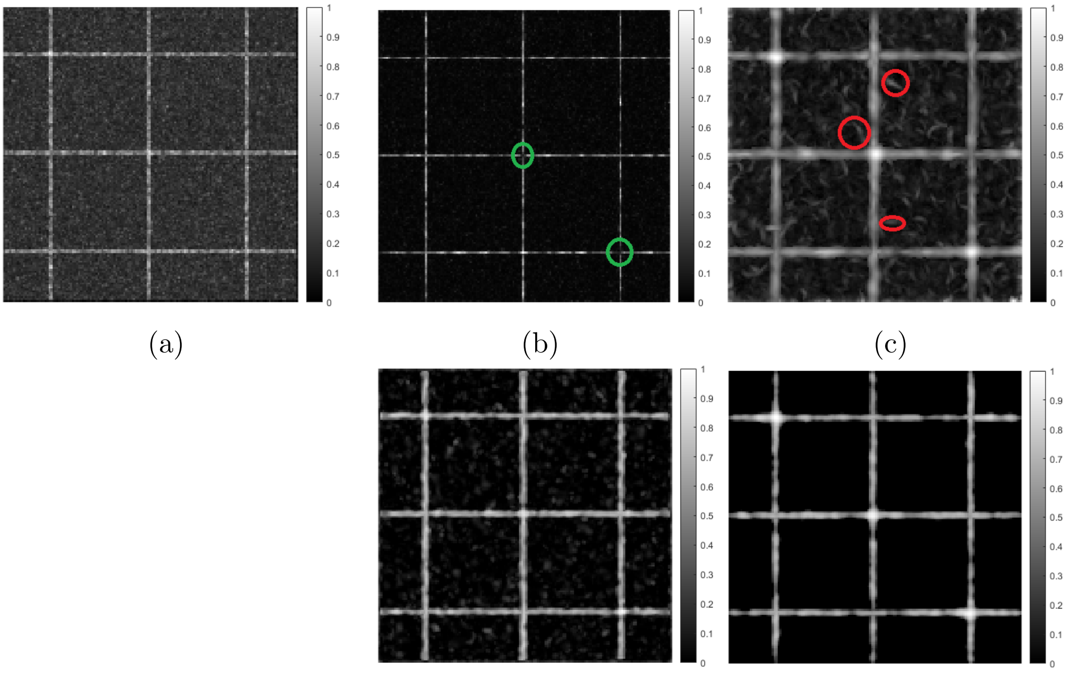

(a) (b) (c)

(d) (e)

Figure 4.2: Comparison between Hessian- and PCT-based approaches applied to a synthetic image (a), vesselness (b), neuriteness (c), PCT-vesselness (d), and PCT-neuriteness (e). 2D max projections of 3D images are shown. Green circles in the (b) illustrate cross sections in the enhanced image by traditional vesselness filter. As you notice that, it can not able to detect vessel junctions. Red circles demonstrate the false vessels. However, proposed method are free from the all the problems.

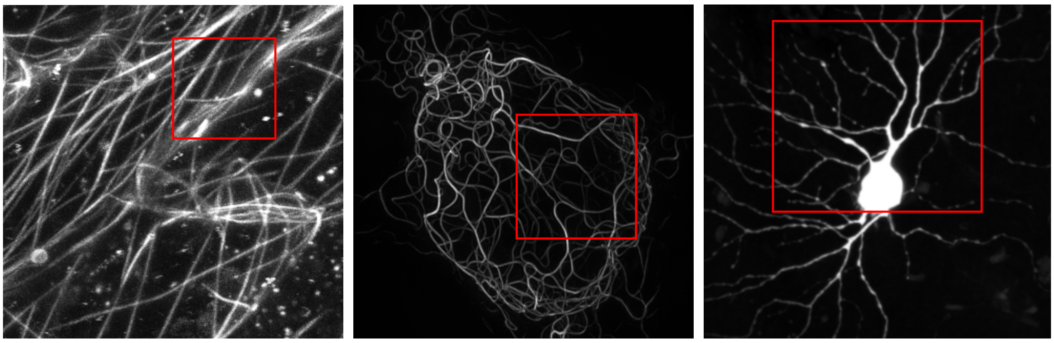

(a) (b) (c)

Figure 4.3: 2D max projections of 3D images of microtubules network in plant cell (a) and keratin network in skin cell (b) (provided by Dr. Tim Hawkins, Durham University, UK), and neuronal network (c) (provided by Dr. Chris Banna, UC Santa Barbara, USA). Regions of interest are highlighted in red.

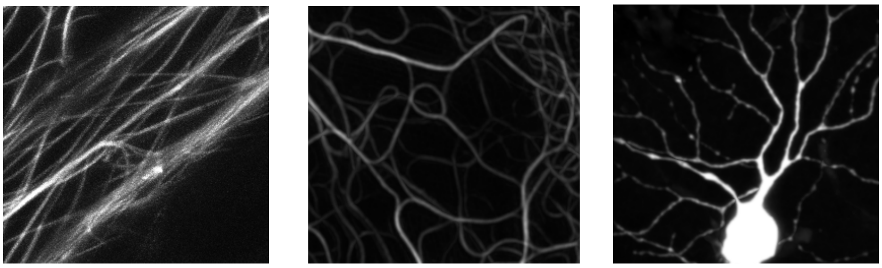

(a) Original images

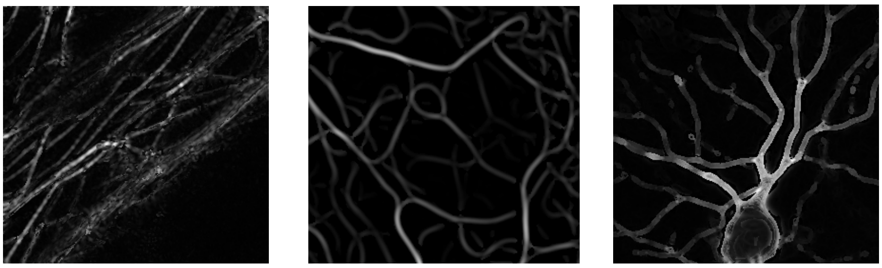

(b) Neuriteness

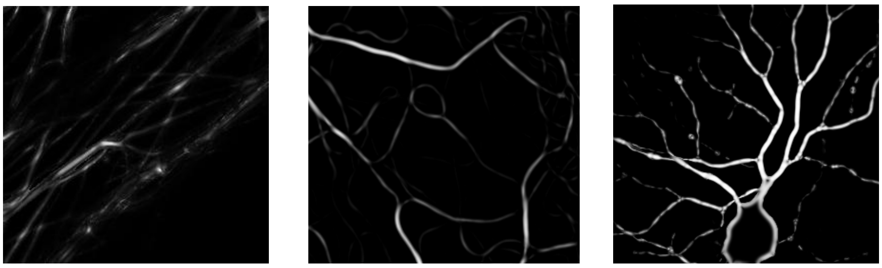

(c) Vesselness

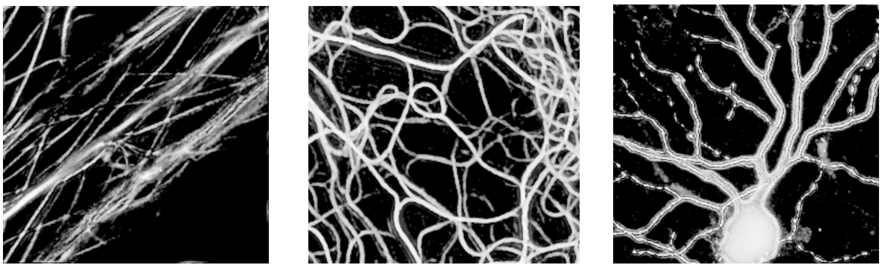

(d) PCT-neuriteness

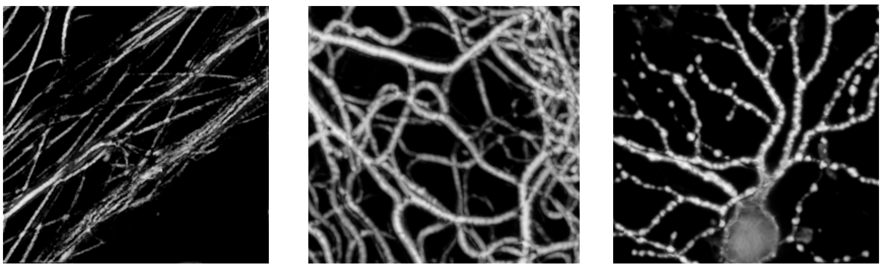

(e) PCT-vesselness

Figure 4.4: Comparison between Hessian- and PCT-based approaches applied to ROIs (a) from the Figure 4.3. Neuriteness (b), vesselness (c), PCT-neuriteness (d), and PCT-vesselness (e). Notice that, traditional vesselness and neuriteness can enhance the curvilinear structures, however PCT-based vesselness and neuriteness can not only enhance the obvious structures, but they can also enhance the fine structures.

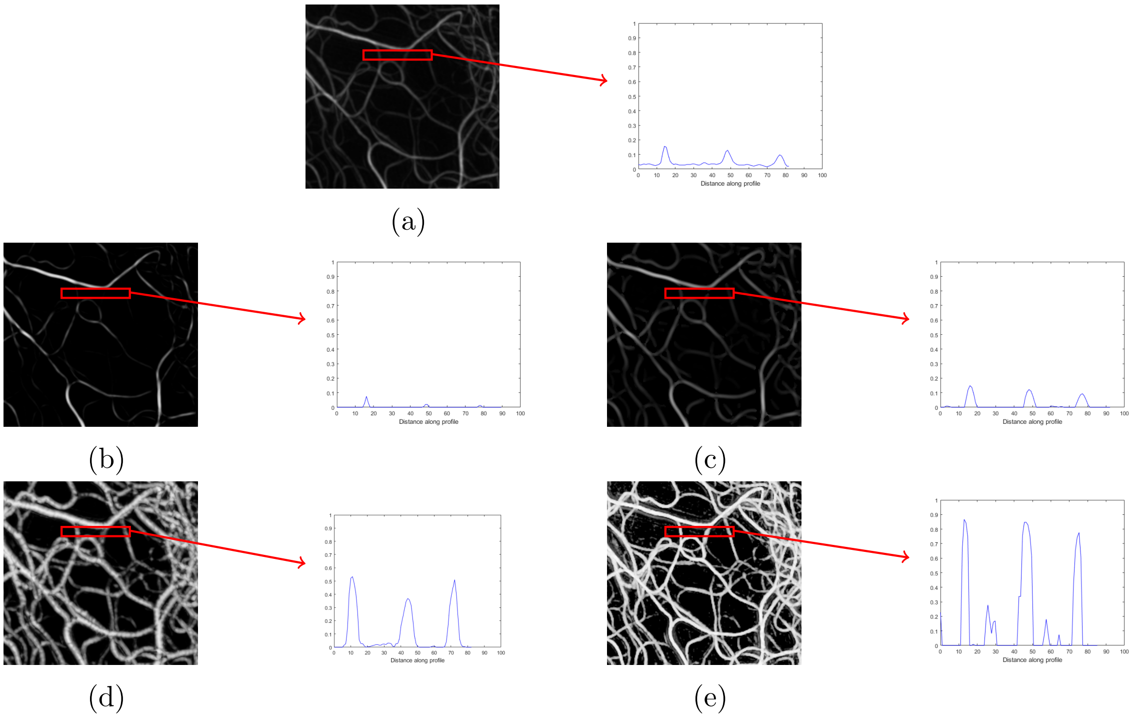

Figure 4.5: Comparison between Hessian- and PCT-based approaches applied to ROIs from Figure 4.3. Enhanced images are compared with the help of profile analysing. Notice that traditional vesselness and neuriteness can not enhance the fine curvilinear structures, while PCT-based vesselness and neuriteness can enhance both large and fine structures. (a) Raw image, (b) vesselness, (c) neuriteness, (d) PCT-vesselness, (e) PCT-neuriteness.

4.4 Results

PCT-based methods were compared with their corresponding intensity-based versions. The performance of the 3D PCT-based methods for curvilinear structure detection was tested on a synthetic image (Figure 4.2), also real biological images of keratins and neuronal networks (Figure 4.3 and Figure 4.4).

A synthetic image was designed to simulate branching structures in a noisy environment. Grid lines with a width of 10 pixels were generated on a bright, constant background. To simulate a real-life scenario, Gaussian noise at 18 SNR was added to the image. Figure 4.2 illustrate the comparison between 3D Hessian- and 3D PCT-based methods when applied to such a synthetic image. As you can notice that, phase-based methods are capable of enhancing fine details compare the traditional methods. Traditional vesselness and neuriteness have issues while enhancing the images. Vesselness cannot detect the cross sections in the biomedical images since both eigenvalues close to zero. Neuriteness enhance the noise as a curvilinear structure and create false curvilinear structures. However, the proposed method is capable of enhancing all curvilinear structures including the fine curvilinear structures and free from all the traditional methods suffers.

Finally, Figure 4.4 demonstrates the comparison results of 3D Hessian- and PCT-based curvilinear structures enhancement methods tested on real biomedical images of structures like microtubules, keratin and neurons (see Figure 4.3). Figure 4.5 demonstrates the ability of proposed methods with the regard of enhancement. While state-of-the-art methods can not enhance the fine curvilinear structures, proposed methods increase the visibility of curvilinear structures in terms of quantitatively and qualitatively.

4.5 Conclusion

Enhancement of the curvilinear structure is important for many biomedical applications. In this research, I have proposed the 3D Phase Congruency Tensor concept used to define 3D contrast-independent curvilinear feature enhancement methods such as PC-vesselness and PCT-neuriteness. Contrary to the 3D Hessian-based intensity-dependent methods, results indicated for the PCT-based approaches show a much higher degree of uniformity in the curvilinear feature enhancement performance. Finally, the 3D PCT concept can be adapted to methods for finding other non-curvilinear structures such as junctions or ending points where high curvature values exist along more than one principal directions. Compare to traditional methods like vesselness and neuriteness, our approach is robust when enhancing low-intensity features in the biomedical images. However, phase congruency can be sensitive to noise.

Epilogue

In this Chapter I have introduced a 3D contrast-independent approach to enhance curvilinear structures based on the 3D Phase Congruency Tensor concept which has shown to be a successful curvilinear structures enhancement approach when compared to other intensity-based state-of-the-art approaches and tested on a variety of synthetic and real images.

Chapter 5

The Multiscale Bowler-Hat Transform for Curvilinear Feature Enhancement in Biomedical Images

Prologue

In Chapter 3 (*p.* 31), I have provided an introduction to mathematical morphology concept for binary and grayscale image processing.

In this Chapter, I will introduce a new mathematical morphology-based approach for image enhancement, specifically the curvilinear features enhancement, called the bowler-hat transform. The proposed method has been evaluated with both synthetic and real biomedical image datasets and quantitatively and qualitatively compared with several state-of-the-art curvilinear features enhancement methods.

Declaration: This Chapter is based on the following publication: Sazak, Ç., Nelson, C. J. & Obara, B. The multiscale bowler-hat transform for blood vessel enhancement in retinal images. *Pattern Recognition* **88,** 739–750 (2019). This Chapter is presented as published, although referencing and notation has been altered and cross-referencing added for consistency throughout this thesis. Some stylistic changes have been made for consistency. The majority of the text is verbatim; however, additions to the body of text are included where they are appropriate.

5.1 Introduction

Many biomedical images contain curvilinear structures, such as blood vessels or cytoskeletal networks [73]. Automated extraction of these structures and their connected network is often an essential step in quantitative image analysis and computer-aided diagnostic pipelines. For example, automated retinal vessel extraction is used for diagnosis, screening, and evaluation in a wide range of retinal diseases, including diabetes and arteriosclerosis [135].

However, for a multitude of reasons, *e.g.* noisy image capture, sample/patient variability, low contrast scenarios, etc., biomedical imaging modalities may suffer from poor quality. As such, standard image segmentation methods are not able to robustly detect curvilinear structures, and therefore some form of curvilinear structure enhancement is required [73].

A wide range of curvilinear structure enhancement methods have been proposed (see [135] and [73] for a recent review). These include Hessian [4, 58, 75], Phase Congruency Tensor [10, 136], mathematical morphology [75, 86, 93], adaptive histogram equalisation [81] based approaches and many others [11, 84, 89, 91, 92, 137–139].

5.1.1 Contribution and Organisation

In this Chapter, I introduce an enhancement method for curvilinear structures based on mathematical morphology concept, which exploits a key shape property of curvilinear structures: the elongation. The proposed method, called the bowler-hat transform, has been qualitatively and quantitatively validated and compared with state-of-the-art methods using a range of synthetic data and publicly available retinal image datasets. The obtained results show that the proposed method achieves high-quality, curvilinear structure enhancement in both synthetic examples and clinically relevant retinal images. Retinal vessels can be considered as dark vessels on a bright background or, when the image is simply inverted, as bright vessels on a dark background. For the purposes of clarity in description and visualisation, I assume, and our methods work for, bright vessels on a dark background; this is similar to other methods [4]. The proposed method is suitable for a range of biomedical image types without needing prior training or tuning.

The rest of this Chapter is organised as follows. Section 5.2 introduces and explains the proposed bowler-hat transform, Section 5.3 presents validation experiments and results on synthetic and real data. Finally, in Section 5.4, I discuss the results and future work.

5.2 Method

In this Section, I introduce a novel, mathematical morphology-based method for curvilinear structure enhancement in images: the bowler-hat transform. I highlight the key concepts that allow this method to address the major drawbacks of existing, state-of-the-art, methods.

5.2.1 Proposed Method

Figure 5.2 presents a flow diagram of the proposed method which combines the outputs of morphological operations upon an image carried out with two different banks of structuring elements: one bank of disk elements with varying radii, and one bank of line elements with varying radii and rotation. The bowler-hat transform name is influenced coming from the bank of disk elements (forming the bowl) and

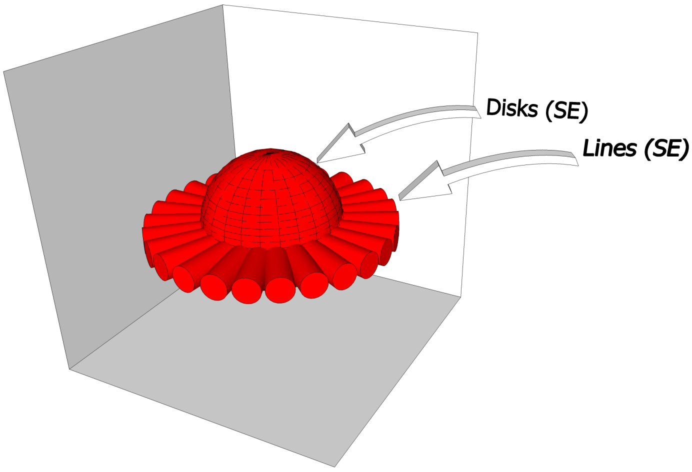

Figure 5.1: The bowler-hat transform name is inspired by the 'bowler-hat' shape defined by the disk element (forming the bowl) and the set of line elements (forming the brim).

the bank of line elements (forming the brim), see Figure 5.1.

For a given grayscale input image, I, it has been carried out a series of morphological openings with a bank of disk-shaped structuring elements, b_s of diameter $s \in [1, s_{max}]$ pixels, where s_{max} is the expected maximum curvilinear structure size and user-defined parameter. This produces a stack of images, for all s, such that;

$$\{I_{disk}\} = \{I \circ b_s \colon \forall s \in [1, s_{\max}]\}\,. \tag{5.1}$$

In each I_{disk} image, curvilinear structure segments wider than s remain and those segments smaller than s are removed.

I also produce a similar stack of images using a bank of line-shaped structuring elements, $b_{s,\theta}$; each line-shaped is of length $s \in [1, s_{max}]$, with a width of 1 pixel, and orientation $\theta \in [0, 180)$, θ_{sep} is angle step.

As a result, curvilinear structure segments that are longer than s and along the direction defined by θ will remain, and those shorter than s or along the direction defined by θ will be removed. For each line length s I produce a stack of images for all orientations defined by $\theta \in [0, 180)$. Then, for each s, I calculate a single image,

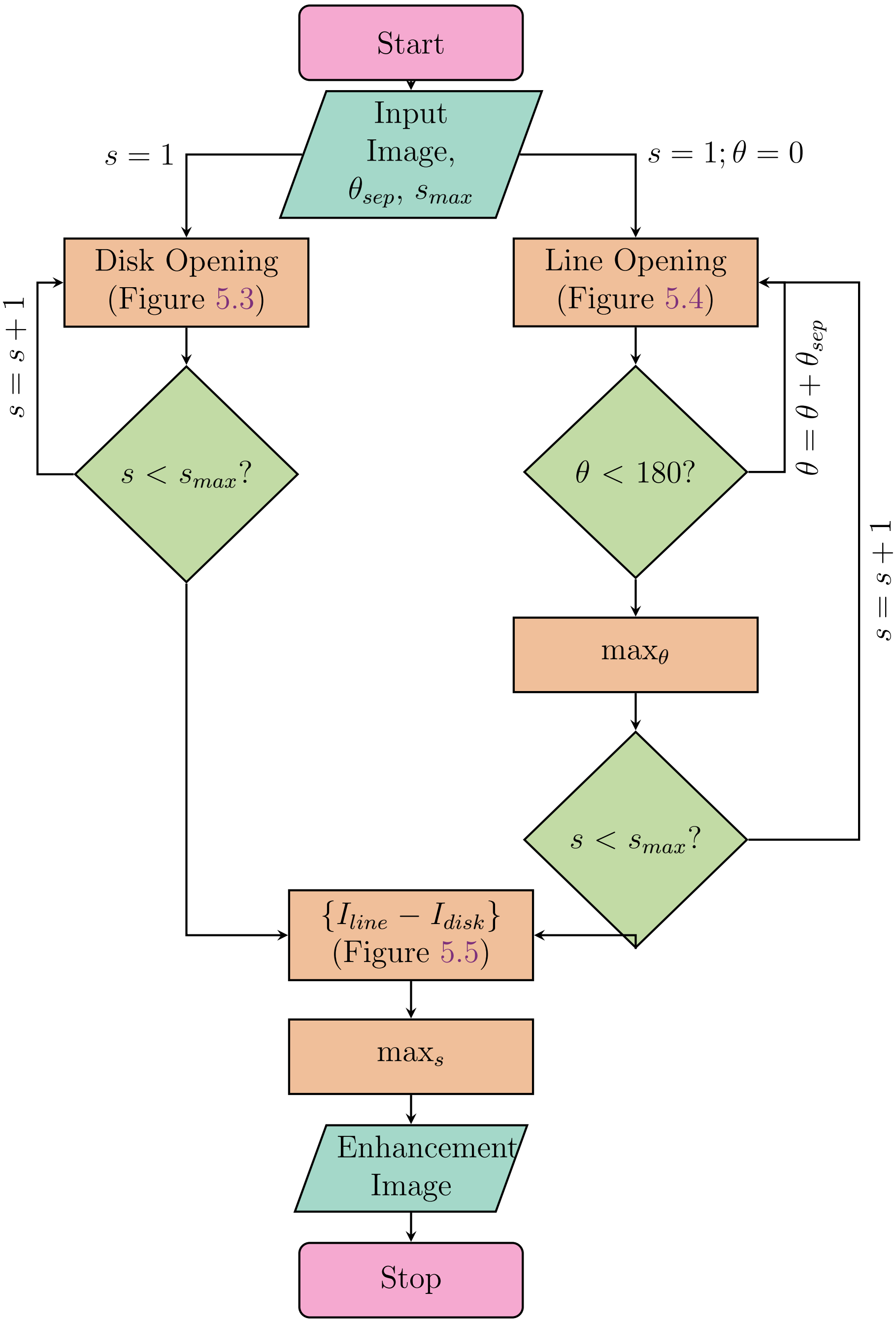

Figure 5.2: Flow chart of the bowler-hat transform showing how two banks of images are created using disk SEs (left route; Figure 5.3) and line SEs (right route; Figure 5.4) of different scales and, for the line elements, rotations. These banks are then combined in a multiscale fashion (Figure 5.5) before forming a single enhancement image.

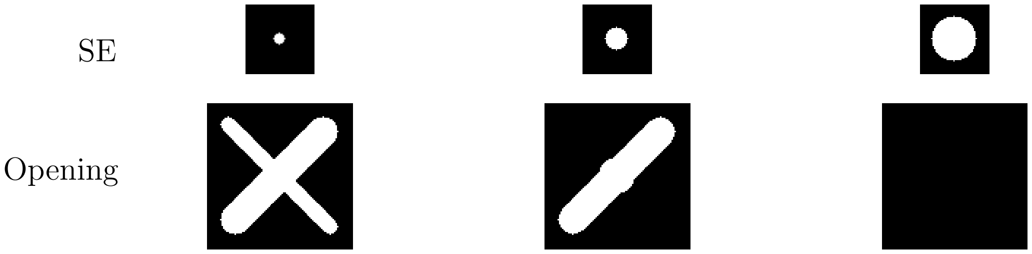

(a) A SE smaller than any features in the input image

(b) A SE bigger than some features but smaller than others

(c) A SE bigger than all features in the image

Figure 5.3: Example openings with disk SEs of various sizes. The set of all openings with disks of differing size represents the left route in Figure 5.2. Reprinted with permission from [140].

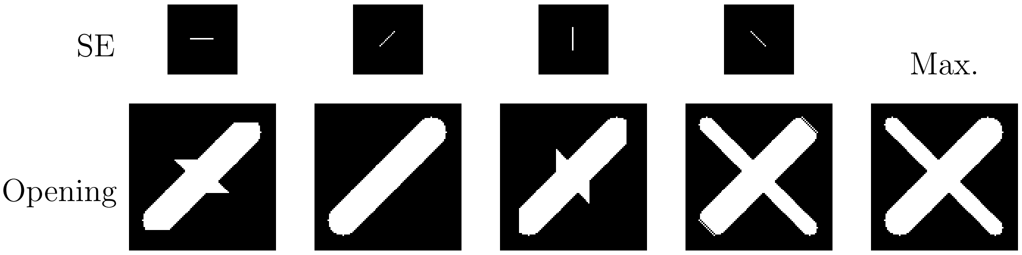

(a) A SE longer than the width of some features in the image

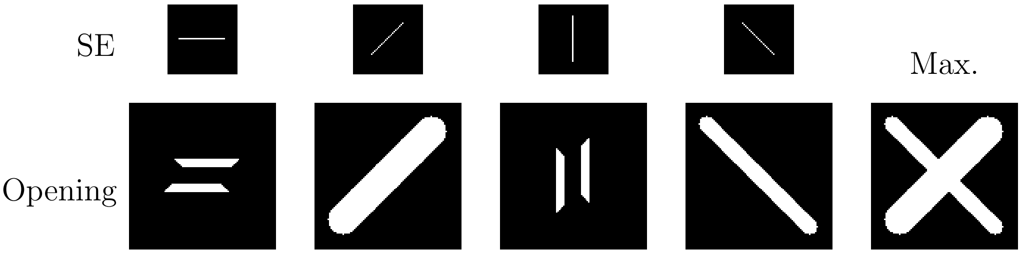

(b) A SE longer than the width of most features in the image. Note how those features aligned with the SE are not attenuated during opening

Figure 5.4: Example openings with line SEs of various lengths and rotations. The set of all openings with lines of differing length and rotation represents the left route in Figure 5.2. In this extremely simple case the maximum (right hand column) includes values at all features. Reprinted with permission from [140].

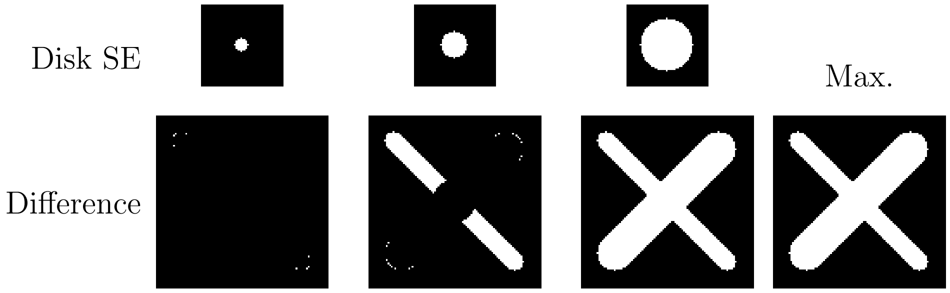

(a) A SE smaller than any features in the input image

(b) A SE bigger than some features but smaller than others

(c) A SE bigger than all features in the image

(d) Element-wise maximum over differences at all scales

Figure 5.5: Example differences between disk openings and maximum (over orientation) line openings of various sizes. The set of all differences represents the coming together of the two routes in Figure 5.2. Disk SEs are shown to give an idea of scale. The maximum (far right) represents the enhanced image. Reprinted with permission from [140].

I_{line} as a pixel-wise maximum of the stack such that;

$$\{I_{line}\} = \left\{\max_{\theta}\left(\{I \circ b_{s,\theta} \colon \forall\theta\}\right) : \forall s \in [1, s_{\max}]\right\}. \tag{5.2}$$

These two stacks, $\{I_{disk}\}$ and $\{I_{line}\}$, are then combined by taking the stack-wise difference, the difference between the maximum opening with a line of length s across all angles and an image formed of opening with a disk of size s, to form the enhanced image. The final enhanced image is then formed from maximum difference at each pixel across all stacks;

$$I_{enhanced} = \max_{s}(|I_{line} - I_{disk}|). \tag{5.3}$$

Pixels in the background, *i.e.* dark regions, will have a low value due to the use of openings; pixels in the foreground of blob-like structures will have a low value as the differences will be minimal, *i.e.* similar values for disk-based and line-based openings; and pixels in the foreground of curvilinear structures will have a high value, *i.e.* large differences between longer line-based openings and disk-based openings.

The combination of line and disk elements gives the proposed method a key advantage over the existing methods. Given an appropriate s_{max}, *i.e.* larger than any curvilinear structures in the image, a junction should appear bright like those curvilinear structures joining that junction, something that many other curvilinear structure enhancement methods fail to do. This is due to the ability to fit longer line-based structuring elements within the junction area. As a result, the curvilinear structure network stays connected when enhanced and segmented, especially at junctions.

In Section 5.3, I demonstrate, qualitatively and quantitatively, the key advantages of the bowler-hat transform over the existing, state-of-the-art curvilinear structure enhancement methods.

5.2.2 Implementation and Computation Time

All codes were implemented and written in MATLAB 2016b [141] on Windows 8.1 Pro 64-bit PC running an Intel Core i7-4790 CPU (3.60 GHz) with 16 GB RAM. The source code is available in a GitHub repository https://github.com/CigdemSazak/bowler-hat-2d.

The average computation time for the proposed method is 3.8 seconds for DRIVE image and 4.9 seconds for STARE image. Please make a note that the proposed method has been implemented and tested in MATLAB, however, C++ implementation could be much faster.

5.3 Results

In this Section, the proposed method is qualitatively and quantitatively validated and compared with the existing state-of-the-art methods using synthetic and clinically relevant, retinal image datasets, with human-annotated ground truths, and other biomedical images.

As with any image processing method, an understanding of how the parameters involved affect the result is essential. In general, I have found the bowler-hat transform to be robust, usually requiring 10–12 θ orientations for line structuring element and the size of the disk/line structuring element d to be greater than the thickest vessel structure in an image.

The following Sections are organised as follows: first, I visually and qualitatively analyse the bowler-hat transform and compare with alternative methods in Section 5.3.1, Section 5.3.3, Section 5.3.2. Second, I use real-world fundus images, with human-created ground truths, to compare these methods in Section 5.3.4. I evaluate these results in a quantitative and comparable manner using the Receiver Operating Characteristic (ROC) curve and the Area Under the Curve (AUC) metric. All the images were normalised after each enhancement approach such that the brightest pixel in the whole image has a value of 1 and the darkest a value of 0.

5.3.1 Profile Analysis

The effect of the curvilinear structure enhancement methods on a simple curvilinear structure is shown in Figure 5.6. This represents the simplest example of a vessel in an image, like those found in retinal images. Figure 5.6 illustrates the normalised, intensity profile for images enhanced with each of the methods. As the Figure 5.6 clearly shows, the enhancement methods tend to expand or shrink the curvilinear structures. Moreover, while the Hessian-based methods have an enhanced signal at the center of the vessel, *i.e.* a peak value of one at the vessels centre-line, their value quickly drops off and decreases the perceived thickness of the vessel. The proposed method has both these benefits: a maximal peak value at the vessel centre-line and an enhanced response to the edges of the vessel. As a result, reliable vessel thickness can be captured.

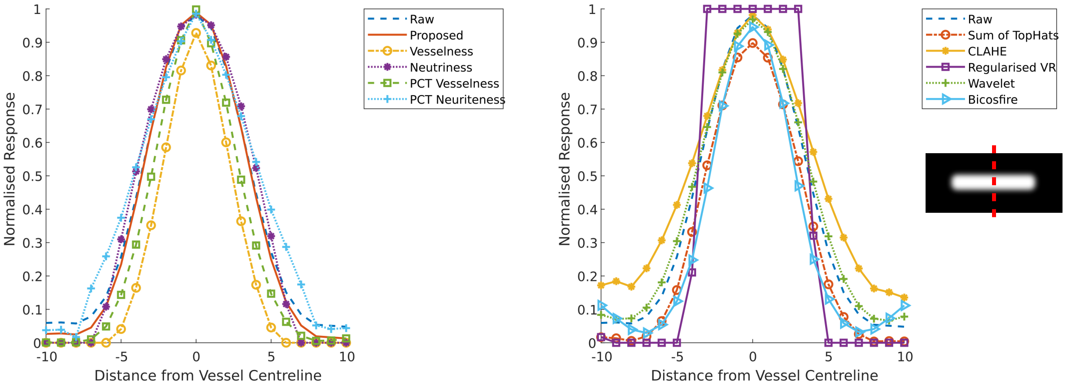

Figure 5.6: Cross-sectional profiles of a synthetic vessel input image and the input image enhanced with the state-of-the-art (see legend for colours) curvilinear structure enhancement methods and the proposed bowler-hat curvilinear structure enhancement method. All the images are normalised such that the brightest pixel in the whole image has a value of 1 and the darkest a value of 0. Some of the methods enhance the whole curvilinear structure but still create noise as like in CLAHE, some of them extend the vessel structure like PCT-neuriteness or shrink as like vesselness. However, the proposed method enhances the curvilinear structure as a foreground data, and detect background as an unnecessary data.

5.3.2 Response to Uneven Background Illumination

Figure 5.7 presents the response of the proposed method to an uneven illumination scenario. Key features such as junctions are preserved and appear unaffected by even severe illumination problems. This ability to preserve junctions under uneven illumination is important for many real applications of curvilinear structure enhancement and the proposed method is able to do this, unlike the current state-of-the-art methods.

5.3.3 Response to Vessels, Intersections, and Blobs

Figure 5.8 presents a qualitative comparison between the proposed method and the state-of-the-art methods when applied to synthetic images and real images with curvilinear, intersection-like, and blob-like structures. Key issues that occur across the state-of-the-art methods include defects at junctions (purple arrows),

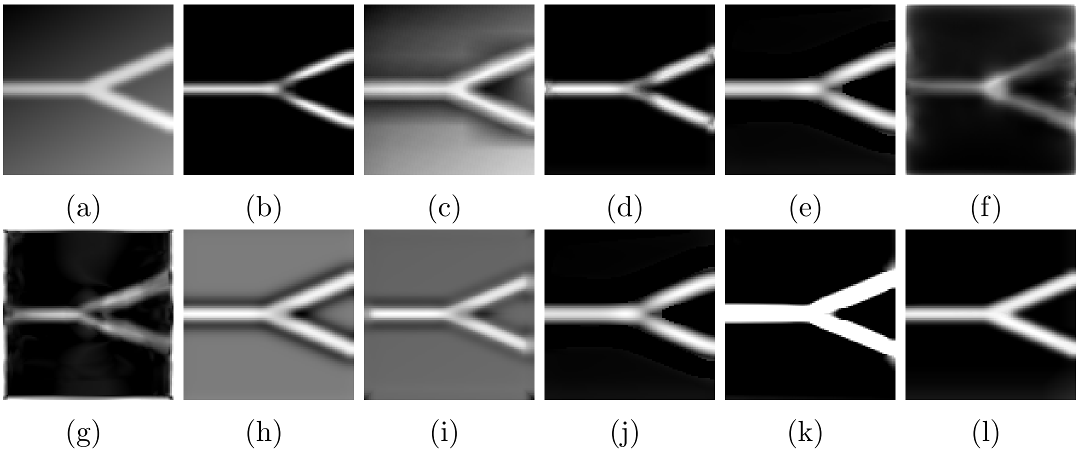

Figure 5.7: Comparison of the curvilinear structure enhancement methods' abilities to deal with uneven background illumination. (a) an input image, (b) vesselness, (c) CLAHE, (d) Zana's top-hat, (e) neuriteness, (f) PCT-vesselness, (g) PCT-neuriteness, (h) wavelet, (i) line detector, (j) volume ratio, (k) SCIRD-TS, and (l) the bowler-hat. Most of the methods have not affected by the background illumination and enhance the curvilinear structures as the manner of perfect enhancer, however, (b, d, f, g, i) are have blurs at the curvilinear structure edges, shrink the curvilinear structures or create shades. For instance, (j, k) and (l) perfectly enhance the vessels.

noise enhancement, tip artefacts (orange arrows) and loss of signal (yellow arrows). These issues are all absent from our proposed method. However, a shortcoming of our approach is shown in Figure 5.8- row 4, which shows a curvilinear structure with an attached 'blob' (green arrow), a perfect curvilinear structure enhancement method would enhance all of the linear structure and none of the blob. While none of the compared approaches act in this ideal manner, many of the methods show a clear difference between the blob response and vessel response.

5.3.4 Real Data - Retinal Image Datasets

In this Section, I show the quality of the proposed method validated on three publicly available retinal image datasets: the DRIVE, STARE, and HRF databases. These datasets have been chosen because of their availability and their ground truth data. I have used these ground truth segmentations to quantitatively compare the proposed method with the other curvilinear structure enhancement methods.

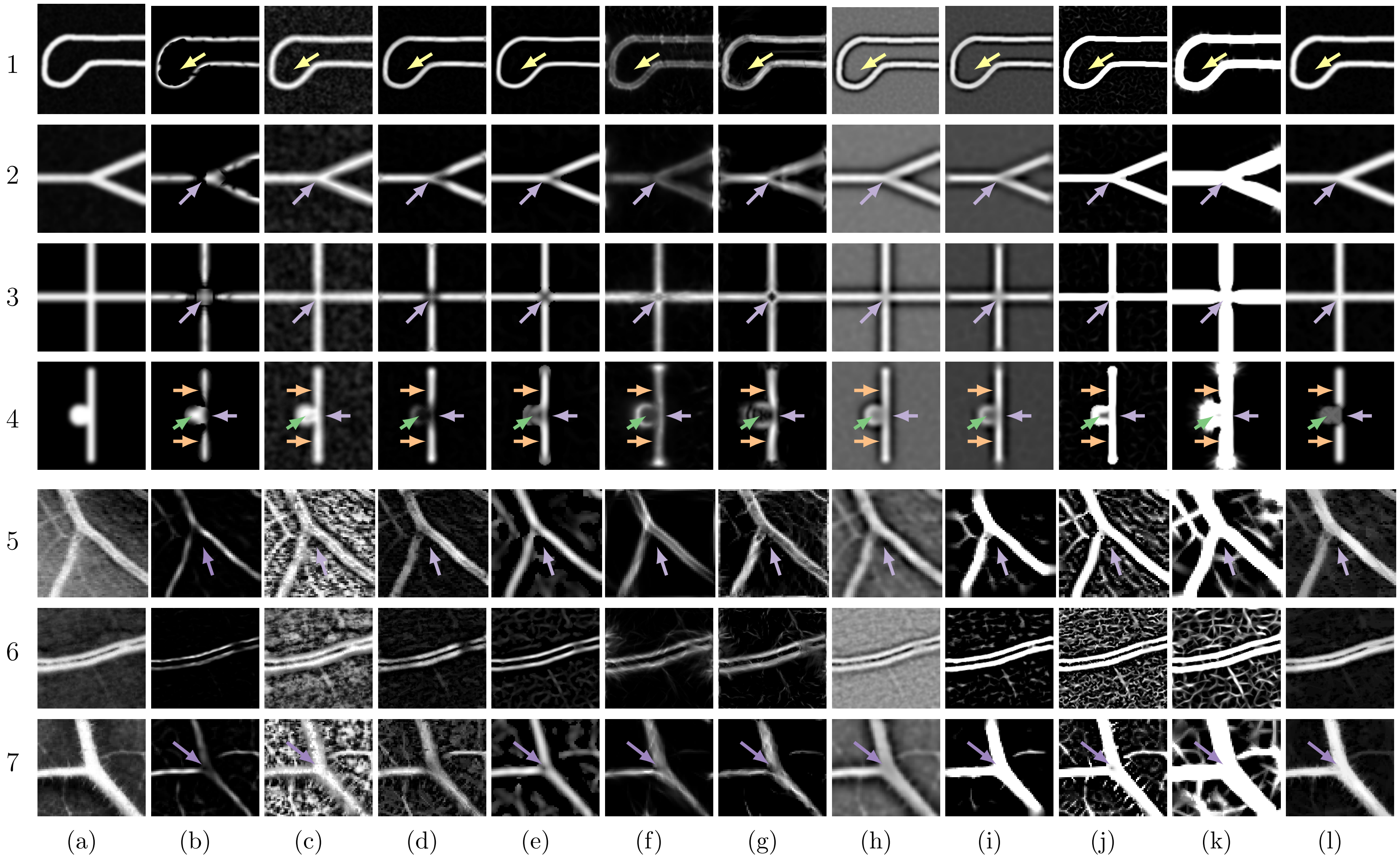

Figure 5.8: The bowler-hat transform enhances curvilinear structures, maintaining junctions and tips while suppressing blobs. A comparison of the enhancement of curvilinear and other structures using the proposed method and the state-of-the-art methods. (a) shows the original images, all curvilinear structures have a thickness of 9 pixels and the 'blob' in 4 has a diameter of 21 pixels. The first four rows are synthetic images that indicate possible curvilinear structures in biomedical images. The last three rows illustrate curvilinear structures from real biomedical images. Row 5 is a cropped region from the DRIVE dataset, while row 6 is curvilinear structure section of the healthy images in the HRF dataset. The last row is another cropped region from the leaf image [10]. Results for (b) vesselness, (c) CLAHE, (d) Zana's top-hat, (e) neuriteness, (f) PCT-vesselness, (g) PCT-neuriteness, (h) wavelet, (i) line detector, (j) volume ratio, (k) SCIRD-TS, and (l) the bowler-hat. Arrows indicate features of interest: vessel structures (yellow arrows), junctions (purple), blob-like features (green), and tips (orange).

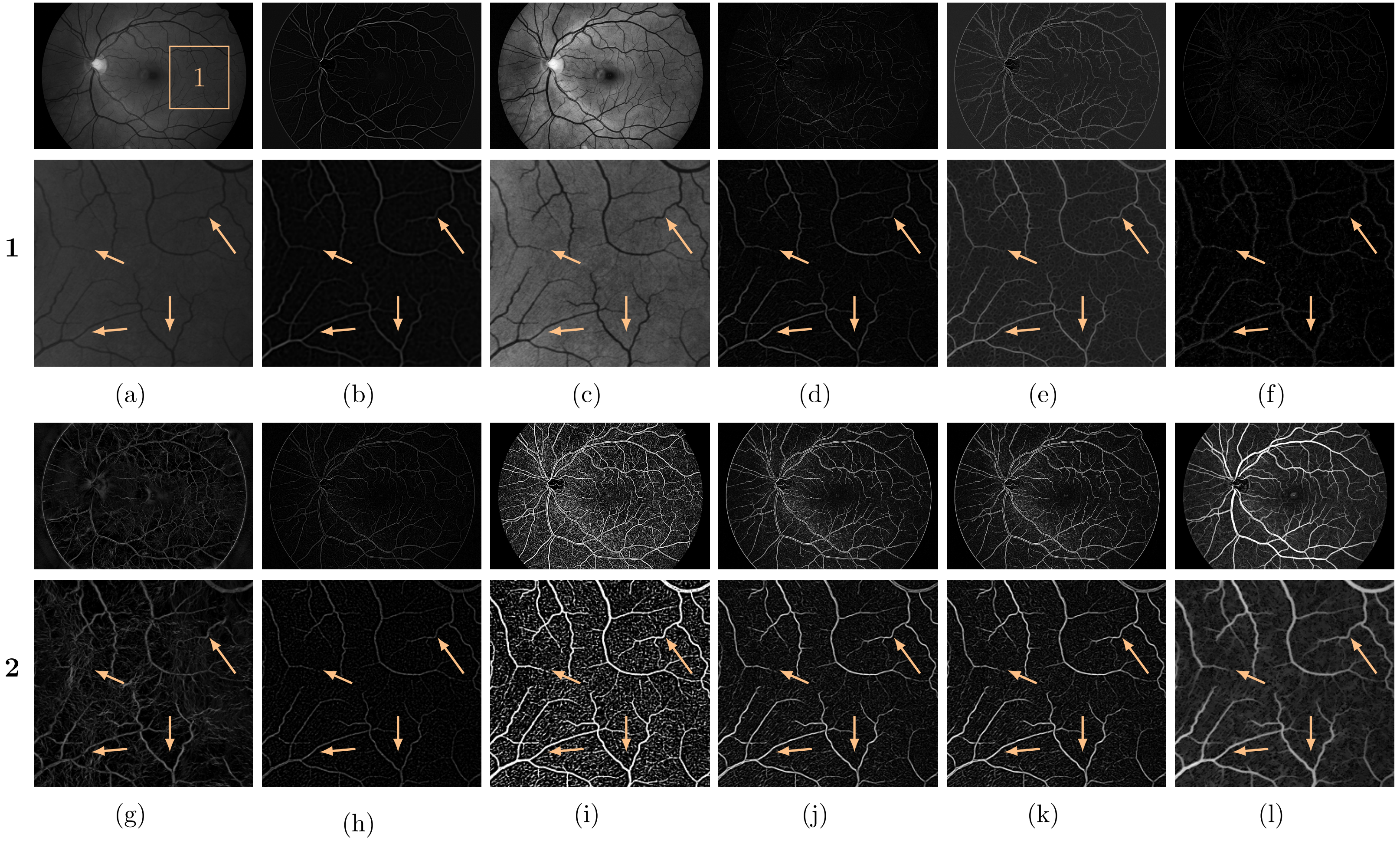

Figure 5.9: A comparison of the curvilinear structure enhancement results for a sample image from HRF dataset. (a) an input image. The zoomed in the region (1) and (2) shows enlarged image ROI in the square of the raw image. The arrows point to key areas of interest, such as junctions, fine tips and curvilinear structures not captured by all methods. Respectively, (b) vesselness, (c) CLAHE, (d) Zana's top-hat, (e) neuriteness, (f) PCT-vesselness, (g) PCT-neuriteness, (h) wavelet, (i) line detector, (j) volume ratio, (k) SCIRD-TS, and (l) the bowler-hat. All the state-of-the-art methods behave can be seen here. (b) vesselness and (e) neuriteness can enhance while not possible to by qualitatively. However, the some of the methods can be distinguishable by qualitatively such as (j) volume ratio and (l) the bowler-hat. More quantitative details can be seen Table 5.1.

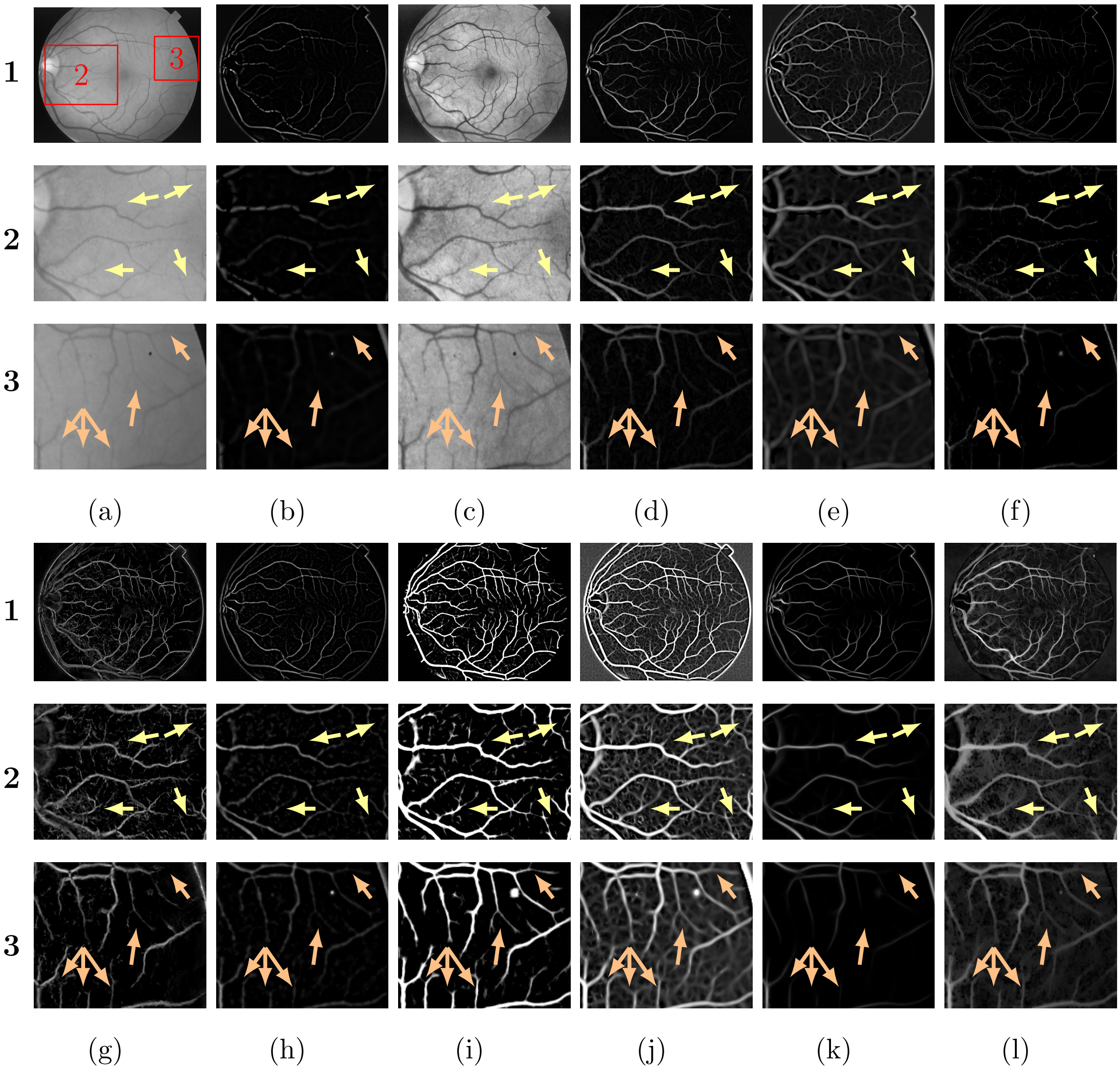

Figure 5.10: A comparison of the curvilinear structures enhancement results for a sample image from the STARE dataset. The zoomed in regions of interest (red boxes 2 and 3) show areas both near the optic disk, with thick vasculature, and far from the disk, where curvilinear structures are much fine and more branching in 1. The arrows point to key areas of interest, such as junctions, fine tips and curvilinear structures not captured by all methods. (a) an input image, (b) vesselness, (c) CLAHE, (d) Zana's top-hat, (e) neuriteness, (f) PCT-vesselness, (g) PCT-neuriteness, (h) wavelet, (i) line detector, (j) volume ratio, (k) SCIRD-TS, and (l) the bowler-hat. (Notation for numeric labels: 1 - full image; 2 - 2^{nd} regions of interest; 3 - 3^{rd} regions of interest.)

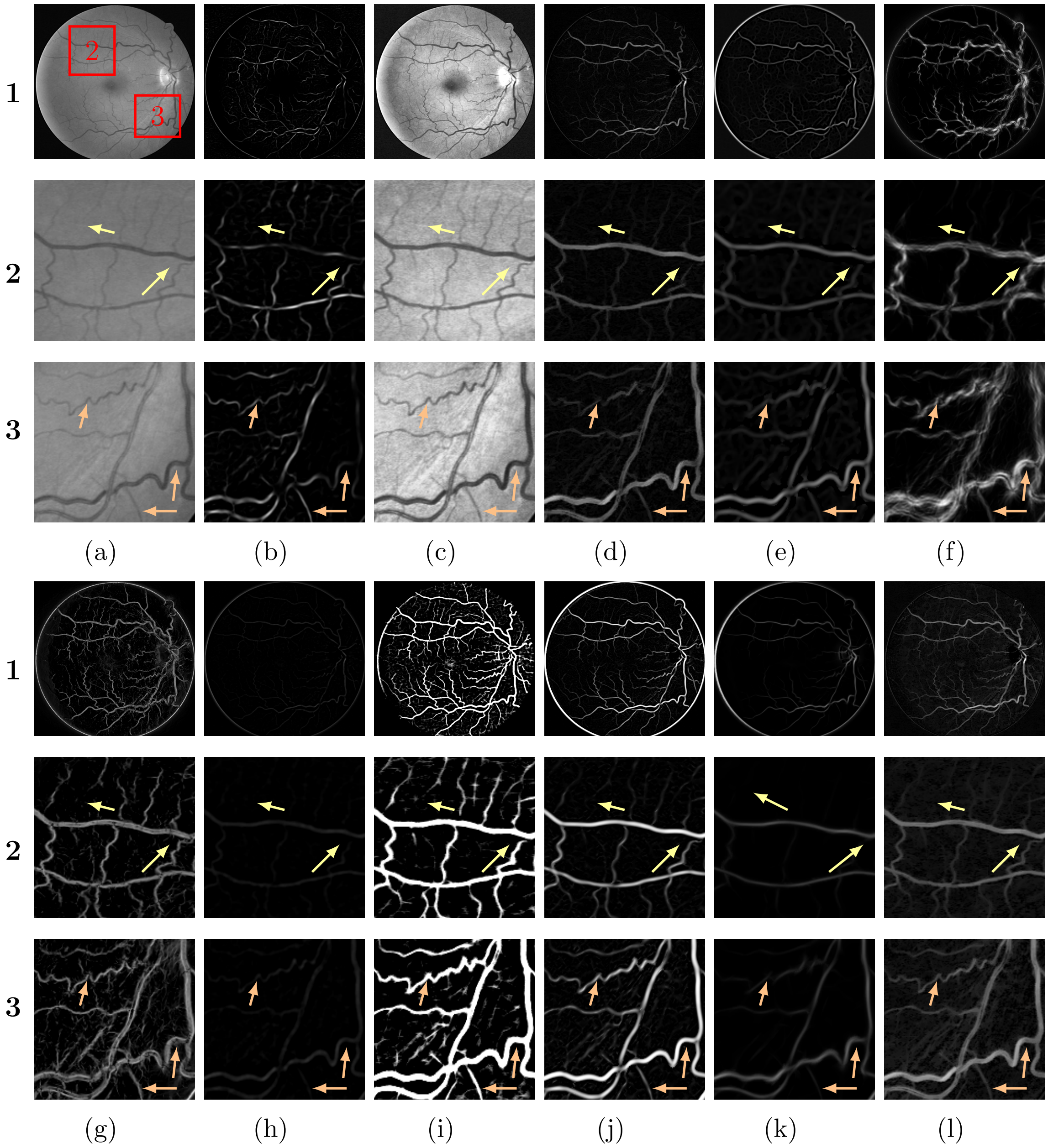

Figure 5.11: A comparison of the curvilinear structures enhancement results for a sample image from the DRIVE dataset. The zoomed in regions of interest (red boxes 2 and 3) show areas both near the optic disk, with thick vasculature, and far from the disk, where curvilinear structures are much fine and more branching in 1. The arrows point to key areas of interest, such as junctions, fine tips and curvilinear structures not captured by all methods. (a) an input image, (b) vesselness, (c) CLAHE, (d) Zana's top-hat, (e) neuriteness, (f) PCT-vesselness, (g) PCT-neuriteness, (h) wavelet, (i) line detector, (j) volume ratio, (k) SCIRD-TS, and (l) the bowler-hat. (Notation for numeric labels: 1 - full image; 2 - 2^{nd} regions of interest; 3 - 3^{rd} regions of interest.)

The Digital Retinal Images for Vessel Extraction (DRIVE) [41] dataset is a published database of retinal images for research and educational purposes. The database consists of twenty colour images that are JPEG compressed, as for many screening programs. These images were selected randomly from a screening of 400 diabetic subjects between the ages of 25 and 90. The ground truth provided with this dataset consists of manual segmentation of the vasculature for each image. Ground truths were prepared by trained observers, and 'true' pixels are those for which observers where $> 70\%$ certain.

The Structured Analysis of the REtina (STARE) dataset is another publicly available database [142] containing twenty colour images with human-determined vasculature ground truth. I have compared all these images against the AH labelling.

The High-Resolution Fundus (HRF) image dataset [3] consists of 45 retinal images. This dataset has three types of subjects include healthy, diabetic retinopathy, and glaucoma.

Quantitative Validation - Enhancement

While a visual inspection can give some information regarding the effectiveness of the curvilinear structure enhancement methods, a form of quantitative validation is required. Therefore, as proposed in [143], I have used the Receiver Operating Characteristic (ROC) curve and the Area Under the Curve (AUC) to compare the curvilinear structure enhancement methods. To derive the ROC curve and then the AUC value is calculated, each enhanced image is segmented at different thresholds and compared with the corresponding ground truth segmentation (see Figure 5.12).

The AUC metric measures vessel segmentation accuracy directly but it also measures the curvilinear structure enhancement accuracy indirectly by giving us an indication of the enhancement contribution to the final segmentation result. Please note that, before any quantitative evaluation, all the enhanced retinal images were masked

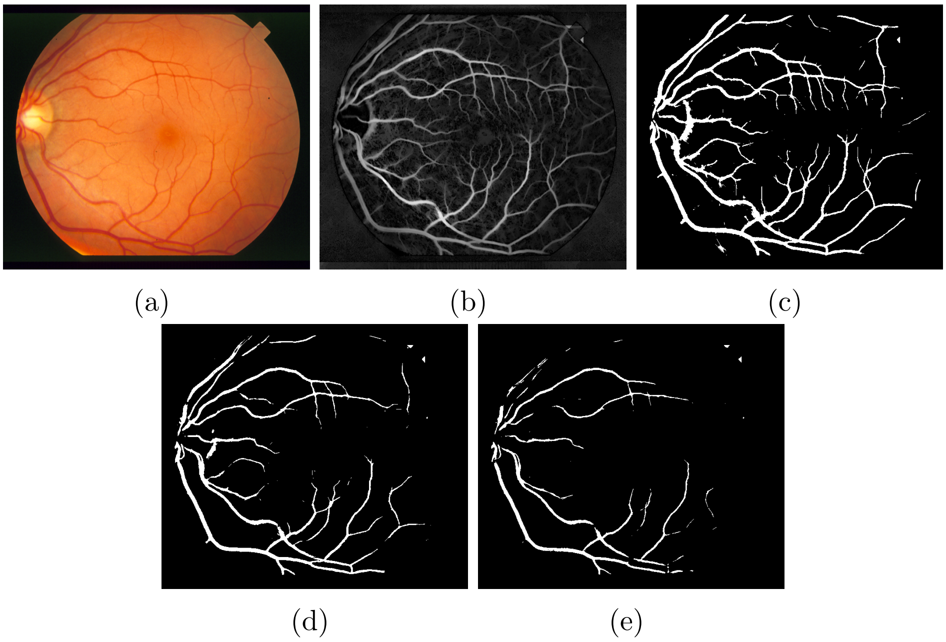
(a) (b) (c)
(d) (e)

Figure 5.12: Exemplary image from STARE dataset segmented with the different threshold levels. (a) is an input image, (b) is the image enhanced by the bowler-hat transform, (c-e) are segmented images with threshold levels: (c) 0.2, (d) 0.3, (e) and 0.4.

with the mask images provided with the retinal image datasets (see Figure 5.13).

Quantitative Validation - Segmentation

To quantitatively evaluate the robustness of the vessel segmentation methods, sensitivity (SN), specificity (SP), and accuracy (ACC) metrics are calculated for each segmented image and its corresponding ground truth segmentation, as follows;

$$\text{SN} = \frac{TP}{TP + FN}, \tag{5.4}$$

$$\text{SP} = \frac{TN}{TN + FP}, \tag{5.5}$$

$$\text{ACC} = \frac{TP + TN}{TP + TN + FP + FN}, \tag{5.6}$$

where TP is the true positive count, FP the false positive count, TN the true negative and FN the false negative counts of the segmented pixels. I used these

(a) Original (b) Green channel (c) Enhanced

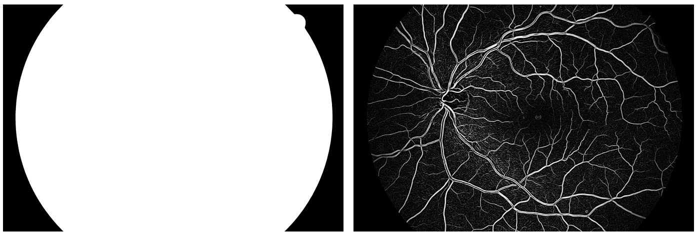

(d) Mask (e) Enhanced and masked

Figure 5.13: All the enhanced retinal images are masked before any quantitative validation. (a) is a retinal image from the HRF dataset, (b) demonstrates the green channel of input image, (c) is the image enhanced by volume ratio, (d) is the mask provided in the HRF dataset, and finally (e) is the enhanced image after masking.

Enhancement Method	AUC (Std)				
	Year/Ref	DRIVE	STARE	HRF(healthy)	HRF(unhealthy)
Raw image	-	0.416 (0.064)	0.490 (0.076)	0.530 (0.075)	0.541(0.073)
Vesselness	1998 [4]	0.888 (0.013)	0.898 (0.015)	0.913 (0.020)	0.904 (0.020)
CLAHE	1998 [81]	0.862 (0.068)	0.880 (0.087)	0.867 (0.025)	0.835 (0.023)
Zana's top-hat	2001 [86]	0.933 (0.015)	0.956 (0.021)	0.943 (0.010)	0.91 (0.016)
Neuriteness	2004 [8]	0.909 (0.022)	0.927 (0.039)	0.896 (0.024)	0.879 (0.059)
PCT-vesselness	2012 [10]	0.890 (0.037)	0.899 (0.056)	0.888 (0.011)	0.837 (0.030)
PCT-neuriteness	2012 [10]	0.817 (0.021)	0.827 (0.065)	0.901 (0.029)	0.777 (0.022)
Wavelet	2012 [11]	0.921 (0.013)	0.935 (0.015)	0.829 (0.021)	0.740 (0.026)
Line detector	2013 [84]	0.926 (0.019)	0.954 (0.016)	0.858 (0.020)	0.734 (0.026)
Volume ratio	2016 [9]	0.936 (0.013)	0.956 (0.012)	0.927 (0.018)	0.823 (0.026)
SCIRD-TS	2016 [100]	0.925 (0.012)	0.946 (0.021)	0.956 (0.012)	0.692 (0.035)
Bowler-hat	2019 [18]	**0.946 (0.032)**	**0.962 (0.034)**	**0.968 (0.015)**	**0.944 (0.016)**

Table 5.1: Mean AUC values calculated as described in Section 5.3.4, for the images across the DRIVE, STARE and HRF datasets enhanced by the bowler-hat and the state-of-the-art methods. The best results for each dataset are in bold. Individual ROC curves can be seen in Figure 5.14.

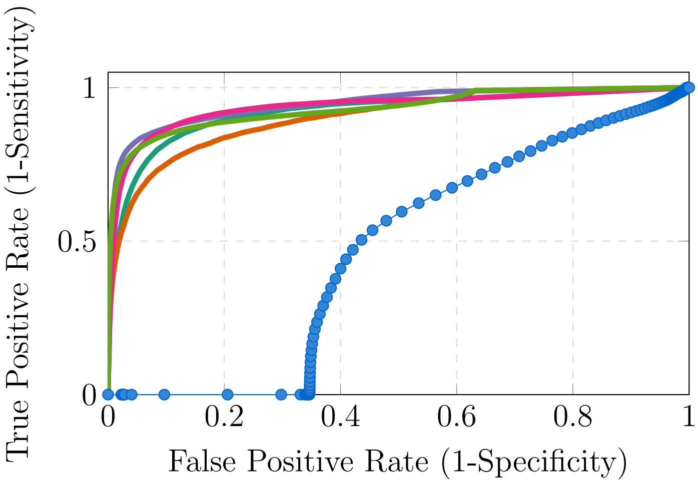

(a) DRIVE

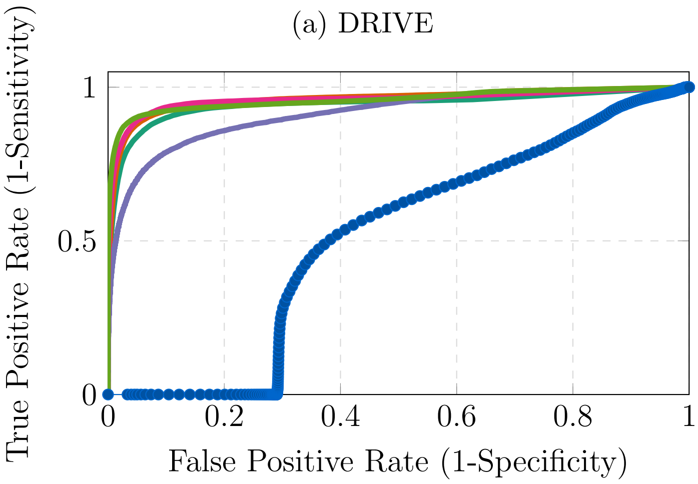

(b) STARE

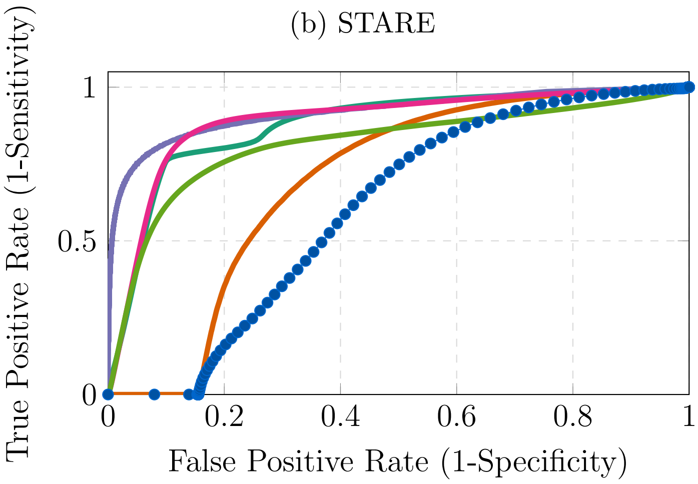

(c) HRF

Figure 5.14: ROC curves calculated for sample images from the (a) DRIVE, (b) STARE, and (c) HRF datasets enhanced by the proposed and the state-of-the-art methods (see legend for colours). Corresponding mean AUC values can be found in Table 5.1. (Note: Rest of the methods results can be seen Figure 5.15.)

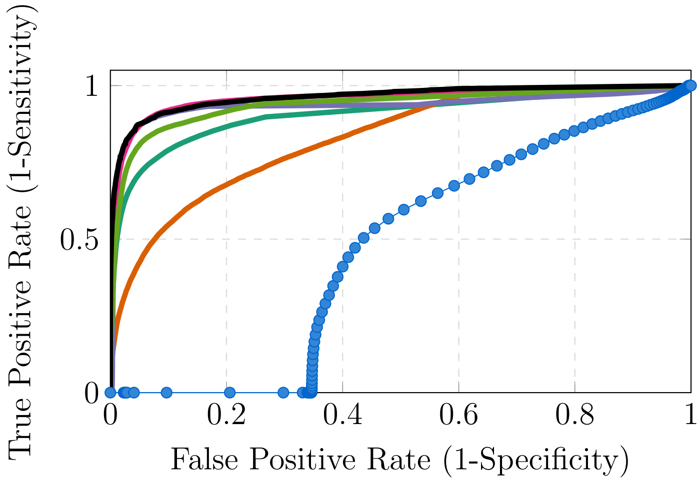

(a) DRIVE

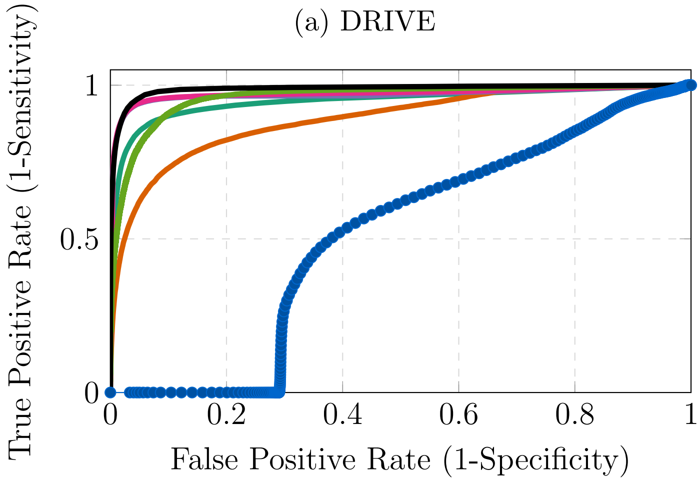

(b) STARE

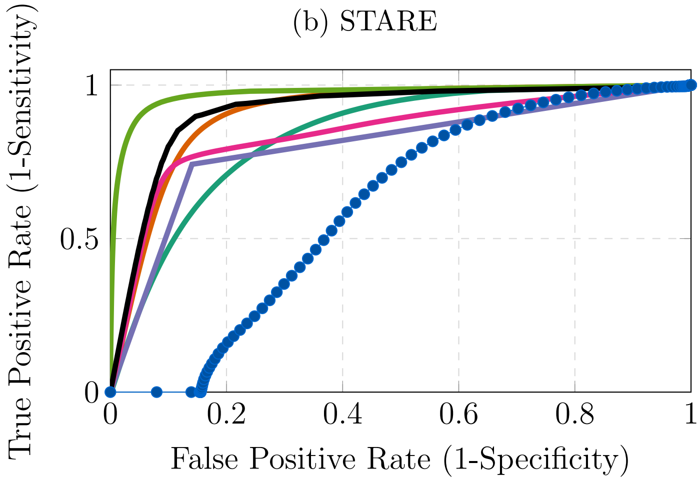

(c) HRF

Figure 5.15: ROC curves calculated for sample images from the (a) DRIVE, (b) STARE, and (c) HRF datasets enhanced by the proposed and the state-of-the-art methods (see legend for colours). Corresponding mean AUC values can be found in Table 5.1.

metrics in Table 5.2 and Table 5.3.

Healthy Subjects

Figure 5.9 shows the results of the proposed and state-of-the-art methods applied to a sample image from the HRF dataset (results for DRIVE Figure 5.11 and STARE Figure 5.10).

I can see that the proposed method is able to enhance finer structures as detected by the human observer but not emphasised by many of the other methods (see arrows).

I can also see that, whilst the connectivity seems to be maintained (unlike in Figure 5.9b), 'false vessels' are not introduced (*c.f.* Figure 5.9e).

Finally, Figure 5.14, Figure 5.15 and Table 5.1 present ROC curves and mean AUC values for the enhancement results of the proposed and state-of-the-art methods applied to all images across the DRIVE, STARE and HRF datasets by using the quantitative validation as described Section 5.3.4.

Unhealthy Subjects

Figure 5.16 presents a visual comparison of the enhancement methods applied to sample images of subjects with diabetic retinopathy and with glaucoma from the DRIVE, STARE and HRF datasets. As it can be noticed in Figure 5.16i, the proposed method is sensitive to noisy regions. This issue can be addressed by the use of a line-shaped morphological structuring element with a varying thickness. Even so, the proposed method achieved the highest overall score on the HRF unhealthy images as illustrated in Table 5.1.

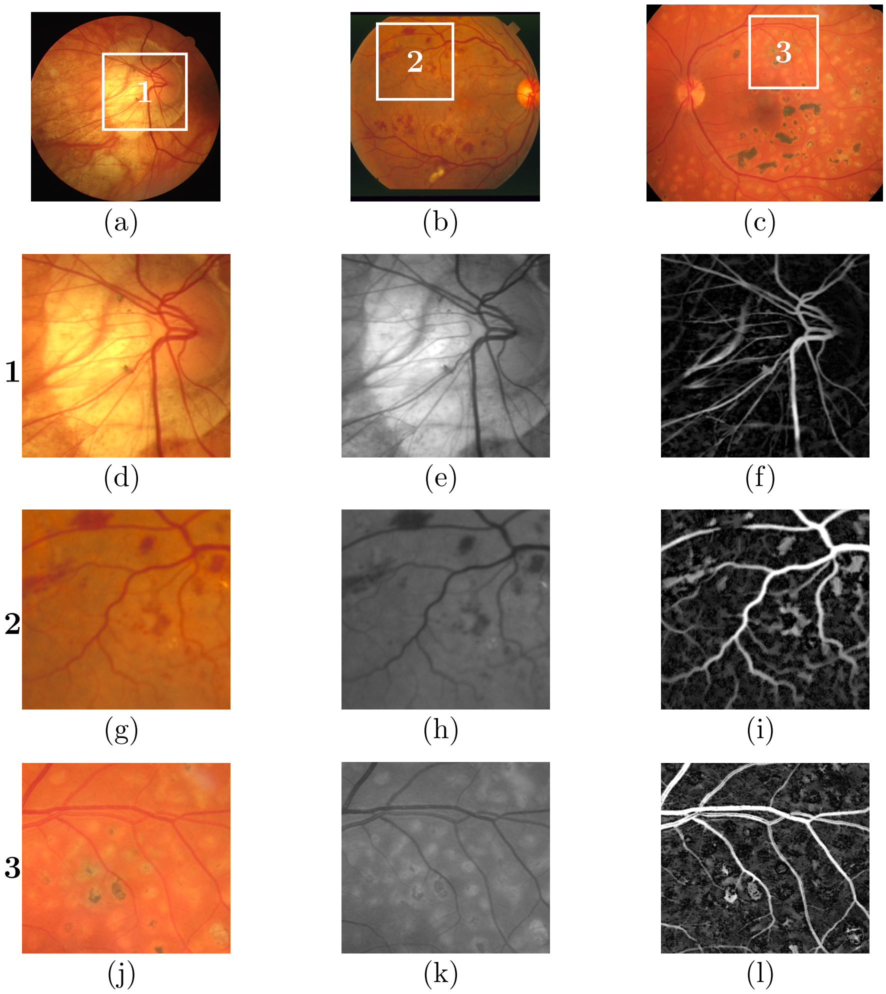

(a) (b) (c) (d) (e) (f) (g) (h) (i) (j) (k) (l)

Figure 5.16: The bowler-hat applied to the retinal images of unhealthy subjects from (a) DRIVE, (b) STARE and (c) HRF datasets. (d, g, j) are the input images with the region of interest. (e, h, j) illustrate the green channel of input image (f, i, l) demonstrate the enhancement result of the curvilinear structure on the abnormal area. Notice that, proposed method is able to enhance curvilinear structures even fine structures. However, problematic areas are also enhanced too. (Notation for numeric labels: 1 - full image; 2 - 2^{nd} regions of interest; 3 - 3^{rd} regions of interest.)

Enhancement with Global and Local Thresholding

Figure 5.17 demonstrates the vessel segmentation results obtained by the proposed and the state-of-the-art curvilinear structures enhancement methods followed by the same global and local thresholding approaches proposed in [144, 145] when applied to the HRF dataset images. The quantitative comparison of the vessel segmentation

Enhancement Method		ACC (Std)	
		Global	Local
	Year/Ref	HRF	HRF
Vesselness	1998 [4]	0.936(0.006)	0.951(0.006)
CLAHE	1998 [81]	0.668(0.051)	0.859(0.009)
Zana's top-hat	2001 [86]	0.925(0.016)	0.946(0.008)
Neuriteness	2004 [8]	0.948(0.005)	0.953(0.006)
PCT-vesselness	2012 [10]	0.892(0.015)	0.926(0.007)
PCT-neuriteness	2012 [10]	0.916(0.013)	0.900(0.008)
Wavelet	2012 [11]	0.672(0.037)	0.946(0.006)
Line detector	2013 [84]	0.902(0.008)	0.957(0.006)
Volume ratio	2016 [9]	0.936(0.012)	0.947(0.011)
SCIRD-TS	2015 [100]	0.947(0.008)	0.951(0.010)
Bowler-hat	-	**0.960(0.005)**	**0.961(0.005)**

Table 5.2: Mean ACC values with the standard deviation for curvilinear structures segmentation results obtained by the proposed and the state-of-the-art curvilinear structures enhancement methods followed by the same global thresholding approach proposed in [144] and local thresholding approach proposed in [145] when applied to the HRF dataset images. The best results are in bold.

results obtained is presented in Table 5.2.

Comparison with Other Segmentation Methods

To highlight the effectiveness of the proposed curvilinear structure enhancement method (combined with the local thresholding approach [145]) for a full vessel segmentation, I compared the performance of our method with seventeen state-of-the-art vessel segmentation methods reported in the literature [3, 11, 32, 41, 68, 84, 89, 116, 146–154] applied to DRIVE, STARE and HRF datasets.

Table 5.3 shows the reported results of the seventeen segmentation methods compared with the proposed method. From Table 5.3, it can be seen that the proposed bowler-hat transform outperforms several common or state-of-the-art methods from the field. In cases where the proposed method does not outperform, but still

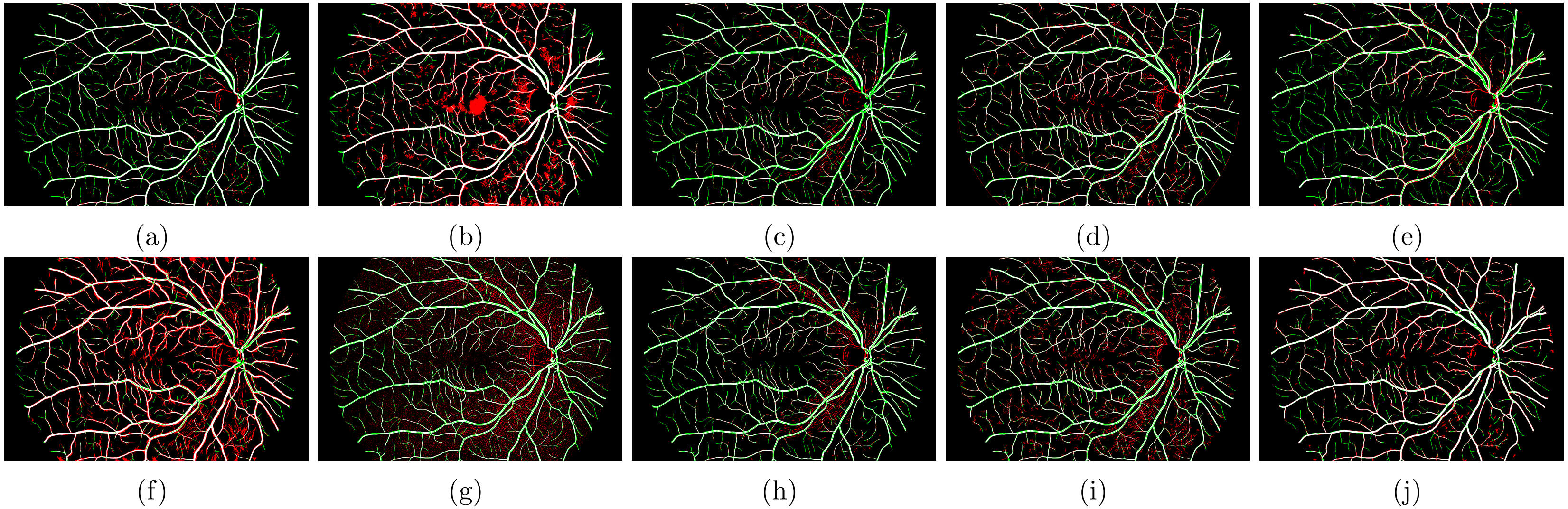

Figure 5.17: Curvilinear structures segmentation results obtained by the proposed and the state-of-the-art curvilinear structures enhancement methods followed by the same local thresholding approach proposed in [145] when applied to the HRF dataset images. (a) vesselness, (b) CLAHE, (c) Zana's top-hat, (d) neuriteness, (e) PCT-vesselness, (f) PCT-neuriteness, (g) wavelet, (h) line detector, (i) volume ratio, and (j) the bowler-hat. Colours indicate true positive (white), false positive (red) and false negative pixels (green). Corresponding mean AUC values can be found in Table 5.2.

Method	DRIVE			STARE			HRF		
	SN	SP	ACC	SN	SP	ACC	SN	SP	ACC
Staal et.al [41]	-	-	0.946	-	-	0.951	-	-	-
Soares et.al [146]	-	-	0.946	-	-	0.948	-	-	-
Lupascu et.al [147]	0.720	-	**0.959**	-	-	-	-	-	-
You et.al [148]	0.741	0.975	0.943	0.726	0.975	0.949	-	-	-
Marin et.al [149]	0.706	0.980	0.945	0.694	0.981	0.952	-	-	-
Wang et.al [68]	-	-	0.946	-	-	0.952	-	-	-
Mendonca et.al [116]	0.734	0.976	0.945	0.699	0.973	0.944	-	-	-
Palomera-Perez et.al [150]	0.660	0.961	0.922	**0.779**	0.940	0.924	-	-	-
Matinez-Perez et.al [151]	0.724	0.965	0.934	0.750	0.956	0.941	-	-	-
Al-Diri et.al [152]	0.728	0.955	-	0.752	0.968	-	-	-	-
Fraz et.al [89]	0.715	0.976	0.943	0.731	0.968	0.944	-	-	-
Nguyen et.al [84]	-	-	0.940	-	-	0.932	-	-	-
Bankhead et.al [11]	0.703	0.971	0.937	0.758	0.950	0.932	-	-	-
Orlando et.al [32]	**0.785**	0.967	-	-	-	-	-	-	-
Azzopardi et.al [153]	0.766	0.970	0.944	0.772	0.970	0.950	-	-	-
Odstrcilik et.al [3]	0.784	0.951	0.934	0.706	0.969	0.934	0.786	0.975	0.953
Zhang et.al [154]	0.774	0.972	0.947	0.779	0.975	0.955	0.797	0.971	0.955
Proposed method	0.718	**0.981**	**0.959**	0.730	**0.979**	**0.962**	**0.831**	**0.981**	**0.963**

Table 5.3: Performance of the state-of-the-art curvilinear structures segmentation methods and the proposed method, including mean sensitivity (SN), specificity (SP), accuracy (ACC), when applied to images in the DRIVE, STARE and HRF datasets. The best results are shown in bold.

performs to a similar quality, it is worth keeping in mind that many of these methods combine multiple stages, of which enhancement is just one, whereas our approach is able to achieve such high-quality results with just an enhancement process. The results on both datasets demonstrate that the sensitivity of the proposed method is not in the top three respectively for DRIVE ($SE = 0.616$) and STARE ($SE = 0.730$). However, the proposed method has the highest score with the specificity ($SP = 0.991$) for DRIVE and ($SP = 0.979$) for STARE. Most importantly, our method has the accuracy ($ACC = 0.960$) and ($ACC = 0.962$) for DRIVE and STARE respectively; the highest compared to other vessel segmentation methods. Finally, the proposed method has the highest score for HRF dataset, with ($SE = 0.831$), ($SP = 0.981$) and ($ACC = 0.963$).

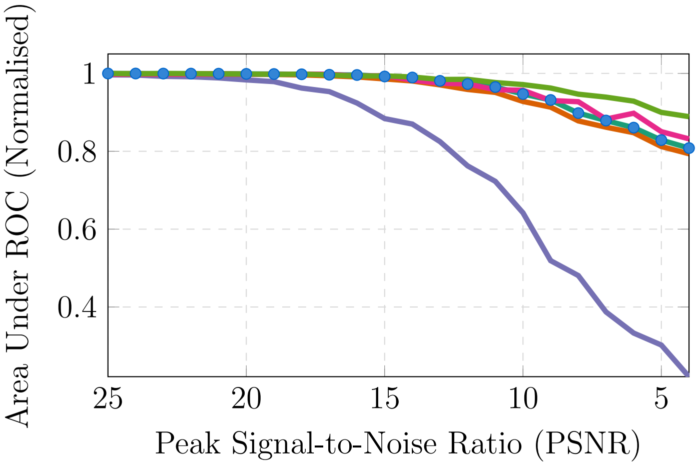

(a) Additive Gaussian Noise

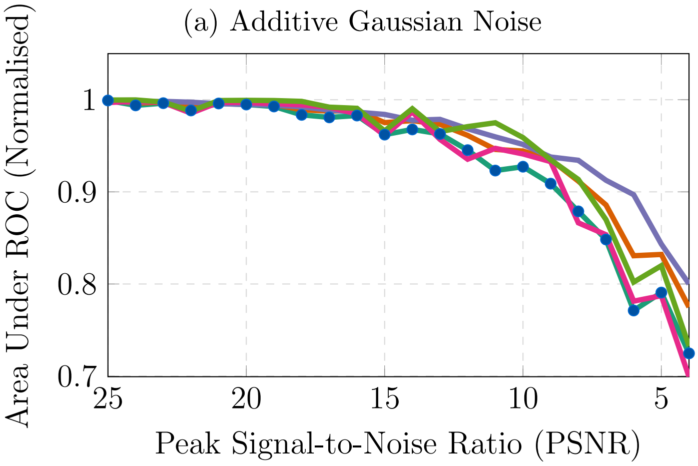

(b) Speckle Noise

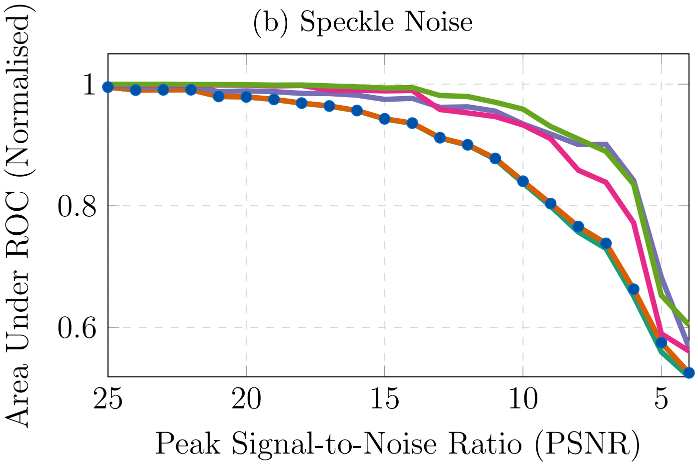

(c) Salt and Pepper Noise

Figure 5.18: The bowler-hat transform is robust against additive Gaussian noise but susceptible to speckle and salt&pepper. Mean AUC for the input image and the image enhanced by bowler-hat and by the state-of-the-art methods with different peak signal-to-noise ratios (PSNRs) for three different noise types: (a) additive Gaussian noise, (b) multiplicative Gaussian noise, and (c) salt and pepper noise (see legend for colours). (Note: Rest of the method results can be seen Figure 5.19).

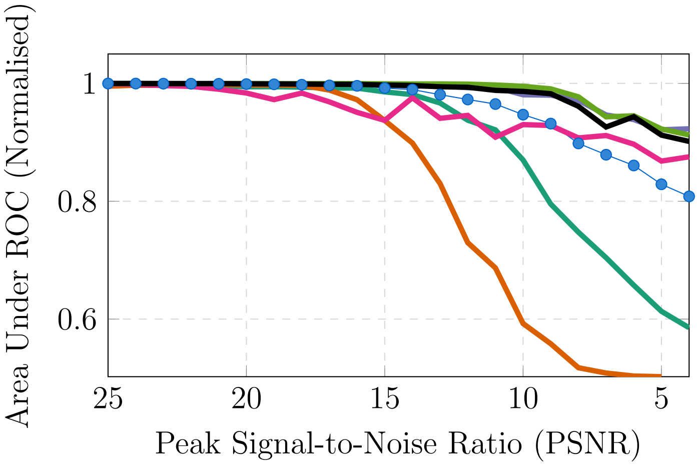

(a) Additive Gaussian Noise

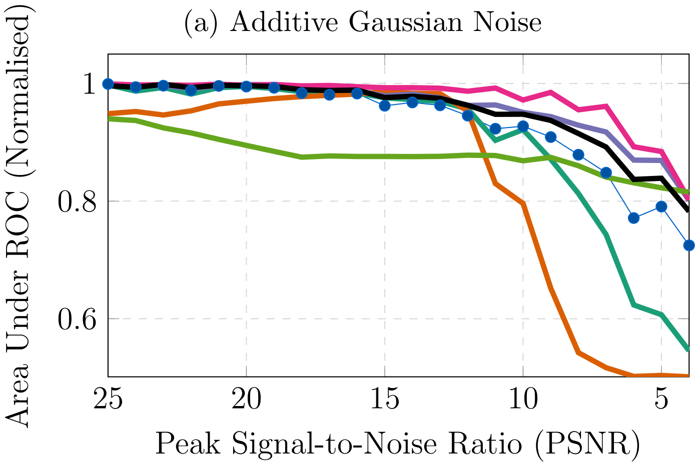

(b) Speckle Noise

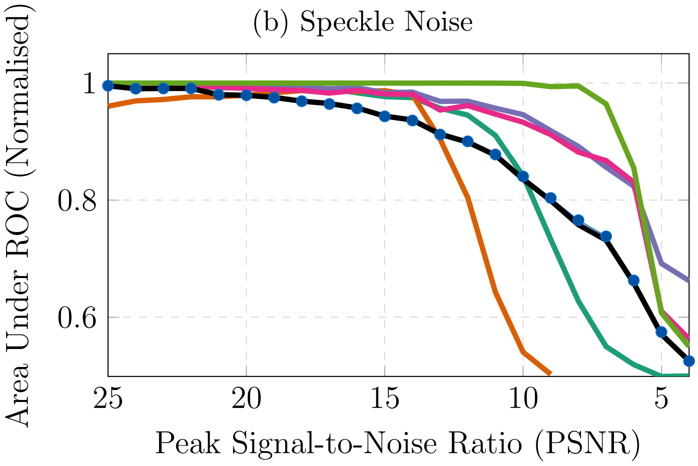

(c) Salt and Pepper Noise

Figure 5.19: The bowler-hat transform is robust against additive Gaussian noise but susceptible to speckle and salt&pepper. Mean AUC for the input image and the image enhanced by bowler-hat and by the state-of-the-art methods with different peak signal-to-noise ratios (PSNRs) for three different noise types: (a) additive Gaussian noise, (b) multiplicative Gaussian noise, and (c) salt and pepper noise (see legend for colours).

5.3.5 Response to Noise

To test how the state-of-the-art enhancement methods and the proposed method behave with a different level and type of noise, a noisy synthetic image that includes a single curvilinear structure was used. I generated such noisy image by optimising the noise generation parameters to achieve a target PSNR by using a genetic optimisation algorithm proposed in [155]. Then examine the enhancement methods by increasing the noise level and then calculating the AUC values for each level of noise and each comparator method. Figure 5.18 shows the effect of three different noise types on the proposed and state-of-the-art methods. Given that the proposed method has no built-in noise suppression, it is unsurprising that the effect of noise on the enhanced image is in-line with the raw image. It is been noted that the method is weakest in response to speckle noise (multiplicative Gaussian) and also weak in response to salt and pepper noise. This follows from the noise-sensitivity in morphological operations and should be taken into consideration when choosing an enhancement method.

5.3.6 Other Biomedical Data

While I have demonstrated the proposed method on the enhancement of curvilinear structures, the approach is applicable to a wide range of biomedical images of different types of curvilinear structures, see Figure 5.20.

5.4 Conclusion and Discussion

An wide range of image processing methods have been proposed for curvilinear structure enhancement in biomedical images. Most of them, however, suffer from issues with low-contrast signals, enhancement of noise or when dealing with junctions.

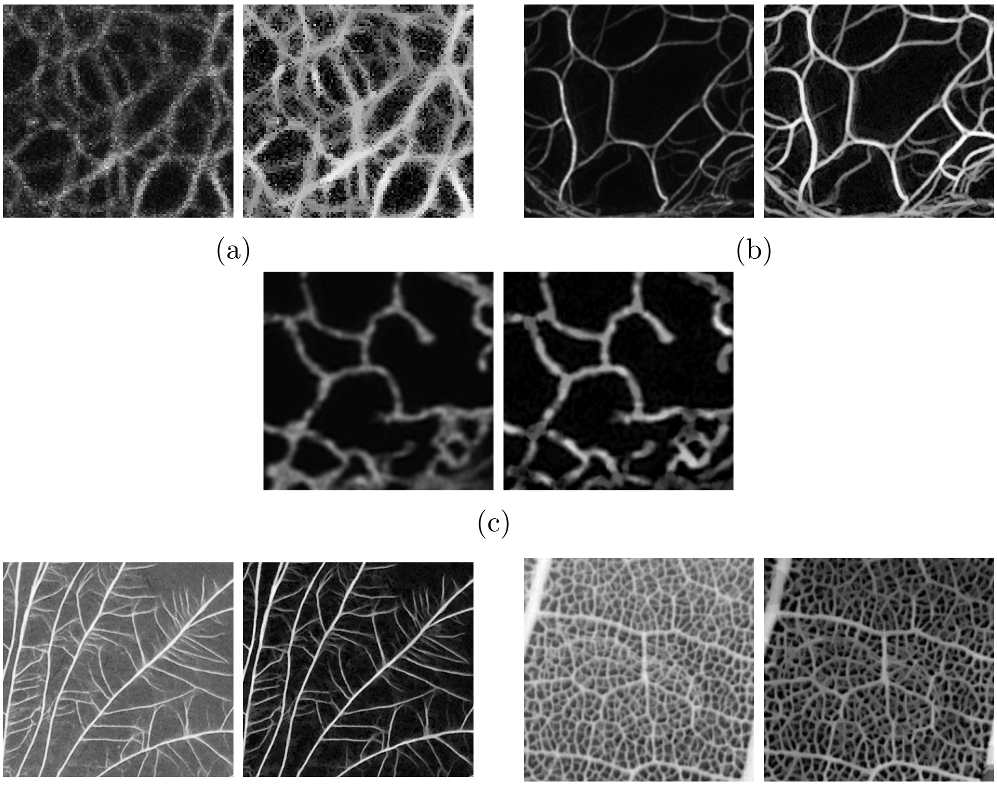

(a) (b) (c) (d) (e)

Figure 5.20: Results of the curvilinear structure enhancement using the bowler-hat on biological images of (a-b) cytoskeletal networks, (c) endoplasmic reticulum, and (d-e) macro-scale networks. (a) provided by Prof. Dr. Med. Rudolf Leube, RWTH Aachen University, Germany. (b) provided by Dr. Tim Hawkins, Durham University, UK. (c-e) provided by Prof. M. Fricker, Oxford University, UK. The proposed method can enhance the curvilinear structure in the wide range of biomedical images. Notice that, the proposed method is able to enhance line-like structures in the different type of biological images.

In this Chapter, I introduce an enhancement method for curvilinear structures based on mathematical morphology, which exploits the elongated shape of curvilinear structures. The proposed method, the bowler-hat transform, was qualitatively and quantitatively validated and compared with the state-of-the-art methods using a range of synthetic and real image datasets, including retinal image collections (DRIVE, STARE and HRF). I showed the effectiveness of the bowler-hat transform, and its superior performance on retinal imaging data, see Figure 5.14, Table 5.1, and Table 5.2. Furthermore, experimental results on the unhealthy retinal images have shown that the curvilinear structures enhanced by our bowler hat transform are continuous and complete in problematic regions as illustrated in Figure 5.16.

As with any image processing technique, our proposed method has limitations. Basically, morphological operations are renowned for their large computational requirements. Another limitation of the proposed method is displayed in Figure 5.8 row 4, which shows a curvilinear structure with an attached 'blob' (green arrow), a perfect curvilinear structure enhancement method would enhance all of the linear structure and none of the blob. Whilst none of the comparison methods act in this ideal manner many of them show a clear difference between the blob response and curvilinear structures response, our proposed method shows some difference, but this difference impacts the signal of the curvilinear structure.

Moreover, as I note in Figure 5.9, the proposed method is sensitive to noise such as susceptible to speckle and salt&pepper, as is the PCT-neuriteness method in Figure 5.9g. In the future, I will investigate introducing a line-shaped morphological structuring element with varying thickness to address this issue. Nevertheless, our implementation demonstrates an improved and easy to use curvilinear structure enhancement alternative that can be used in a wide range of biomedical imaging scenarios [156]. Whilst one would expect the lack of noise suppression to be a major issue with regard to quantified measurements of curvilinear structure enhancement, I find that the proposed method gives the best enhancement of all methods on the DRIVE, STARE and HRF datasets (see Table 5.1 and Figure 5.14).

In this Chapter, I have demonstrated the ability of the proposed bowler-hat transform to effectively enhance and segment curvilinear structures in the retinal images. In addition, to illustrate the robustness of the proposed bowler-hat transform enhance, I have matched it with the seventeen state-of-the-art methods previously tested on the DRIVE, STARE and HRF image datasets, see Table 5.3.

Epilogue

In this Chapter, I have introduced a new bowler-hat transform approach, based on mathematical morphology, for curvilinear features enhancement in biomedical images. The proposed approach has been extensively validated and compared to other several state-of-the-art curvilinear features enhancement methods using a variety of synthetic and real biomedical images.

In the next Chapter, I will present a 3D extension of the bowler-hat transform.

Chapter 6

The Multiscale Bowler-Hat Transform for Curvilinear Features Enhancement in 3D Biomedical Images

Prologue

Enhancement and detection of 3D curvilinear structures in 3D biomedical images has long been an open problem as most existing image processing methods fail in many aspects, including a lack of uniform enhancement between curvilinear structures of different radii and a lack of enhancement at the junctions. In this Chapter, I propose a new method based on mathematical morphology to enhance 3D curvilinear structures in biomedical images. Chapter 3 (*p.* 31) is also a key to understand proposed method in this Chapter. This method is an extension of 2D bowler-hat transform, explained in Chapter 5 (*p.* 55). The proposed method, 3D bowler-hat transform, combines sphere and line structuring elements to enhance curvilinear structures. The proposed method is validated on synthetic and real data, and compared with state-of-the-art methods. Our results show that the proposed method achieves a high-quality curvilinear structures enhancement in both synthetic and real biomedical images, and is able to cope with variations in curvilinear structures thickness throughout vascular networks while remaining robust at junctions.

Declaration: This Chapter is based on the following publication: Sazak, Ç., Nelson, C. J. & Obara, B. *The multiscale bowler-hat transform for curvilinear structure enhancement in 3D biomedical images* in *British Machine Vision Conference* (2018). This Chapter is presented as published, although referencing and notation has been altered and cross-referencing added for consistency throughout this thesis. Some stylistic changes have been made for consistency. The majority of the text is verbatim; however, additions to the body of text are included where they are appropriate.

6.1 Introduction

Automatic detection of curvilinear structures is one of the fundamental procedures in many 3D biomedical image processing applications, where they are used to understanding of important vascular networks, such as cytoskeletal networks, blood vessels, airways, and other similar fibrous tissues. Reliable detection and then accurate analysis of these vascular networks strongly relies on robust curvilinear structures enhancement methods. Several such methods have been proposed and investigated for various types of biomedical images such as: blood vessels [4, 49], neurons [76], microtubules [127] and others [40, 157]. Nevertheless, most of the curvilinear structures enhancement methods still suffer from unresolved problems such as losing signals at the junctions or false vessel effects [17].

In this Chapter, I extended 2D curvilinear structures enhancement method, called the 2D bowler-hat transform [17], to 3D. The proposed method is based on a 2D image filtering method exploring a concept of mathematical morphology [18]. I qualitatively and quantitatively validate and compare the proposed 3D method with the state-of-the-art curvilinear features enhancement methods using a range of synthetic and real biomedical images. Our results show that the proposed method produces a high-quality curvilinear structure enhancement, especially at junctions in both synthetic and real images. The method is suitable to be applied to a variety of biomedical image types without requiring prior preparation or tuning. Finally, I made my method available online, along with source code and all test functions. The source code is available in a GitHub repository https://github.com/CigdemSazak/bowler-hat-3d.

6.2 Method

In this Section, I introduce a 3D extension of a mathematical morphology-based 2D method for curvilinear structure enhancement, called the bowler-hat transform [18]. While explaining the details of the proposed method, we point out the concepts that allow us to address the major drawbacks of existing, state-of-the-art curvilinear structures enhancement methods.

6.2.1 Mathematical Morphology

Mathematical morphology concept has been extensively used in image processing and image analysis, see Chapter 3 (*p.* 31). A wide range of applications and a background information see Chapter 2 (*p.* 8), and Chapter 5 (*p.* 55) for a use of the concept to define our 2D bowler-hat transform [18].

6.2.2 Proposed Method

The proposed method is explained and summarized with a small example in 6.1. The 3D bowler-hat transform combines two banks of different structuring elements: a bank of spherical structuring elements with varying diameter and a bank of orientated line structuring elements with varying length and directions.

(a) Input Image

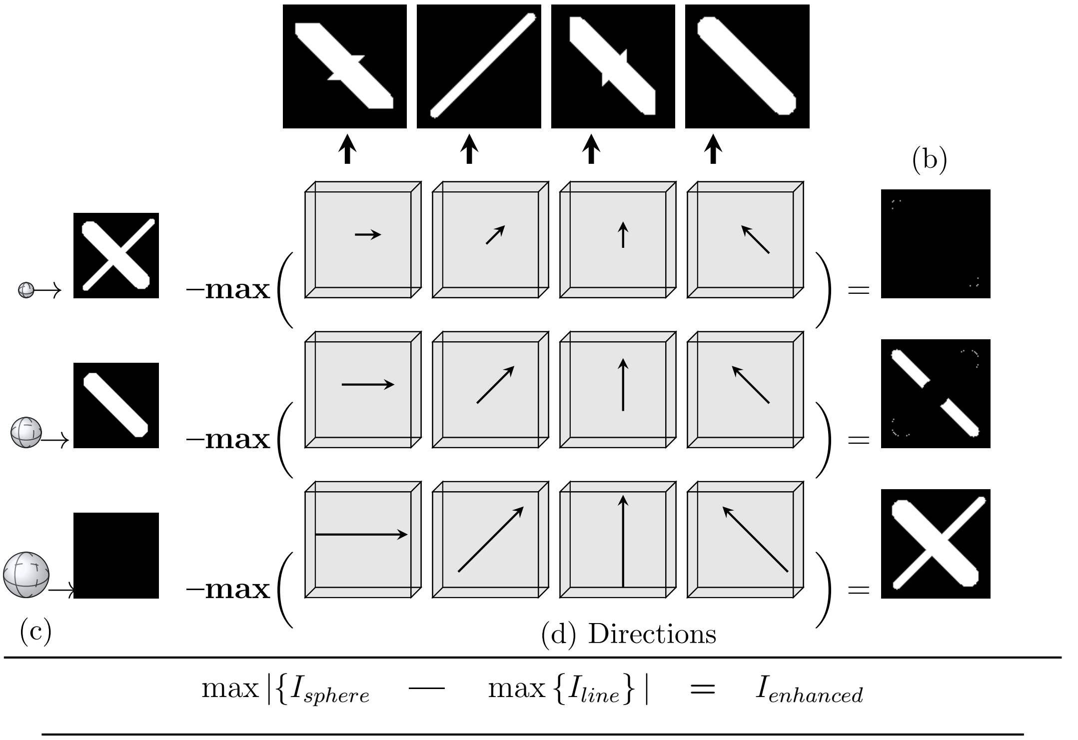

Figure 6.1: A step-by-step schematic explanation of how the proposed method works on a simple image. Suppose that (a) is an input image. (c) illustrates openings with 'sphere' structure elements. (d) demonstrates openings with 'line' elements of different directions and same lengths as equivalent 'sphere' element diameters; the pixel-wise maximum of these openings is taken. (b) This result is then subtracted from the sphere openings.

First, I create a bank of morphological openings of a 3D input image I with spherical structuring elements S^d_{sphere} of diameter $d \in [1, d_{max}]$, where d_{max} is expected maximum size of curvilinear structures in a given image I. After every morphological opening of the image I, curvilinear structures smaller than d are eliminated and the ones larger than d remain.

As a result, a 3D image stack, for all $d \in [1, d_{max}]$, is constructed as;

$$\{I_{sphere}\} = \{I \circ S^d_{sphere}\}, \quad \forall d \in [1, d_{max}]. \tag{6.1}$$

Then, another bank of morphological openings of the input image I is performed with line structuring elements $S_{line}^{d,\mathbf{v}}$ of lengths d, $\forall d \in [1, d_{max}]$, and of directions defined as follows;

$$\mathbf{v} = (\theta_k, \phi_k), \quad \forall k \in [1, N]. \tag{6.2}$$

Direction (θ_k, ϕ_k) is defined as a k^{th} point from N uniformly distributed points on the unit sphere, and more details can be found in [131]. After every morphological opening of the image I with a line structuring element $S_{line}^{d,\mathbf{v}}$, curvilinear structures smaller than d along direction $\mathbf{v}$ are eliminated but all curvilinear structures that are longer than d along direction $\mathbf{v}$ remain. This step results in a 3D image stack for all lengths d and all directions $\mathbf{v}$;

$$\{I_{line}\} = \{I \circ S_{line}^{d,\mathbf{v}}\}, \forall d \in [1, d_{max}], \forall k \in [1, N]. \tag{6.3}$$

Then, for each length d, a pixel-wise maximum across all directions $\mathbf{v}$ is calculated resulting in a 3D image stack;

$$\{I_{line}\} = \{\max_{k \in [1,N]} |\{I \circ S_{line}^{d,\mathbf{v}}\}|\}, \quad \forall r \in [1, d_{max}]. \tag{6.4}$$

The enhanced image is then produced by taking maximum stack-wise difference at each pixel;

$$I_{enhanced} = \max_{r \in [1, d_{max}]} |\{I_{sphere} - I_{line}\}|. \tag{6.5}$$

With the 3D bowler-hat transform, areas that are dark (background) in the original image remain dark due to the use of openings; blob-like bright objects (undesired foreground features) are suppressed as the sphere-based and line-based opening gives similar values; and tube-like bright objects (desired foreground features) are enhanced due to the large difference between sphere-based and longer line-based openings. To assign an appropriate d_{max}, expected maximum curvilinear structures size in the image, allows the identification of most of the curvilinear structures and junctions, something that many other curvilinear structure enhancement methods fail to do. This is due to the ability to fit longer line-based structuring elements within the junction area. In general, I have found the bowler-hat transform to be robust with N=[32,64] orientations of the line structuring element. In Section 6.3 I illustrate the key advantages of the proposed method over other curvilinear structure enhancement methods.

6.3 Results and Discussions

In this Section, I qualitatively and quantitatively validate the robustness of the proposed method using a range of synthetic and real biomedical image datasets. We then compare the proposed method with the state-of-the-art curvilinear structure enhancement methods such as Hessian-based vesselness [4], neuriteness [8] and volume ratio [9], PCT-based vesselness and neuriteness [17], and recently published RORPO [95].

6.3.1 Quantitative Validation

While a visual examination can give some subjective information regarding the effectiveness of the curvilinear structure enhancement method, a form a quantitative validation is also required. To compare the proposed method with the other state-of-the-art algorithms, I have chosen to calculate the Receiver Operating Characteristic (ROC) curve and the Area Under the Curve (AUC) and more details can be found in [158].

6.3.2 Response to Noise

Figure 6.2 presents the performance comparison of the proposed method with the state-of-the-art approaches under the influence of three different noises: additive Gaussian, speckle and salt & pepper. Figure 6.3 demonstrates a sample of images in

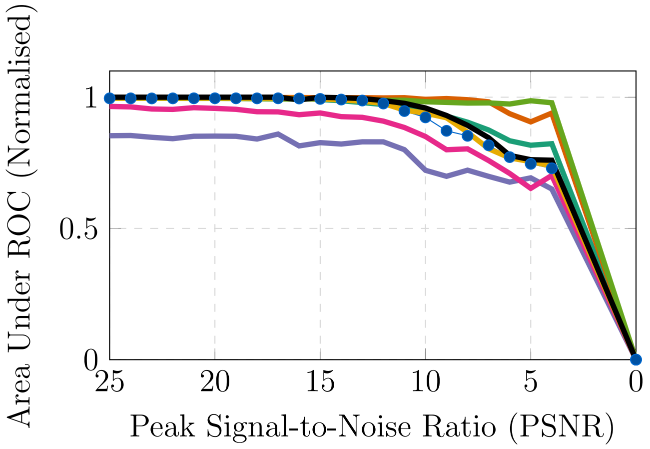

(a) Additive Gaussian Noise

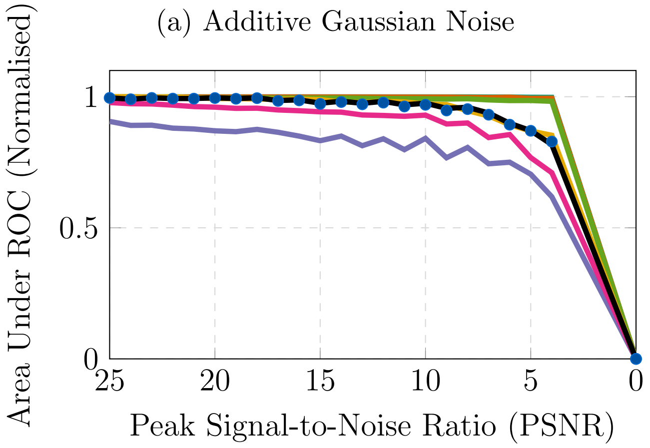

(b) Speckle Noise

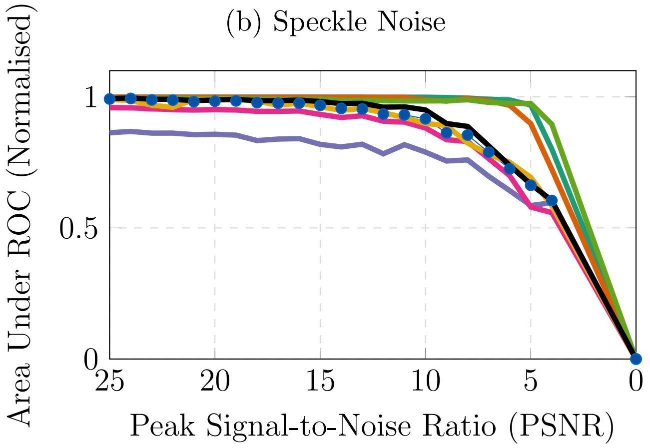

(c) Salt and Pepper Noise

Figure 6.2: AUC values for the input image and the image enhanced by the proposed method and the state-of-the-art methods with different peak signal-to-noise ratios (PSNRs) for three different noise types: (a) additive Gaussian noise, (b) multiplicative Gaussian (speckle) noise, and (c) salt and pepper noise (see legend for colours). Sample images used here can be seen in Figure 6.3.

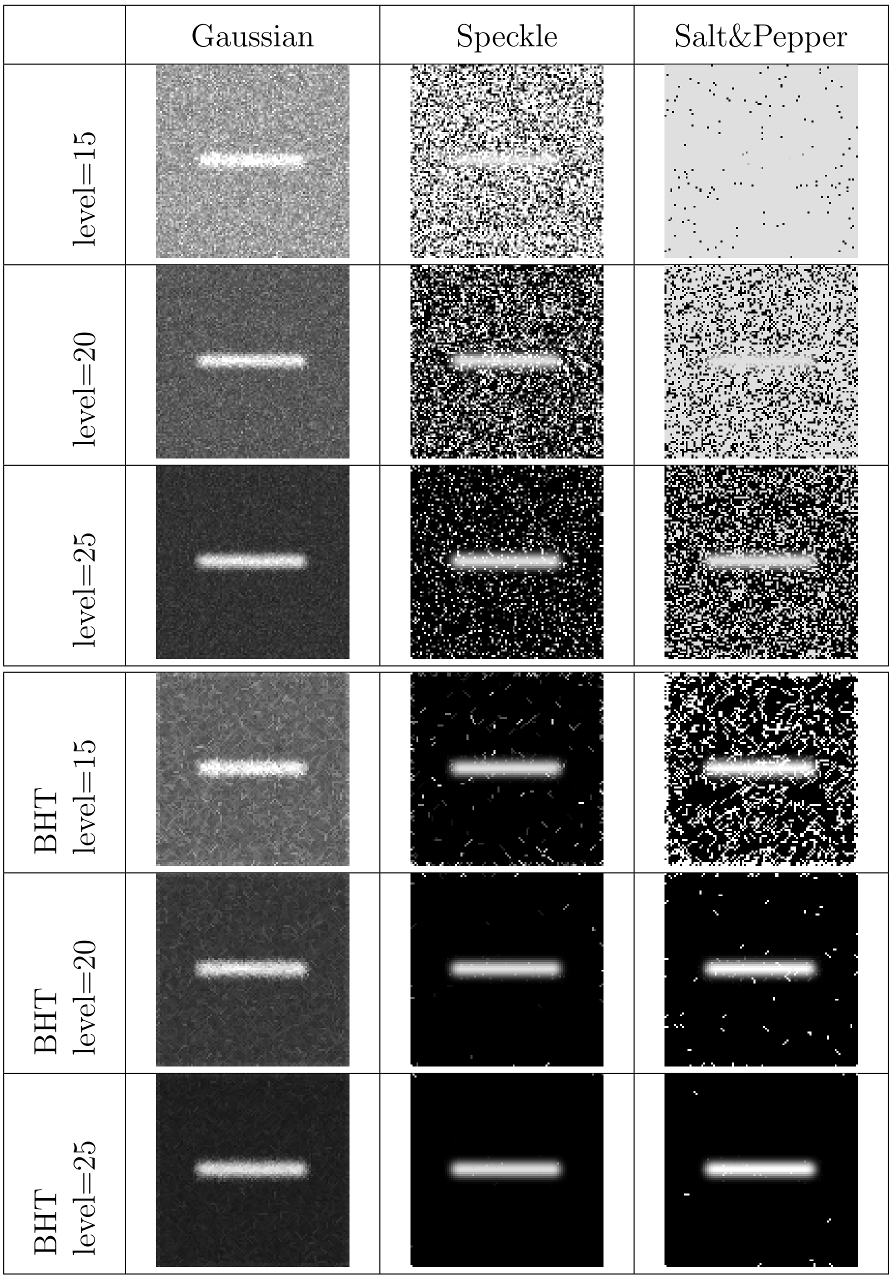

Figure 6.3: Robustness of 3D bowler-hat transform-based curvilinear structures enhancement approach against the noise. Rows 1-3: 3D sample images of line-like structure with different types (additive Gaussian noise, multiplicative Gaussian (speckle) noise, and salt and pepper noise) and levels (15, 20, 25) of noise. Rows 4-6: the input images enhanced by the 3D bowler-hat transform-based curvilinear structures enhancement approach (BHT). All 3D images are illustrated as a 2D maximum intensity projection.

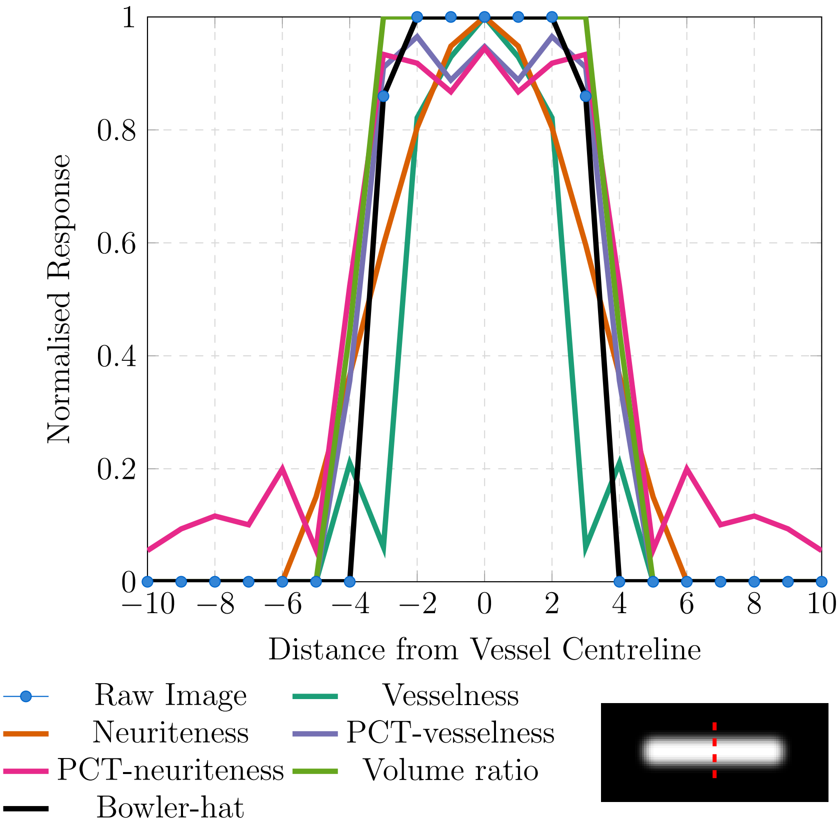

Figure 6.4: Cross-sectional profile of 2D max intensity projection of 3D synthetic vessel image (black, dashed line), curvilinear structure enhanced by the proposed method (black, solid line) and by the state-of-the-art methods (see legend for colours). All images are normalised such that the brightest pixel in the whole image has a value of 1 and the darkest a value of 0. Some of the methods shrink the curvilinear structures like vesselness and create some shadows or blur around the vessel corners like PCT-neuriteness, however, when you look at the proposed method, it exactly follows the structure of the input images (since proposed method overlap the raw image lines).

the different type of noise and with different level of noise. Evidently, the proposed method has no built-in noise suppression; as expected that the effect of noise on the enhanced image is in-line with the raw image. This inherits from the noise-sensitivity in mathematical morphology and should be taken into consideration while choosing an enhancement method. However, Figure 6.3 illustrates the sample images for the different type of noise and different level on a line-like structure. These sample images also demonstrate the data used in Figure 6.3.

6.3.3 Profile Analysis

Figure 6.4 illustrates bowler-hat and state-of-the-art methods responses to a simple curvilinear structure on a synthetic image. It is obvious that the value of the enhanced image at the middle of the curvilinear structure reaches a peak value and quickly drops off and decreases at the expected thickness of the curvilinear structure by the Hessian-based methods. On the other hand, the PCT-based methods are less responsive to the centreline of the curvilinear structure, while obtaining a high response to the edges due to the contrast variations. The value of the enhanced image does not significantly peak at the curvilinear structure centre, but their response does not drop off quickly since it is free from the contrast variations. The proposed method has both these benefits: a maximal peak value at the curvilinear structure centre-line and an enhanced response to the edges of the curvilinear structure. As a result, reliable curvilinear structure thicknesses can be captured.

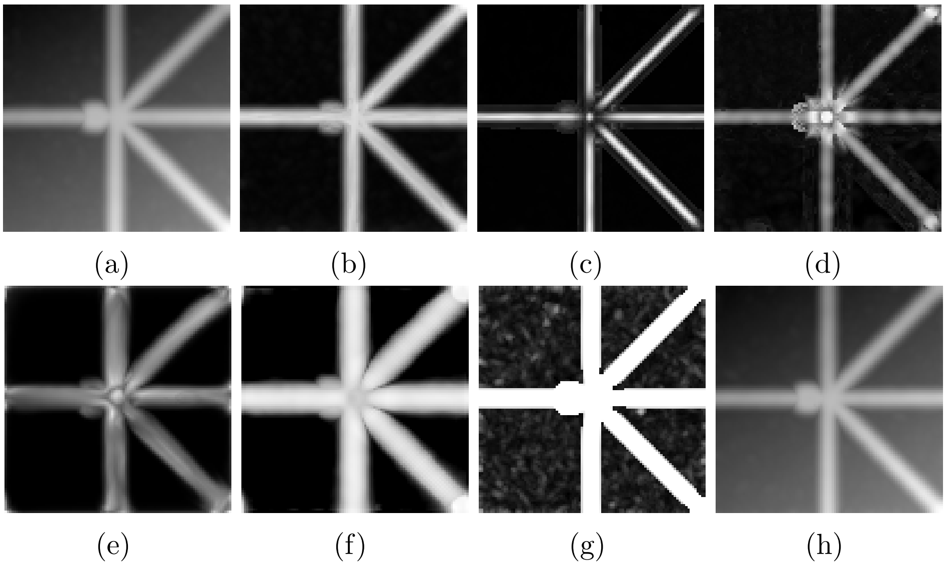

Figure 6.5: Comparison of the curvilinear features enhancement methods' abilities to deal with uneven background illumination. (a) An input image. (b) Bowler-hat enhancement response. (c-h) state-of-the-art methods' enhancement responses, respectively: (c) vesselness, (d) neuriteness, (e) PCT-vesselness, (f) PCT-neuriteness, (g) volume ratio, and (h) RORPO. The perfect enhancer method should detect only curvilinear structure. However, most of the methods fails at the vessel junctions like (c, d) and still enhance the blob-like structures as in (h, g).

6.3.4 Response to Uneven Background Illumination

Figure 6.5 presents an intuitive comparison between the proposed method and other state-of-the-art methods, regarding the response to the uneven background illumination. When compared with the other methods, the proposed method maintains the high responses at the junctions and seems unaffected by uneven background

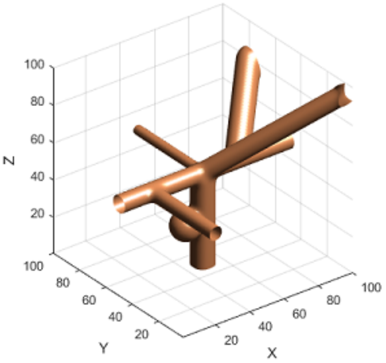

(a) Input image

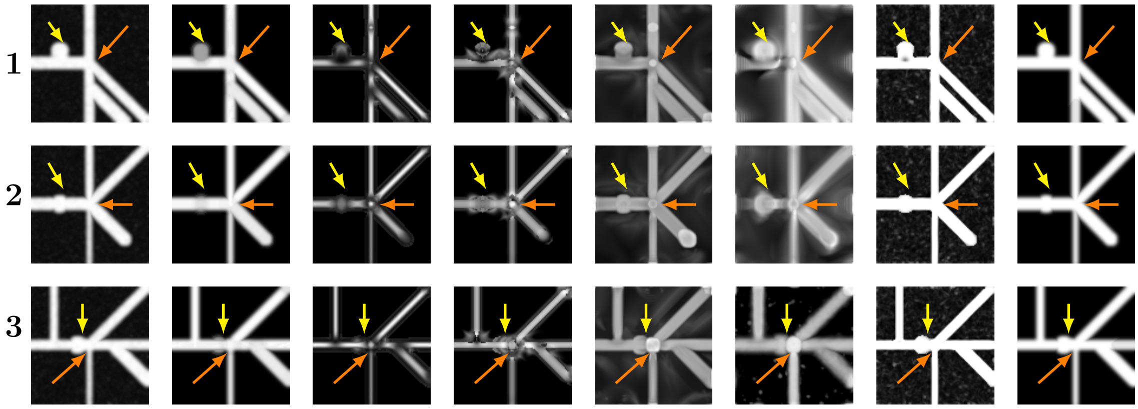

(b) (c) (d) (e) (f) (g) (h) (i)

Figure 6.6: Comparison of curvilinear structure enhancement methods' responses to curvilinear structures, intersections/junctions, and blobs. A 3D synthetic image (a) by 100x100x100 voxels is generated and three angles 2D max intensity projection is used (b); respectively 1st row is X, the 2nd row is Y and the 3rd row is Z direction. All curvilinear structures have nine pixels thickness and blob has a diameter of 21 pixels. (c) shows the bowler-hat and the state-of-the-art methods respectively, (d) vesselness, (e) neuriteness, (f) PCT-vesselness, (g) PCT-neuriteness, (h) volume ratio, and (i) RORPO. The arrows refer features of interest: blob-like structures (yellow arrows), junctions (orange arrows), noise (green arrows).

illuminations.

6.3.5 Response to Curvilinear Structures, Intersections/Junctions, and Blobs

Figure 6.6 illustrates the comparison between the proposed method and state-of-the-art methods. It is obvious that most of the state-of-the-art methods fail at the junction like in Figure 6.6d and some of those create false curvilinear structures effects as in Figure 6.6g or add noise the enhanced image Figure 6.6h. Compare to others, our proposed method is free from all of these effects and artefacts, but it is not good at suppressing the blob-like structures as like vesselness or neuriteness.

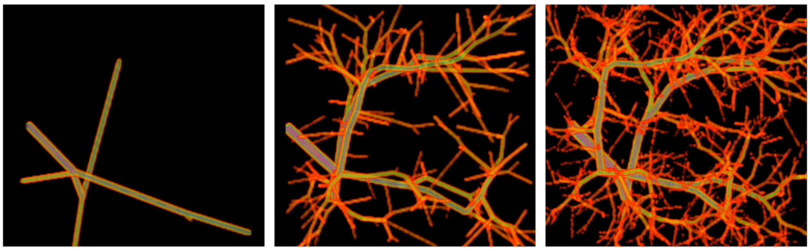

(a) 5 (b) 200 (c) 1000

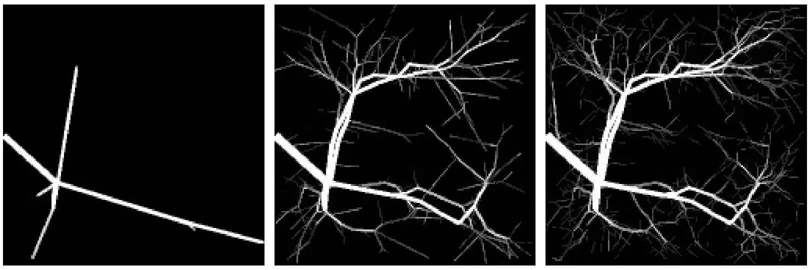

(d) 5 (e) 200 (f) 1000

Figure 6.7: Visualisation of 3D synthetic curvilinear networks images generated with the VascuSynth software [159]. The images (a-c) (167x167x167 voxels) are used to quantitatively validate the proposed method and the state-of-the-art methods and (d-f) are the results of the proposed method. The proposed method is able to detect most of the branches and more detailed results are shown in Figure 6.8 and in Table 6.1.

6.3.6 Response to Vascular Network Complexity

Nine volumetric images and their corresponding ground truth images of 3D synthetic vascular networks with an increasing complexity were generated using the VascuSynth software [159], as shown in Figure 6.7. In addition, to make the image more realistic, I add a small amount of the Gaussian noise of level $\sigma_2 = 10$ and apply a Gaussian smoothing kernel with a standard deviation of 1. I tested the proposed methods as well as the aforementioned other approaches on these images. The results are presented in Table 6.1. Figure 6.8 also demonstrates the ROC curve all over the nine enhanced images. It appears that the proposed method clearly has the highest AUC value (0.965) compare to the state-of-the-art methods. Overall, the proposed method performance is better than state-of-the-art methods. However, the average computation time for the proposed method for VascuSynth image is 328 seconds.

	AUC					
Nodes	Vesselness	Neuriteness	PCT-ves.	PCT-neu.	Volume ratio	**Bowler-hat**
5	**0.999**	0.923	0.840	0.897	**0.999**	**0.999**
10	0.996	0.883	0.820	0.873	0.998	**0.999**
50	0.976	0.830	0.794	0.851	0.981	**0.994**
100	0.951	0.778	0.778	0.827	0.957	**0.982**
200	0.930	0.755	0.770	0.799	0.936	**0.966**
400	0.910	0.746	0.749	0.788	0.917	**0.950**
600	0.902	0.743	0.742	0.777	0.909	**0.941**
800	0.885	0.719	0.724	0.756	0.893	**0.926**
1000	0.884	0.722	0.726	0.759	0.891	**0.924**
mean(std)	0.937(0.045)	0.788(0.073)	0.771(0.04)	0.814(0.05)	0.942(0.043)	**0.965(0.03)**

Table 6.1: AUC values for nine 3D images of vascular networks with increasing network's complexity (see Figure 6.7) enhanced with the proposed and the state-of-the-art methods. The best results for each vascular network are in bold. ROC curve of the all volumetric images can be seen in Figure 6.8.

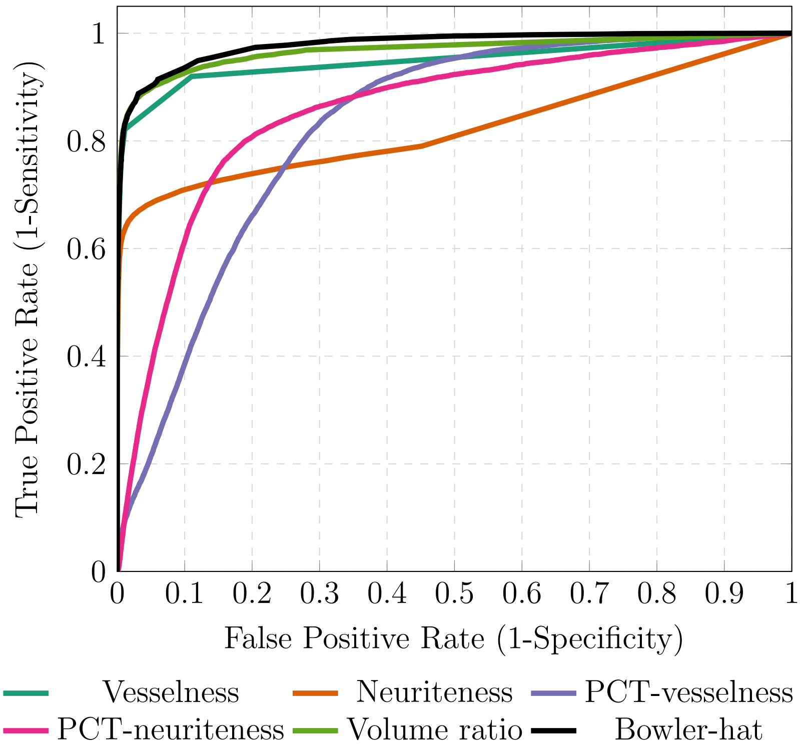

Figure 6.8: Mean ROC curve for all vascular networks images from Figure 6.7 calculated using the proposed and the state-of-the-art methods (see legend for colours). Individual AUC values can be found in Table 6.1.

6.3.7 Real Data

An Olfactory Projection Fibers image dataset from DIADEM Challenge [160] is used to demonstrate the robustness of the proposed method against the noise. In two exemplary fibers images, Gaussian noise was introduced at the noise levels ranging from $\sigma = 10$ to $\sigma = 60$, and salt and pepper noise at the different level of density $\rho = 10$ to $\rho = 60$ see Figure 6.9. Such images were then enhanced with the proposed method and the AUC values were calculated and presented in Figure 6.9. I also tested the performance of the proposed method on the 3D real images. Here I adopt three representative types of real images, namely microtubules network in a plant cell, keratin network in a skin cell, and neuronal network. Correspondingly I compare the output of the proposed method with five other approaches, and the results are shown in Figure 6.10. It is clearly suggested that our method has the

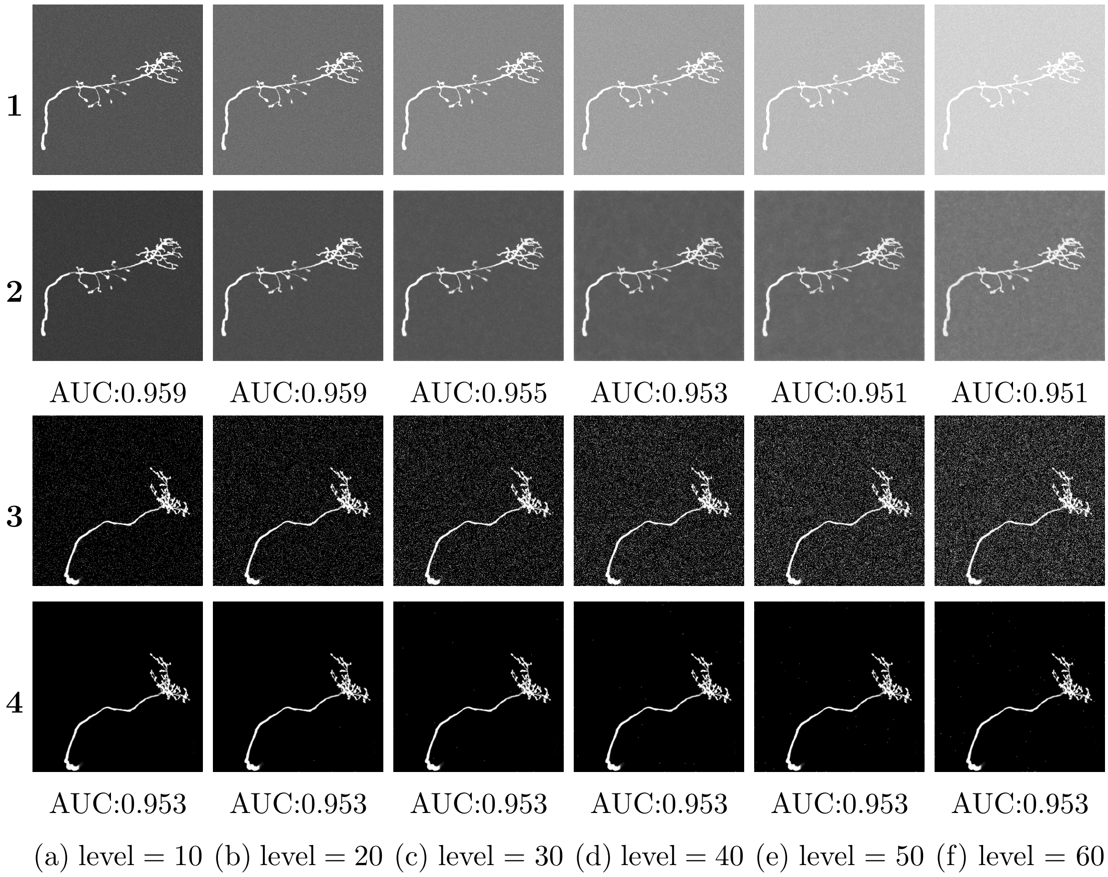

(a) level = 10 (b) level = 20 (c) level = 30 (d) level = 40 (e) level = 50 (f) level = 60

Figure 6.9: Application of the proposed method into the Olfactory Projection Neuron dataset from the DIADEM Challenge. All of the images are 2D maximum intensity projection. Rows 1 and 3 are input images that have been contaminated by different levels (increasing left to right) and types of noise (1 - Gaussian additive noise; 3 - salt and pepper noise). Rows 2 and 4 are enhancement results with the proposed method and corresponding AUC values.

best performance in preserving junctions.

6.4 Conclusion

Hessian- or Phase Congruency Tensor-based image enhancement methods had been commonly used to enhance curvilinear structures in 3D biomedical images using measurements like vesselness, neuriteness and volume ratio.

This Chapter proposes a novel mathematical morphology-based method for curvilinear structures enhancement in 3D biomedical images. The proposed method

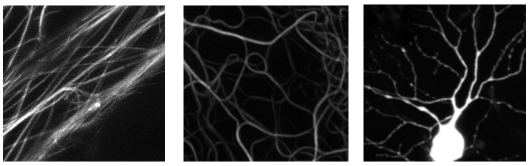

(a) ROIs

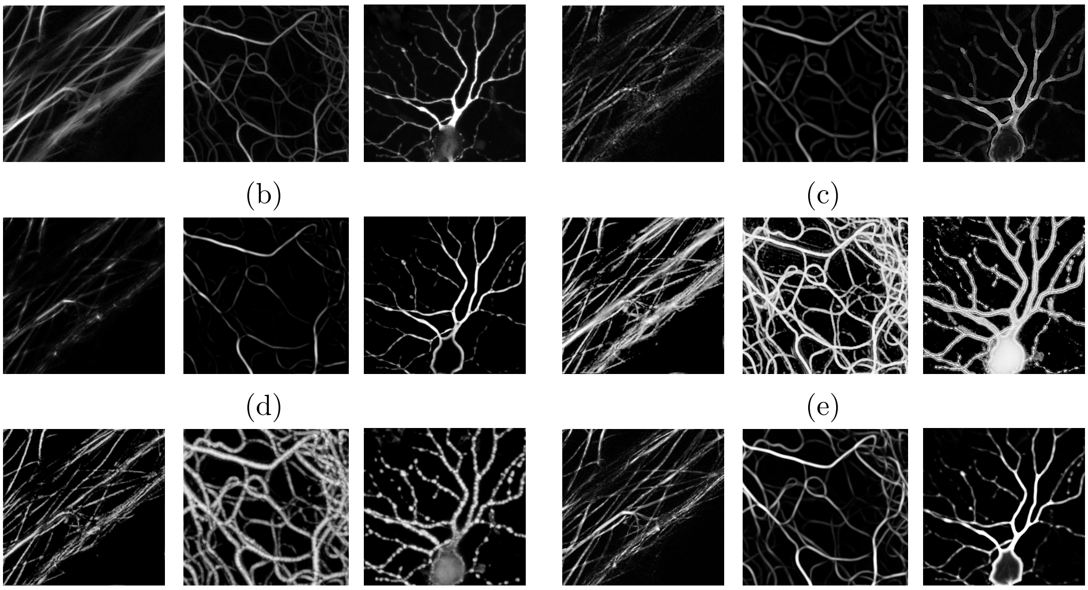

(b)

(c)

(d)

(e)

(f)

(g)

Figure 6.10: Comparison of the proposed and the state-of-the-art methods on a set of real biomedical images. (a) are regions of interest highlighted in red in Chapter 4 (*p.* 41) in Figure 4.3. Results: bowler-hat (b), neuriteness (c), vesselness (d), PCT-neuriteness (e), PCT-vesselness (f) and volume ratio (g). Notice that, (b) enhances curvilinear structures while ignoring the blob-like structures. Even if (e) enhance and make the curvilinear structures more visible, it also enhance the blob-like structures.

is shown to have benefits over existing methods, including no loss of signal and junctions and minimized artefacts at curvilinear structure ends. I show robustness on both synthetic and real image datasets. In order to the robustness of the proposed method, a fast noise-robust version of the line segment opening/closing based on the rank-max opening maybe be considered [161].

Epilogue

In this Chapter, I have introduced a 3D extension of 2D bowler-hat transform-based approach for curvilinear structure enhancement method in 3D biomedical images. The proposed approach has been extensively validated and compared to a range of state-of-the-art methods using a variety of synthetic and real biomedical images.

In the remaining Chapter, I am going to present another curvilinear features enhancement method called multiscale top-hat tensor.

Chapter 7

Curvilinear Structure Enhancement by Multiscale Top-Hat Tensor in 2D/3D Images

Prologue

A wide range of biomedical applications require enhancement, detection, quantification and modelling of curvilinear structures in 2D and 3D images. Curvilinear structure enhancement is a crucial step for further analysis, but many of the enhancement approaches still suffer from contrast variations and noise. This can be addressed using a multiscale approach that produces a better quality enhancement for low contrast and noisy images compared with a single-scale approach in a wide range of biomedical images. In this Chapter I propose the Multiscale Top-Hat Tensor (MTHT) approach, which combines multiscale morphological filtering with a local tensor representation of curvilinear structures in 2D and 3D images. From this tensor representation, I extract the eigenvalues and compute MTHT-based analogues to the commonly used curvilinear measures, such as vesselness and neuriteness.

Declaration: Alharbi, S. S., Sazak, C., Nelson, C. J. & Obara, B. *Curvilinear*

Structure Enhancement by Multiscale Top-Hat Tensor in 2D/3D Images in IEEE International Conference on Bioinformatics and Biomedicine (BIBM) (Madrid, Spain, Dec. 2018).

Çiğdem Sazak and Shuaa S. Alharbi contributed equally to this work. This Chapter is presented as published in the International Conference on Bioinformatics and Biomedicine, 2018 although referencing and notation has been altered and cross-referencing added for consistency throughout this thesis. Some stylistic changes have been made for consistency. The majority of the text is verbatim; however, additions to the body of text are included where they are appropriate.

7.1 Introduction

The enhancement and detection of curvilinear structures are important and essential tasks in biomedical image processing. There is a wide range of curvilinear structure in biomedical imaging data, such as blood vessels, neurons, leaf veins, and fungal networks. Curvilinear structure enhancement is an important step, especially where the subjective quality of images of curvilinear structures is necessary for human interpretation.

A wide range of curvilinear structure enhancement approaches has used mathematical morphology operations to enhance curvilinear structures in 2D and 3D images. The top-hat transform [102] is a popular approach, which extracts bright features from a dark background that match the shape and orientation of a specified structuring element [15]. This approach has been used to extract curvilinear structures in retinal [53] and fingerprint [36] images.

A local tensor representation [16] of an image measures how image structures change across dominant directions, and the eigenvalues and eigenvectors of the tensor can provide information that can be used to enhance, extract and analyse curvilinear structures.

In this Chapter, I combine these two approaches by representing curvilinear structures filtered by morphological operations in local tensor representation of the image. I apply a multiscale top-hat with a line structuring element at different scales and orientations. Then, I produce a stack of top-hat images and combine them into a local tensor, find the eigenvalues to calculate vesselness and neuriteness to enhance the curvilinear structure in the biomedical images. This approach works with 2D and 3D images.

Compared with other existing approaches, the gathered results prove that our proposed approach achieves high-quality curvilinear structure enhancement in the synthetic examples and in a wide range of real 2D and 3D biomedical image types.

7.2 Method

In this Section, I introduce the proposed approach that consolidates the advantages of mathematical morphology and local tensor representation to enhance curvilinear structures in 2D/3D images.

7.2.1 Proposed Method Framework

Since curvilinear structures can appear at different scales and directions in images, a top-hat transform using multiscale and multi-directional structuring elements should be applied to detect them.

The image is processed by using line structuring elements of different sizes (scale) and directions (orientations) and is then represented as a tensor, the Multiscale Top-Hat Tensor (MTHT), which intrinsically contains information on scale and orientation. Then, through the use of its eigenvalues and eigenvectors, vesselness and neuriteness are calculated to enhance curvilinear structures. The details of the proposed approach are given below.

Multiscale Top-Hat Transform

For a given 2D/3D grayscale image $I(\mathbf{p})$, where $\mathbf{p}$ donates the pixel position, a stack of 2D/3D line structuring elements $B_{\sigma_i,\mathbf{u}_j}$, for m different scales σ_i and n different orientations $\mathbf{u}_j$, is defined.

In 2D, the $\mathbf{u}_j$ orientation of line structuring element is defined as follows;

$$\mathbf{u}_j = [cos(\theta_j), sin(\theta_j)]^T, \tag{7.1}$$

where $\theta_j \in [0; 180)$.

In 3D, as proposed in [17, 129], a point distribution on the sphere of unit radius is used to define the orientation $\mathbf{u}_j$ of the 3D line structuring element as follows;

$$\mathbf{u}_j = [sin(\theta_j)cos(\phi_j), sin(\theta_j)sin(\phi_j), cos(\theta_j)]^T, \tag{7.2}$$

where $\theta_j \in [0; 180]$ and $\phi_j \in [0; 360)$.

Then, I produced a top-hat image using a line structuring element defined by scale σ_i and orientation $\mathbf{u}_j$ as follows;

$$TH(\mathbf{p})_{\sigma_i,\mathbf{u}_j} = I(\mathbf{p}) - (I \circ B_{\sigma_i,\mathbf{u}_j})(\mathbf{p}). \tag{7.3}$$

Tensor Representation

In general, the tensor representation of an image can provide information about how much the image differs along and across the dominant orientations within a particular region [16].

In our case, the local tensor $T(\mathbf{p})_{\sigma_i}$ representation of an image $I(\mathbf{p})$ is generated by combining the bank of top-hat images from Equation 7.3 as follows;

$$T(\mathbf{p})_{\sigma_i} = \sum_{j=1}^{n} \|TH(\mathbf{p})_{\sigma_i,\mathbf{u}_j}\| (\mathbf{u}_j \mathbf{u}_j^T). \tag{7.4}$$

MTHT-Vesselness

As described in Chapter 2, piecewise curvilinear segments can be detected by analysing the relations between eigenvalues and eigenvectors of the locally calculated Hessian [4].

In a similar way [10], the vesselness of the proposed approach is defined where the eigenvalues of the Hessian matrix are substituted with those of the MTHT. Finally, multiscale vesselness, for a given set of m scales can be calculated as follows;

$$V = \max_i \left(V_{\sigma_i} \right) . \tag{7.5}$$

MTHT-Neuriteness

When combining the neuriteness with our approach, it is necessary to modify the neuriteness measurement introduced by [8] for 2D and 3D images respectively. In [8], they normalised eigenvalues correspondingly to the smaller absolute eigenvalue which is a negative value. Whereas, in our approach, I used a morphological line structuring element instead of the second order derivative of the Gaussian function used by [8], so the smaller absolute eigenvalue will be equal to 0. The modified neuriteness Equation is;

$$N_{\sigma_i} = \begin{cases} \dfrac{\lambda}{\lambda_{max}} & \text{if } \lambda > 0 \\ 0 & \text{if } \lambda = 0 \end{cases} , \tag{7.6}$$

where λ is the larger in the magnitude of the two eigenvalues λ_1 and λ_2 for 2D images or the larger in the magnitude of the three eigenvalues λ_1, λ_2 and λ_3 for 3D images. λ_{max} denotes the largest λ over all pixels in the image. Similar to vesselness, a multiscale neuriteness can be calculated as;

$$N = \max_i \left(N_{\sigma_i} \right) . \tag{7.7}$$

7.3 Results

In this Section, I present quantitative and qualitative validations for the proposed approach against both synthetic and real-world 2D and 3D imaging data. I then compare the results with state-of-the-art approaches. In order to validate the approach quantitatively in 2D and 3D images, I calculate the Receiver Operating Characteristic (ROC) curve and the Area Under the Curve (AUC), further details can be found in [143].

7.3.1 Application to 2D Retinal Images

Although a visual inspection can provide some information regarding the effectiveness of the curvilinear structure enhancement approaches, a more rigorous form of quantitative validation is required. As in [9], I chose to use the Receiver Operating Characteristic (ROC) curve and the Area Under the Curve (AUC) metrics to compare the curvilinear structure enhancement approaches. I derive the ROC curve and then calculate the AUC value. Each enhanced image is segmented at different threshold levels and compared with the corresponding ground truth segmentation of curvilinear structures in the image. I measure the quality of the approach by using publicly available retinal image datasets: DRIVE [162], STARE [142] and HRF [3]. These datasets have been chosen because of their availability and their ground truth data. I have used these ground truth segmentations to quantitatively compare the proposed approach with the other curvilinear structure enhancement approaches.

In particular, I evaluate our approach, alongside the vesselness [4], Zana's top-hat [15], neuriteness [8] and RORPO [94] approaches, calculating the Receiver Operating Characteristic (ROC) curve and the mean of Area Under the Curve (AUC) between the enhanced images and the ground truth. The results are displayed accordingly in Figure 7.1, Figure 7.2 and Table 7.1. A higher AUC value indicates

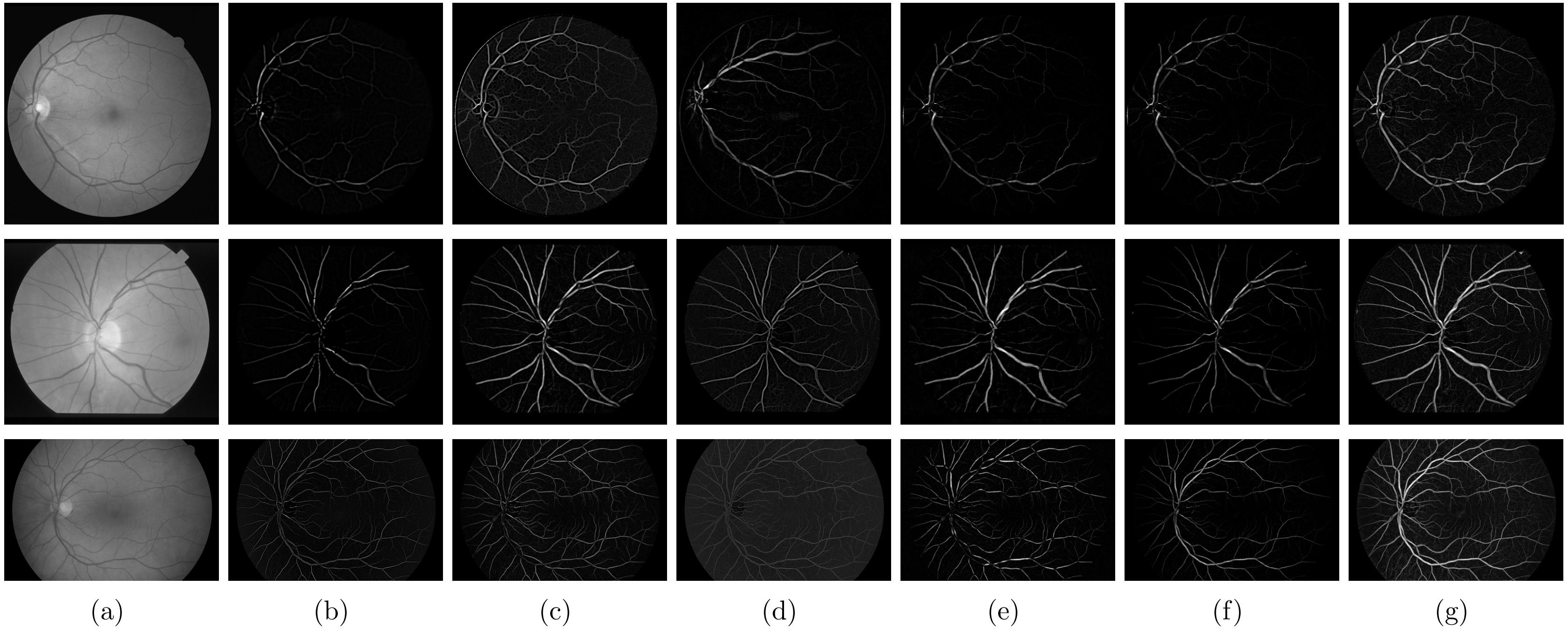

Figure 7.1: A selection of 2D retina images alongside the enhanced images by the state-of-the-art approaches and by the proposed MTHT-based approaches. (a) is the original grayscale images from the DRIVE, STARE, and HRF retina dataset, (b) Vesselness [4], (c) Zana's top-hat [15], (d) Neuriteness [8], (e) RORPO [94], (f) MTHT-vesselness, and (g) MTHT-neuriteness.

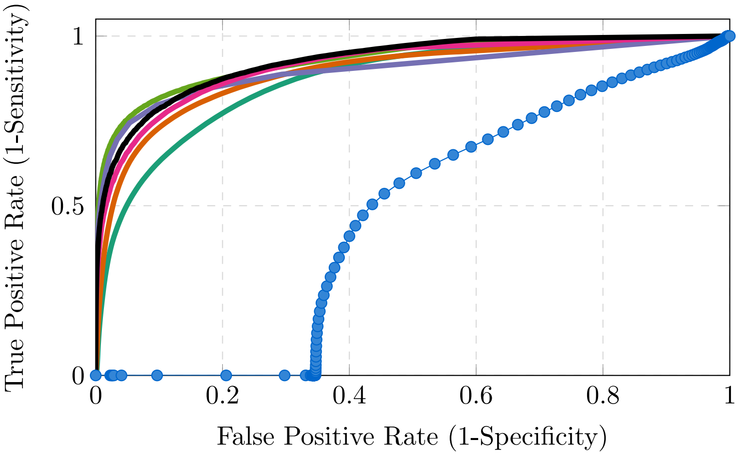

(a) DRIVE

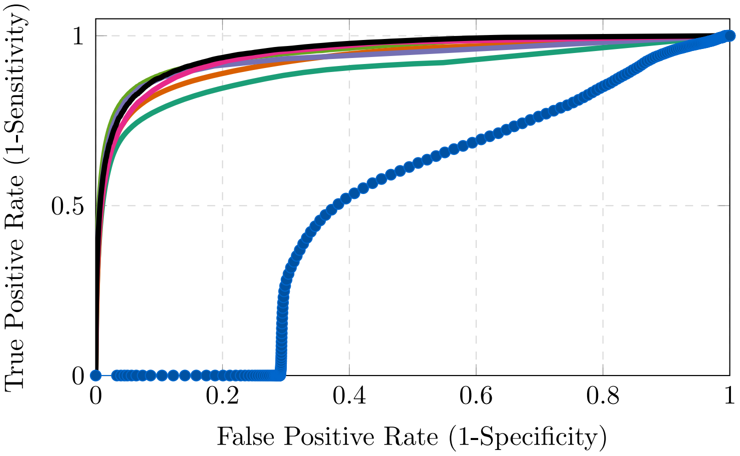

(b) STARE

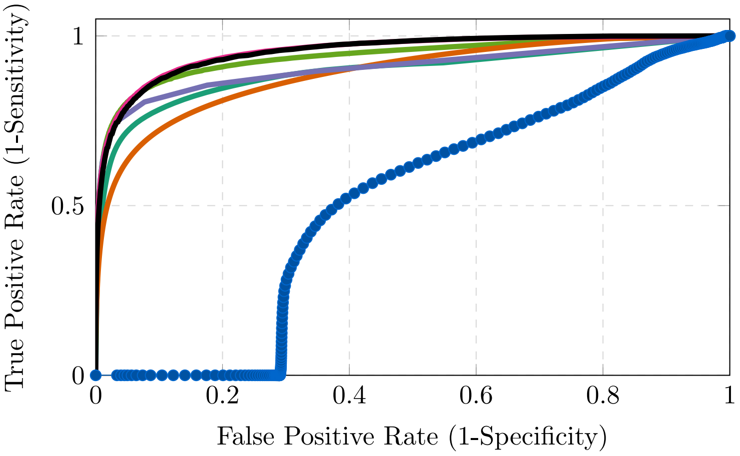

(c) HRF (healthy)

Figure 7.2: Mean ROC curves are calculated for all the 2D retinal images in: (a) DRIVE, (b) STARE, and (c) HRF datasets enhanced using the state-of-the-art approaches alongside the proposed MTHT-vesselness and MTHT-neuriteness (see legend for colours). Correspondingly, the mean AUC values for all datasets can be found in Table 7.1.

Enhancement Approach	AUC (StDev)			
	DRIVE	STARE	HRF (healthy)	HRF (unhealthy)
Raw image	0.416 (0.064)	0.490 (0.076)	0.530 (0.075)	0.541 (0.073)
Vesselness	0.888 (0.243)	0.898 (0.215)	0.913 (0.020)	0.904 (0.020)
Zana's top-hat	**0.933 (0.015)**	0.956 (0.021)	0.943 **(0.010)**	0.910 (0.016)
Neuriteness	0.909 (0.022)	0.927 (0.039)	0.896 (0.024)	0.879 (0.059)
RORPO	0.867 (0.016)	0.902 (0.020)	0.869 (0.014)	0.854 **(0.015)**
MTHT-vesselness	0.923 (0.017)	0.955 (0.024)	**0.959** (0.012)	0.934 **(0.015)**
MTHT-neuriteness	0.931 (0.016)	**0.958 (0.019)**	**0.959 (0.010)**	**0.935** (0.018)

Table 7.1: Mean AUC values for the state-of-the-art approaches, and proposed MTHT-vesselness and MTHT-neuriteness across the DRIVE, STARE and HRF datasets. A selection of results are shown in Figure 7.1 and the mean ROC curves can be seen in Figure 7.2. The best results for each dataset are in bold.

a better enhancement of curvilinear structures, with a value of 1 indicating that the enhanced image is identical to the ground truth image.

Our experimental results clearly show that our proposed approach works better than the state-of-the-art approaches for the STARE dataset. Furthermore, the proposed approach achieved a high score overall on the HRF healthy and unhealthy images, as illustrated in Table 7.1.

The average computation time for the proposed method is 13.7 seconds for DRIVE image and 16.4 seconds for STARE image. Please make a note that the proposed method has been implemented and tested in Matlab, however, C++ implementation could be much faster.

7.3.2 3D Vascular Network Complexity

In order to validate our approach in 3D, I used synthetic vascular networks produced by the free software package called VascuSynth [163]. The tree generation is performed by iteratively growing a vascular structure based on an oxygen demand map. Each generated image is associated with its ground truth. In this experiment, I generated 9 volumetric images with increasing complexity and their corresponding

	AUC				
Nodes	Vesselness [4]	Neuriteness [8]	RORPO [95]	MTHT-vesselness	MTHT-neuriteness
5	0.999	0.923	0.999	**1.000**	0.992
10	0.996	0.883	0.997	**1.000**	0.998
50	0.976	0.830	0.965	**0.999**	0.982
100	0.951	0.778	0.930	**0.999**	0.988
200	0.930	0.755	0.900	**0.998**	0.981
400	0.910	0.746	0.879	**0.996**	0.975
600	0.902	0.743	0.869	**0.993**	0.970
800	0.885	0.719	0.855	**0.987**	0.959
1000	0.884	0.722	0.852	**0.983**	0.956
mean (StDev)	0.937 (0.045)	0.788 (0.073)	0.916 (0.058)	**0.995 (0.006)**	0.978 (0.014)

Table 7.2: AUC values for 9 3D curvilinear network images with increasing network's complexity (see Figure 7.3) enhanced with the state-of-the-art approaches alongside the proposed MTHT-vesselness and MTHT-neuriteness. The best results for each dataset are in bold.

ground truth. In addition, in order to make the image more realistic, I added a small amount of Gaussian noise of level $\sigma^2 = 10$ and applied a Gaussian smoothing kernel with a standard deviation of 1. The results, in terms of AUC, are presented in Table 7.2 and a sample of the results are shown in Figure 7.3. I also demonstrate the mean ROC curve over the 9 enhanced images, as shown in Figure 7.4. Our proposed approach is compared with vesselness [4], neuriteness [8] and with the latest 3D enhancement approach [95]. Our proposed approach clearly has the highest mean AUC value (0.995) with a standard deviation equal to (0.006) for the proposed MTHT-vesselness. On the other hand, I obtained an AUC value (0.978) with a standard deviation equal to (0.014) for the proposed MTHT-neuriteness compared to the state-of-art approaches.

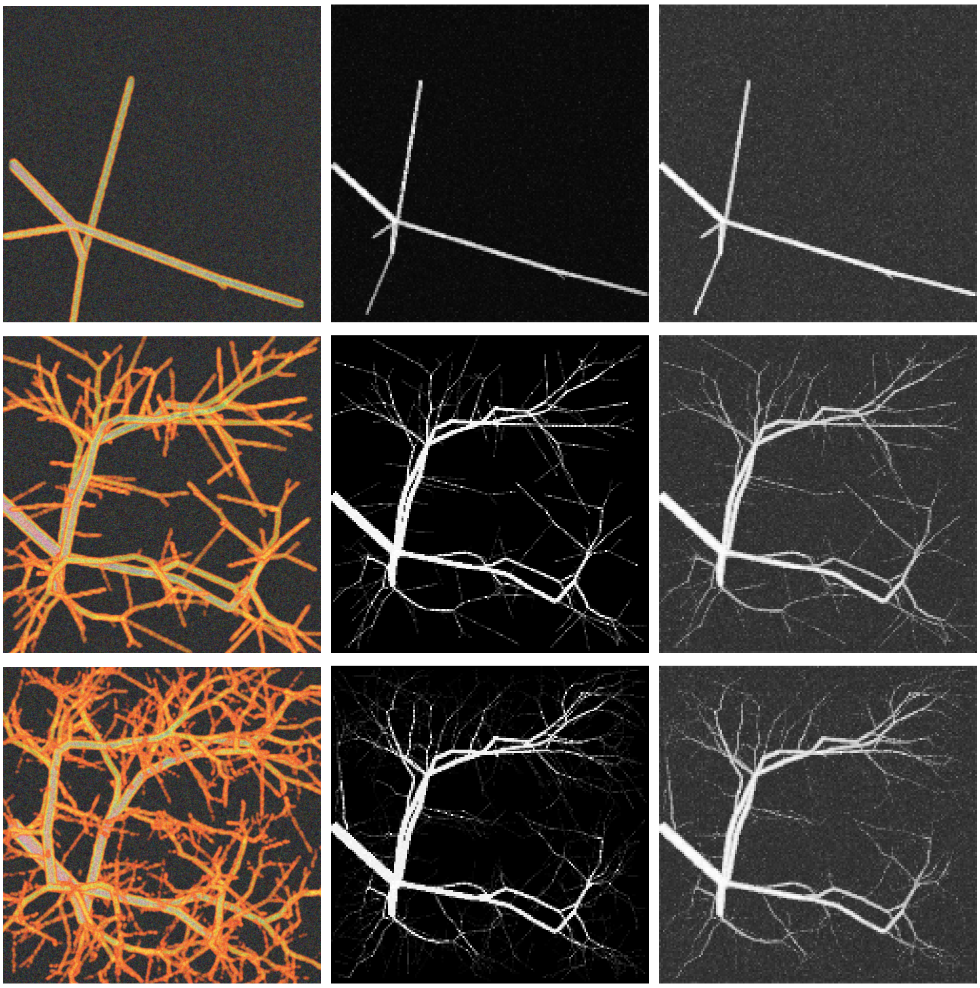
(a) (b) (c)

Figure 7.3: A selection of 3D synthetic vascular network images generated with the VascuSynth software. Each image has a resolution of (167x167x167 voxels) and have different nodes to increase the complexity of structure. (a) original images with different number of nodes (5, 200 and 1000) respectively. (b-c) are the enhanced images from the proposed MTHT-vesselness and MTHT-neuriteness respectively.

7.3.3 2D and 3D Qualitative Validation

Additionally, as displayed in Figure 7.5 and Figure 7.6, I have demonstrated the robustness of the proposed approach when applied to a wide range of 2D and 3D real-world images. It is clear that our approach has the best performance compared with the state-of-the-art approaches. In particular, our proposed approach can handle complex curvilinear networks as shown in Figure 7.6(1)f and (2)f.

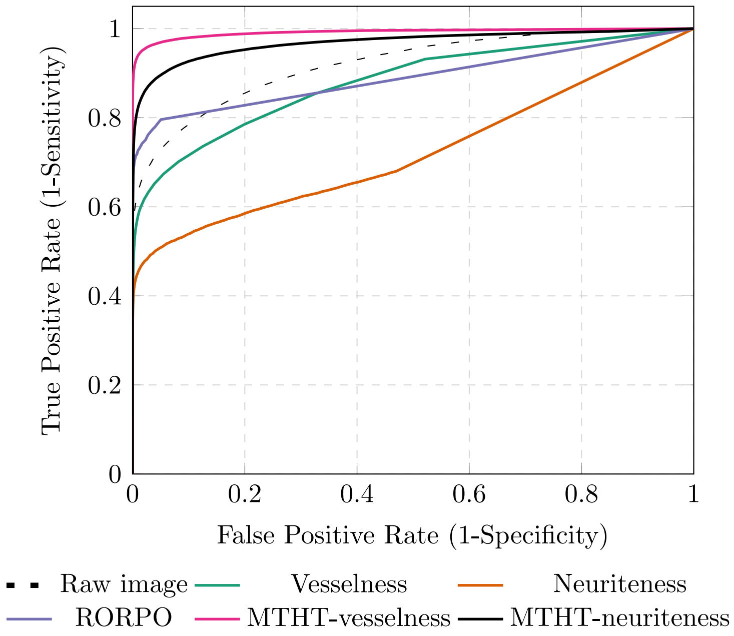

Figure 7.4: Mean ROC curve for all 3D curvilinear network images enhanced using the state-of-the-art approaches alongside the proposed MTHT-vesselness and MTHT-neuriteness (see legend for colours). Correspondingly, the mean AUC values can be found in Table 7.2.

7.4 Implementation

The software was implemented and written in MATLAB 2017a on Windows 8.1 pro 64-bit PC running an Intel Core i7-4790 CPU (3.60 GHz) with 16 GB RAM. The software is made available at: https://github.com/ShuaaAlharbi/MTHT.

7.5 Conclusion

The enhancement of curvilinear structures is important for many image processing applications. In this research, I have proposed a novel approach that combines the advantages of a morphological multiscale top-hat transform and a local tensor to enhance the curvilinear structures in a wide range of 2D and 3D biological and medical images.

The proposed MTHT approach is evaluated qualitatively and quantitatively using

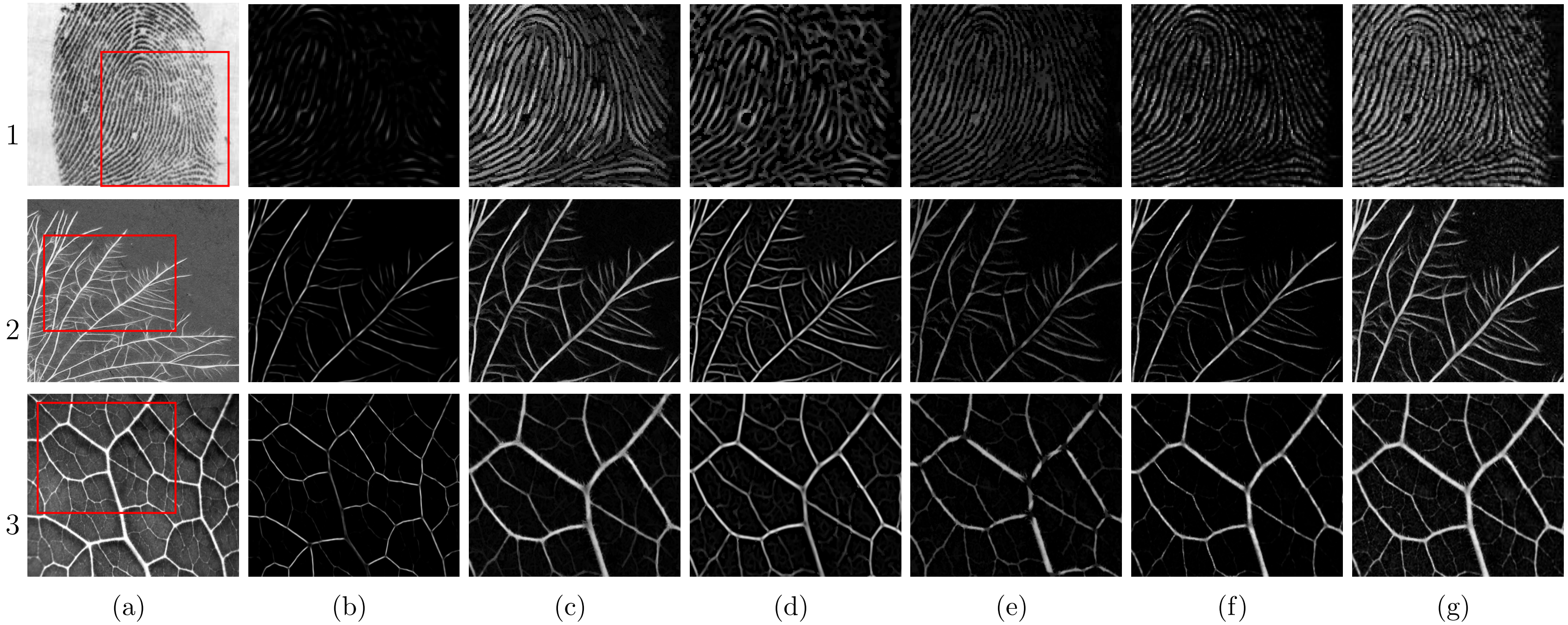

Figure 7.5: Comparison of the curvilinear structure enhancement approaches using 2D real images. (a) original images: (1) finger print [164], (2) macro-scale networks (provided by Prof. M. Fricker, Oxford University, UK), and (3) leaf image [10]. (b) Vesselness [4], (c) Zana's top-hat [15], (d) Neuriteness [8], (e) RORPO [94], (f) MTHT-vesselness, and (g) MTHT-neuriteness. The red box on the original image shows the region of interest.

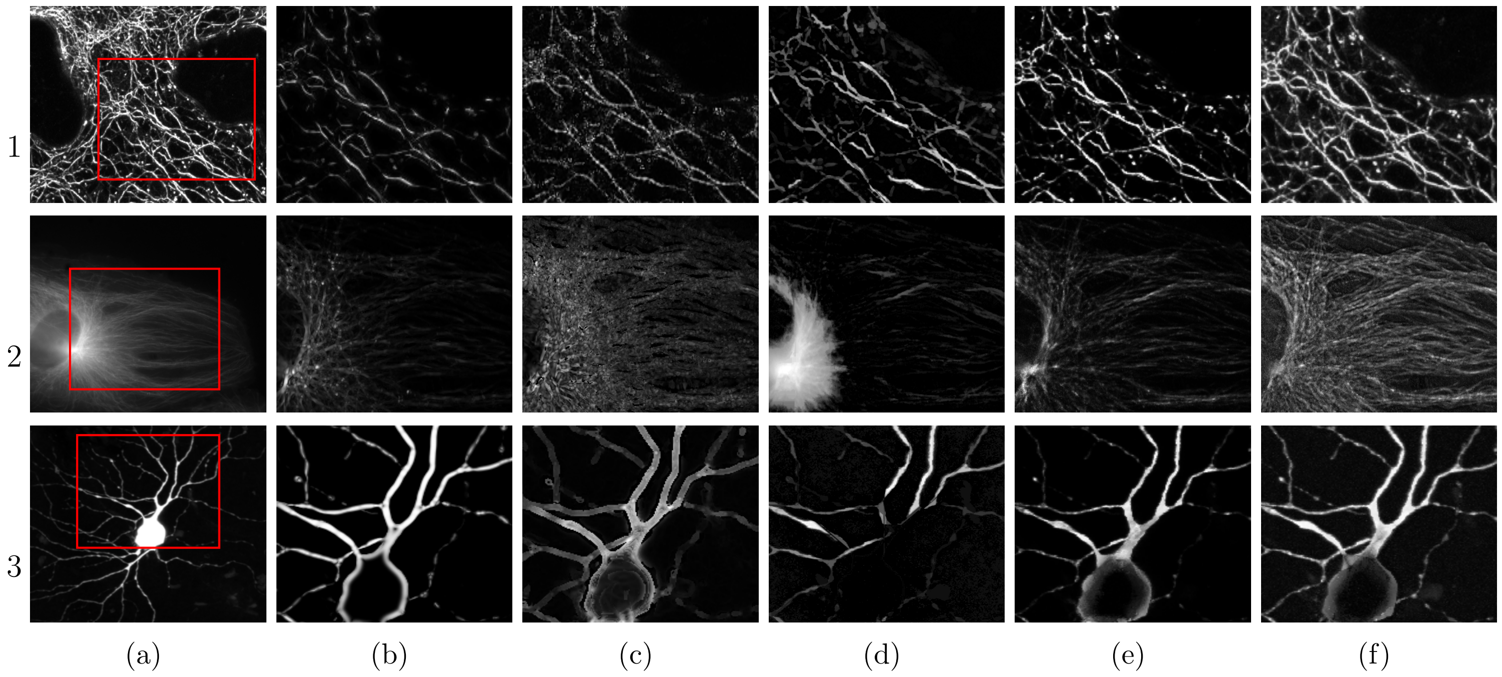

(a) (b) (c) (d) (e) (f)

Figure 7.6: Comparison of the curvilinear structure enhancement approaches using 3D real images. (a) original images: (1) keratin network in a skin cell (Dr. Tim Hawkins, Durham University, UK), (2) microtubules [165], and (3) neuronal (provided by Dr. Chris Banna, UC Santa Barbara, USA). (b) Vesselness [4] , (c) Neuriteness [8], (d) RORPO [95], (e) MTHT-vesselness, and (f) MTHT-neuriteness. All images are seen with a Maximum Intensity Projection. The red box on the original image shows the region of interest.

different 2D and 3D images. The experimental results show that the approach is comparable with the Hessian-based vesselness and neuriteness approaches, as well with the Zana's top-hat and RORPO approach. In general, the MTHT proposed approach showed better enhancement results compared with the state-of-art approaches. Although the proposed approach achieves good enhancement results in all tested biomedical images, there is room for improvement. In particular, the top-hat transform using different structuring elements for an improved enhancement of the image background, as well as better handling of junctions should be explored further.

Epilogue

The proposed approach is validated on synthetic and real data, and is also compared to the state-of-the-art approaches. The results show that the proposed approach achieves high-quality curvilinear structure enhancement in synthetic examples and in a wide range of 2D and 3D images. This approach is shown to be able to cope with variations in contrast and noise.

Chapter 8

Contributions and Conclusions

> *On the one hand, philosophy is to keep us thinking about things that we may come to know, and on the other hand to keep us modestly aware of how much that seems like knowledge isn't knowledge.*
>
> — Bertrand Russell

In this thesis, firstly, I reviewed the image enhancement methods in the literature to provide a general idea of what people search and achieve so far. Later in the following part, I explain the basic ideas behind mathematical morphology before pass on to discuss image enhancement and introducing a recently developed approach for curvilinear structure enhancement based on mathematical morphology. Most of the parts after the morphology part are related to mathematical morphology.

In this thesis, I detailed the extension of phase-based tensor method to enhance curvilinear structures in the frequency domain in 3D images. I have introduced new techniques for the enhancement of images and the detection and measurement of objects in biomedical images. These methods have been built upon the ideas and concepts of mathematical morphology and tensor representation. To overcome one of the more challenging problems regarding the enhancement the curvilinear structures, contrast dependency, I have introduced 3D phase congruency tensor. I have combined the power of the phase congruency, free from the contrast changes in the image, with the tensor representation that increases the number of orientation. I have applied this method to real data in 3D cases, and the results have been proved that the enhancement method is promising.

On the basis of the character of curvilinear structures in images, I have introduced a new curvilinear structure enhancement method, the bowler-hat transform 2D and 3D (Chapter 5 (*p.* 55) and Chapter 6 (*p.* 86)), validating the results on synthetic data, comparing to existing methods and showing the enhancement capacity of this approach on real-world data. Bowler-hat transforms are simple and effective to enhance curvilinear structures in biomedical images. I have shown that the bowler-hat transforms are powerful enhancement approaches that better in most cases than comparator methods in synthetic and real scenarios.

Finally, I have carried out my studies into one combined method which multiscale top-hat tensor again in 2D and 3D images (Chapter 7 (*p.* 103)). Here, I have applied the different type of real word examples either 2D or 3D to enhance curvilinear structures.

This thesis constitutes a series of contributions to the research area of image processing and analysis, especially within the field of mathematical morphology. Phase congruency and tensor representation. These new approaches have been shown to work well on noisy and complicated real-world data, such as medical and biological images and, despite the popular direction towards deep learning, like these will likely have a significant role to play in biomedical image processing for following several years to come.

8.1 Contributions to the Field

This thesis includes a series of contributions to the field of image processing and analysis, particularly mathematical morphology.

Firstly, in Chapter 2 (*p.* 8), I reviewed the image enhancement methods in the literature to provide a general idea of what people search and achieve so far. This Chapter is also prepared to demonstrate which method is suitable for which reason. So, researchers can use as a reference guide for their research before diving into the field. All curvilinear features enhancement approaches introduced here, are also used as comparator methods in the following Chapters.

Then, I detailed the extension of phase congruency tensor-based method to enhance curvilinear structures in 3D images. This method proposes an intensity-independent solution to any intensity variation problem that traditional curvilinear structures enhancement methods suffer from.

Then, in the following Chapter 3 (*p.* 31), I explain the basic ideas behind mathematical morphology before pass on to discuss image enhancement and introducing a recently developed approach for curvilinear structure enhancement based on mathematical morphology. This Chapter is supported by the simple binary image to explain how the mathematical morphology works and its operations'. All the Chapters after the morphology Chapter are related to mathematical morphology operations.

In Chapter 5 (*p.* 55), a 2D image enhancement method, called bowler-hat transform, has been introduced. The bowler-hat transform has been validated against comparator methods using both synthetic and real image data (retinal).

In Chapter 6 (*p.* 86), I proposed an extension of the bowler-hat transform into 3D. The 3D bowler-hat transform is validated quantitatively and qualitatively in both synthetic and real-world medical images.

Finally, I introduce another image enhancement method based on mathematical morphology concept combined with the tensor representation of an image in 2D and 3D, see Chapter 7 (*p.* 103).

8.2 Future Work

As a future work, it would be more interesting to asses the behaviour of the proposed methods in this thesis in datasets where other nearby structures are present, like in many biomedical images.

Also, the 3D PCT concept may be extended, instead of the 3D Hessian matrix-based approach, into 3D anisotropic diffusion schemes [136] and into 3D live-wire tracing concepts [8]. Moreover, the 2D and 3D bowler-hat transform concept may be extended into blob-like structures enhancement variants. Finally, a more extensive validation of the 2D and 3D bowler-hat transform-based concepts with a much wider range of biomedical imaging datasets would be beneficial.

MTHT transform, proposed in Chapter 7 (*p.* 103), achieves good enhancement results in all tested biomedical images, however, there is still a room for improvement. In particular, the MTHT methods are quite sensitive to noise. The potential improvement may involve an introduction of a noise suppression, (*i.e.* Gaussian kernel) which could help to reduce the noise in the enhanced image. On the other hand, a combination of different structuring elements, as done in the top-hat transform, may improved the enhancement as well as better handling of junctions.

Bibliography

1. Obara, B., Grau, V. & Fricker, M. D. A Bioimage informatics approach to automatically extract complex fungal networks. *Bioinformatics* **28,** 2374–2381 (2012) (*p.* 2).
2. Wikimedia. *Microtubuler Image* https://commons.wikimedia.org/wiki/File:Btub.jpg. 2006 (*pp.* 2, 4).
3. Odstrcilik, J., Kolar, R., Budai, A., Hornegger, J., Jan, J., Gazarek, J., Kubena, T., Cernosek, P., Svoboda, O. & Angelopoulou, E. Retinal vessel segmentation by improved matched filtering: evaluation on a new high-resolution fundus image database. *IET Image Processing* **7,** 373–383 (2013) (*pp.* 2, 10, 70, 77, 79, 108).
4. Frangi, A. F., Niessen, W. J., Vincken, K. L. & Viergever, M. A. *Multiscale vessel enhancement filtering* in *International Conference on Medical Image Computing and Computer-Assisted Intervention* (1998), 130–137 (*pp.* 1, 9–10, 12–15, 42, 48, 56–57, 72, 77, 87, 91, 107–109, 112, 115–116).
5. Sato, Y., Nakajima, S., Atsumi, H., Koller, T., Gerig, G., Yoshida, S. & Kikinis, R. 3D multi-scale line filter for segmentation and visualization of curvilinear structures in medical images. *Medical Image Analysis* **2,** 143–168 (1998) (*pp.* 1, 3, 10).
6. Krissian, K., Malandain, G., Ayache, N., Vaillant, R. & Trousset, Y. Model-based detection of tubular structures in 3D images. *Computer Vision and Image Understanding* **80,** 130–171 (2000) (*pp.* 1, 15).

7. Koller, T. M., Gerig, G., Szekely, G. & Dettwiler, D. *Multiscale detection of curvilinear structures in 2-D and 3-D image data* in *Fifth International Conference on Computer Vision* (1995), 864–869 (*pp.* 1, 10, 12).

8. Meijering, E., Jacob, M., Sarria, J.-C., Steiner, P., Hirling, H. & Unser, M. Design and validation of a tool for neurite tracing and analysis in fluorescence microscopy images. *Cytometry* **58,** 167–176 (2004) (*pp.* 1, 13, 16–17, 48, 72, 77, 91, 107–109, 112, 115–116, 121).

9. Jerman, T., Pernuš, F., Likar, B. & Špiclin, Ž. Enhancement of Vascular Structures in 3D and 2D Angiographic Images. *IEEE Transactions on Medical Imaging* **35,** 2107–2118 (2016) (*pp.* 1, 8–9, 17–18, 72, 77, 91, 108).

10. Obara, B., Fricker, M., Gavaghan, D. & Grau, V. Contrast-independent curvilinear structure detection in biomedical images. *IEEE Transactions on Image Processing* **21,** 2572–2581 (2012) (*pp.* 1, 4, 9, 12, 18, 22–23, 42–43, 48, 56, 66, 72, 77, 107, 115).

11. Bankhead, P., Scholfield, C. N., McGeown, J. G. & Curtis, T. M. Fast retinal vessel detection and measurement using wavelets and edge location refinement. *PloS One* **7,** e32435 (2012) (*pp.* 1, 25–26, 56, 72, 77, 79).

12. Kovesi, P. *Invariant measures of image features from phase information* (University of Western Australia, 1996) (*p.* 1).

13. Serra, J. *Image Analysis and Mathematical Morphology* (Academic Press, 1982) (*pp.* 1, 31).

14. Lee, J., Haralick, R. & Shapiro, L. Morphologic edge detection. *IEEE Journal on Robotics and Automation* **3,** 142–156 (1987) (*pp.* 1, 31).

15. Zana, F. & Klein, J.-C. Segmentation of vessel-like patterns using mathematical morphology and curvature evaluation. *IEEE Transactions on Image Processing* **10,** 1010–1019 (2001) (*pp.* 1, 104, 108–109, 115).

16. Knutsson, H. *Representing local structure using tensors* in *6th Scandinavian Conference on Image Analysis* (1989), 244–251 (*pp.* 1, 41, 43, 104, 106).

17. Sazak, Ç. & Obara, B. *Contrast-independent curvilinear structure enhancement in 3D biomedical images* in *IEEE International Symposium on Biomedical Imaging* (2017), 1165–1168 (*pp.* 1, 3, 18, 22, 41, 87, 91, 106).

18. Sazak, Ç., Nelson, C. J. & Obara, B. The multiscale bowler-hat transform for blood vessel enhancement in retinal images. *Pattern Recognition* **88,** 739–750 (2019) (*pp.* 2, 55, 72, 87–88).

19. Sazak, Ç., Nelson, C. J. & Obara, B. *The multiscale bowler-hat transform for curvilinear structure enhancement in 3D biomedical images* in *British Machine Vision Conference* (2018) (*pp.* 2, 87).

20. Fan, J., Zhou, X., Dy, J. G., Zhang, Y. & Wong, S. T. An automated pipeline for dendrite spine detection and tracking of 3D optical microscopy neuron images of in vivo mouse models. *Neuroinformatics* **7,** 113–130 (2009) (*p.* 3).

21. Engel, A., Schoenenberger, C.-A. & Müller, D. J. High resolution imaging of native biological sample surfaces using scanning probe microscopy. *Current opinion in structural biology* **7,** 279–284 (1997) (*p.* 3).

22. Shapiro, F. Variable conformation of GAP junctions linking bone cells: A transmission electron microscopic study of linear, stacked linear, curvilinear, oval, and annular junctions. *Calcified tissue international* **61,** 285–293 (1997) (*p.* 3).

23. Eberhardt, C. & Clarke, A. Automated reconstruction of curvilinear fibres from 3D datasets acquired by X-ray microtomography. *Journal of microscopy* **206,** 41–53 (2002) (*p.* 3).

24. Westin, C.-F., Wigström, L., Loock, T., Sjöqvist, L., Kikinis, R. & Knutsson, H. Three-dimensional adaptive filtering in magnetic resonance angiography. *Journal of Magnetic Resonance Imaging* **14,** 63–71 (2001) (*p.* 3).

25. Hata, T., Takahashi, H., Watanabe, K., Takahashi, M., Taguchi, K., Itoh, T. & Todo, S. Magnetic resonance imaging for preoperative evaluation of breast cancer: a comparative study with mammography and ultrasonography. *Journal of the American College of Surgeons* **198,** 190–197 (2004) (*p.* 3).

26. Mastropasqua, L., Toto, L., Mattei, P. A., Vecchiarino, L., Mastropasqua, A., Navarra, R., Di Nicola, M. & Nubile, M. Optical coherence tomography and 3-dimensional confocal structured imaging system guided femtosecond laser capsulotomy versus manual continuous curvilinear capsulorhexis. *Journal of Cataract & Refractive Surgery* **40,** 2035–2043 (2014) (*p.* 3).

27. Tomer, R., Khairy, K., Amat, F. & Keller, P. J. Quantitative high-speed imaging of entire developing embryos with simultaneous multiview light-sheet microscopy. *Nature Methods* **9,** 755–763 (2012) (*p.* 3).

28. Duncan, J. S. & Ayache, N. Medical image analysis: progress over two decades and the challenges ahead. *IEEE Transactions on Pattern Analysis and Machine Intelligence* **22,** 85–106 (2000) (*p.* 3).

29. Myers, G. Why bioimage informatics matters. *Nature Methods* **9,** 659–660 (2012) (*p.* 3).

30. Zana, F. & Klein, J.-C. A multimodal registration algorithm of eye fundus images using vessels detection and Hough transform. *IEEE Transactions on Medical Imaging* **18,** 419–428 (1999) (*pp.* 3, 8).

31. Maragos, P. in *Handbook of Image and Video Processing* 2nd. Chapter 3.3 (Elsevier Academic, 2005) (*p.* 3).

32. Orlando, J. I. & Blaschko, M. *Learning fully-connected CRFs for blood vessel segmentation in retinal images* in *International Conference on Medical Image Computing and Computer-Assisted Intervention* (2014), 634–641 (*pp.* 3, 77, 79).

33. Sigursson, E. M., Valero, S., Benediktsson, J. A., Chanussot, J., Talbot, H. & Stefansson, E. Automatic retinal vessel extraction based on directional mathematical morphology and fuzzy classification. *Pattern Recognition Letters* **47,** 164–171 (2014) (*pp.* 3, 29).

34. Hadjidemetriou, S., Duncan, J. S., Toomre, D. & Tuck, D. *Automatic quantification of microtubule dynamics* in *IEEE International Symposium on Biomedical Imaging: Nano to Macro* (2004), 656–659 (*p.* 3).

35. Peters, R. A. A new algorithm for image noise reduction using mathematical morphology. *IEEE transactions on Image Processing* **4,** 554–568 (1995) (*pp.* 4, 10).

36. Bibiloni, P., Gonzalez-Hidalgo, M. & Massanet, S. General-purpose curvilinear object detection with fuzzy mathematical morphology. *Applied Soft Computing* **60,** 655–669 (2017) (*pp.* 4, 104).

37. Shui, P.-L. & Zhang, W.-C. Noise-robust edge detector combining isotropic and anisotropic Gaussian kernels. *Pattern Recognition* **45,** 806–820 (2012) (*p.* 4).

38. Sum, K. & Cheung, P. Y. Vessel extraction under non-uniform illumination: a level set approach. *IEEE Transactions on Biomedical Engineering* **55,** 358–360 (2008) (*p.* 4).

39. Setiawan, A. W., Mengko, T. R., Santoso, O. S. & Suksmono, A. B. *Color retinal image enhancement using CLAHE* in *International Conference on ICT for Smart Society* (2013), 1–3 (*p.* 5).

40. Ortiz, S. H. C., Chiu, T. & Fox, M. D. Ultrasound image enhancement: A review. *Biomedical Signal Processing and Control* **7,** 419–428 (2012) (*pp.* 5, 87).

41. Staal, J., Abramoff, M., Niemeijer, M., Viergever, M. & van Ginneken, B. Ridge based vessel segmentation in color images of the retina. *IEEE Transactions on Medical Imaging* **23,** 501–509 (2004) (*pp.* 9, 70, 77, 79).

42. Schuh, M., Banda, J., Bernasconi, P., Angryk, R. & Martens, P. A comparative evaluation of automated solar filament detection. *Solar Physics* **289,** 2503–2524 (2014) (*p.* 8).

43. Tupin, F., Maitre, H., Mangin, J.-F., Nicolas, J.-M. & Pechersky, E. Detection of linear features in SAR images : Application to road network extraction. *IEEE Transactions on Geoscience and Remote Sensing* **36,** 434–453 (1998) (*p.* 8).

44. Harris, C. & Stephens, M. *A combined corner and edge detector* in *Alvey Vision Conference* **15** (1988), 50 (*p.* 8).

45. Marr, D. & Hildreth, E. Theory of edge detection. *Proc. R. Soc. Lond. B* **207,** 187–217 (1980) (*p.* 8).

46. Hennersperger, C., Baust, M., Waelkens, P., Karamalis, A., Ahmadi, S.-A. & Navab, N. Multi-scale tubular structure detection in ultrasound imaging. *IEEE Transactions on Medical Imaging* **34,** 13–26 (2015) (*p.* 8).

47. Perona, P. & Malik, J. Scale-space and edge detection using anisotropic diffusion. *IEEE Transactions on Pattern Analysis and Machine Intelligence* **12,** 629–639 (1990) (*pp.* 8, 11).

48. Cohen, L. D. & Deschamps, T. *Grouping connected components using minimal path techniques application to reconstruction of vessels in 2D and 3D images* in *Computer Society Conference on Computer Vision and Pattern Recognition* **2** (2001), II–II (*p.* 8).

49. Benmansour, F. & Cohen, L. D. Tubular structure segmentation based on minimal path method and anisotropic enhancement. *International Journal of Computer Vision* **92,** 192–210 (2011) (*pp.* 8, 42, 87).

50. Sampat, M. P., Whitman, G. J., Bovik, A. C. & Markey, M. K. Comparison of algorithms to enhance spicules of spiculated masses on mammography. *Journal of Digital Imaging* **21,** 9–17 (2008) (*p.* 8).

51. Sanders, J. E., Goldstein, B. S., Leotta, D. F. & Richards, K. A. Image processing techniques for quantitative analysis of skin structures. *Computer Methods and Programs in Biomedicine* **59,** 167–80 (1999) (*p.* 8).
52. Su, R., Sun, C., Zhang, C. & Pham, T. D. A new method for linear feature and junction enhancement in 2D images based on morphological operation, oriented anisotropic Gaussian function and Hessian information. *Pattern Recognition* **47,** 3193–3208 (2014) (*p.* 8).
53. Liao, M., Zhao, Y.-q., Wang, X.-h. & Dai, P.-s. Retinal vessel enhancement based on multi-scale top-hat transformation and histogram fitting stretching. *Optics and Laser Technology* **58,** 56–62 (2014) (*pp.* 8, 104).
54. Demirel, H. & Anbarjafari, G. Image resolution enhancement by using discrete and stationary wavelet decomposition. *IEEE Transactions on Image Processing* **20,** 1458–1460 (2011) (*p.* 8).
55. Kirbas, C. & Quek, F. A Review of Vessel Extraction Techniques and Algorithms. *ACM Computing Surveys* **36,** 81–121 (2004) (*p.* 9).
56. Kovesi, P. *Phase congruency detects corners and edges* in *The Australian Pattern Recognition Society Conference* (2003), 309–318 (*pp.* 10, 18).
57. Mukhopadhyay, S. & Chanda, B. A multiscale morphological approach to local contrast enhancement. *Signal Processing* **80,** 685–696 (2000) (*p.* 10).
58. Su, R., Sun, C. & Pham, T. D. Junction detection for linear structures based on Hessian, correlation and shape information. *Pattern Recognition* **45,** 3695–3706 (2012) (*pp.* 10, 56).
59. Jerman, T., Pernuš, F., Likar, B. & Špiclin, Ž. *Beyond Frangi: An improved multiscale vesselness filter* in *SPIE Medical Imaging* (2015), 94132A–94132A (*pp.* 10, 48).
60. Lindeberg, T. Scale-space theory: A basic tool for analyzing structures at different scales. *Journal of applied statistics* **21,** 225–270 (1994) (*p.* 11).

61. Adelson, E. H., Anderson, C. H., Bergen, J. R., Burt, P. J. & Ogden, J. M. Pyramid methods in image processing. *RCA engineer* **29,** 33–41 (1984) (*p.* 11).

62. Weickert, J. *Anisotropic diffusion in image processing* (1998) (*p.* 11).

63. Zheng, S., Yuille, A. & Tu, Z. Detecting object boundaries using low-, mid-, and high-level information. *Computer Vision and Image Understanding* **114,** 1055–1067 (2010) (*p.* 11).

64. Canny, J. *A computational approach to edge detection* in *Readings in Computer Vision* (1987), 184–203 (*p.* 11).

65. Rebelo, M. S., Furuie, S. S., Gutierrez, M. A., Costa, E. & Moura, L. Multiscale representation for automatic identification of structures in medical images. *Computers in Biology and Medicine* **37,** 1183–1193 (2007) (*p.* 11).

66. Lindeberg, T. Edge detection and ridge detection with automatic scale selection. *International Journal of Computer Vision* **30,** 117–156 (1998) (*p.* 11).

67. Lindeberg, T. *Scale-space theory in computer vision* (Springer Science & Business Media, 2013) (*p.* 11).

68. Wang, Y., Ji, G., Lin, P. & Trucco, E. Retinal vessel segmentation using multiwavelet kernels and multiscale hierarchical decomposition. *Pattern Recognition* **46,** 2117–2133 (2013) (*pp.* 12, 77, 79).

69. Chan, T. F. & Vese, L. A. Active contours without edges. *IEEE Transactions on Image Processing* **10,** 266–277 (2001) (*p.* 12).

70. Kass, M., Witkin, A. & Terzopoulos, D. Snakes: Active contour models. *International journal of computer vision* **1,** 321–331 (1988) (*p.* 12).

71. Vincken, K. L., Koster, A. S. E. & Viergever, M. A. Probabilistic multiscale image segmentation. *IEEE Transactions on Pattern Analysis and Machine Intelligence* **19,** 109–120 (1997) (*p.* 12).

72. Petrovic, A., Escoda, O. D. & Vandergheynst, P. Multiresolution segmentation of natural images: from linear to nonlinear scale-space representations. *IEEE Transactions on Image Processing* **13,** 1104–1114 (2004) (*p.* 12).

73. Bibiloni, P., Gonzalez-Hidalgo, M. & Massanet, S. A survey on curvilinear object segmentation in multiple applications. *Pattern Recognition* **60,** 949–970 (2016) (*pp.* 13, 56).

74. Krissian, K., Ellsmere, J., Vosburgh, K., Kikinis, R. & Westin, C.-E. *Multiscale segmentation of the aorta in 3D ultrasound images* in *IEEE International Conference of the Engineering in Medicine and Biology Society* **1** (2003), 638–641 (*p.* 15).

75. Su, R., Sun, C., Zhang, C. & Pham, T. D. A new method for linear feature and junction enhancement in 2D images based on morphological operation, oriented anisotropic Gaussian function and Hessian information. *Pattern Recognition* **47,** 3193–3208 (2014) (*pp.* 15, 28, 56).

76. Al-Kofahi, Y., Dowell-Mesfin, N., Pace, C., Shain, W., Turner, J. N. & Roysam, B. Improved detection of branching points in algorithms for automated neuron tracing from 3D confocal images. *Cytometry Part A* **73,** 36–43 (2008) (*pp.* 17, 42, 48–49, 87).

77. Freeman, W. T. & Adelson, E. H. The design and use of steerable filters. *IEEE Transactions on Pattern Analysis & Machine Intelligence* **13,** 891–906 (1991) (*p.* 17).

78. Smafield, T., Pasupuleti, V., Sharma, K., Huganir, R. L., Ye, B. & Zhou, J. Automatic dendritic length quantification for high throughput screening of mature neurons. *Neuroinformatics* **13,** 443–458 (2015) (*p.* 17).

79. Jones, J. P. & Palmer, L. A. An evaluation of the two-dimensional Gabor filter model of simple receptive fields in cat striate cortex. *Journal of neurophysiology* **58,** 1233–1258 (1987) (*p.* 19).

80. Field, D. Scale-invariance and self-similar ‘wavelet’ transforms: an analysis of natural scenes and mammalian visual systems. *Wavelets, Fractals, and Fourier Transforms,* 151–193 (1993) (*pp.* 19, 21).

81. Pisano, E. D., Zong, S., Hemminger, B. M., DeLuca, M., Johnston, R. E., Muller, K., Braeuning, M. P. & Pizer, S. M. Contrast limited adaptive histogram equalization image processing to improve the detection of simulated speculations in dense mammograms. *Journal of Digital Imaging* **11,** 193–200 (1998) (*pp.* 24, 56, 72, 77).

82. Zhao, Y. Q., Wang, X. H., Wang, X. F. & Shih, F. Y. Retinal vessels segmentation based on level set and region growing. *Pattern Recognition* **47,** 2437–2446 (2014) (*p.* 24).

83. Zhang, J., Chen, Y., Bekkers, E., Wang, M., Dashtbozorg, B. & ter Haar Romeny, B. M. Retinal vessel delineation using a brain-inspired wavelet transform and random forest. *Pattern Recognition* **69,** 107–123 (2017) (*p.* 25).

84. Nguyen, U. T., Bhuiyan, A., Park, L. A. & Ramamohanarao, K. An effective retinal blood vessel segmentation method using multi-scale line detection. *Pattern Recognition* **46,** 703–715 (2013) (*pp.* 26–27, 56, 72, 77, 79).

85. Hou, Y. Automatic segmentation of retinal blood vessels based on improved multiscale line detection. *Journal of Computing Science and Engineering* **8,** 119–128 (2014) (*p.* 27).

86. Zana, F. & Klein, J. C. Segmentation of vessel-like patterns using mathematical morphology and curvature evaluation. *IEEE Transactions on Image Processing* **10,** 1010–1019 (2001) (*pp.* 28, 56, 72, 77).

87. Mendonca, A. M. & Campilho, A. Segmentation of retinal blood vessels by combining the detection of centerlines and morphological reconstruction. *IEEE Transactions on Medical Imaging* **25,** 1200–1213 (2006) (*p.* 28).

88. Kovesi, P. Phase congruency: A low-level image invariant. *Psychological Research* **64,** 136–148 (2000) (*p.* 28).

89. Fraz, M., Barman, S., Remagnino, P., Hoppe, A., Basit, A., Uyyanonvara, B., Rudnicka, A. & Owen, C. An approach to localize the retinal blood vessels using bit planes and centerline detection. *Computer Methods and Programs in Biomedicine* **108,** 600–616 (2012) (*pp.* 28, 56, 77, 79).

90. Lu, C.-Y., Jing, B.-Z., Chan, P. P., Xiang, D., Xie, W., Wang, J. & Yeung, D. S. *Vessel enhancement of low quality fundus image using mathematical morphology and combination of Gabor and matched filter* in *IEEE International Conference on Wavelet Analysis and Pattern Recognition* (2016), 168–173 (*p.* 28).

91. Chen, B., Chen, Y., Shao, Z. & Luo, L. *Retinal vessel enhancement using multi-dictionary and sparse coding* in *IEEE International Conference on Acoustics, Speech and Signal Processing* (2016), 893–897 (*pp.* 28, 56).

92. Sigurosson, E. M., Valero, S., Benediktsson, J. A., Chanussot, J., Talbot, H. & Stefansson, E. Automatic retinal vessel extraction based on directional mathematical morphology and fuzzy classification. *Pattern Recognition Letters* **47,** 164–171 (2014) (*pp.* 28–29, 56).

93. Lu, C.-Y., Jing, B.-Z., Chan, P. P., Xiang, D., Xie, W., Wang, J. & Yeung, D. S. *Vessel enhancement of low quality fundus image using mathematical morphology and combination of Gabor and matched filter* in *International Conference on Wavelet Analysis and Pattern Recognition* (2016), 168–173 (*pp.* 28–29, 56).

94. Merveille, O., Naegel, B., Talbot, H., Najman, L. & Passat, N. 2D filtering of curvilinear structures by ranking the orientation responses of path operators (RORPO). *Image Processing on Line* **7,** 246–261 (2017) (*pp.* 29, 108–109, 115).

95. Merveille, O., Talbot, H., Najman, L. & Passat, N. Curvilinear structure analysis by ranking the orientation responses of path operators. *IEEE Trans-*

actions on Pattern Analysis and Machine Intelligence **40,** 304–317 (2018) (*pp.* 29, 91, 112, 116).

96. Law, M. W. & Chung, A. C. Efficient implementation for spherical flux computation and its application to vascular segmentation. *IEEE Transactions on Image Processing* **18,** 596–612 (2009) (*p.* 29).

97. Rigamonti, R. & Lepetit, V. *Accurate and efficient linear structure segmentation by leveraging ad hoc features with learned filters* in *International Conference on Medical Image Computing and Computer-Assisted Intervention* (2012), 189–197 (*p.* 29).

98. Lam, B. S., Gao, Y. & Liew, A. W.-C. General retinal vessel segmentation using regularization-based multiconcavity modeling. *IEEE Transactions on Medical Imaging* **29,** 1369–1381 (2010) (*p.* 29).

99. Annunziata, R., Kheirkhah, A., Hamrah, P. & Trucco, E. *Boosting hand-crafted features for curvilinear structure segmentation by learning context filters* in *International Conference on Medical Image Computing and Computer-Assisted Intervention* (2015), 596–603 (*p.* 29).

100. Annunziata, R. & Trucco, E. Accelerating convolutional sparse coding for curvilinear structures segmentation by refining SCIRD-TS filter banks. *IEEE Transactions on Medical Imaging* **35,** 2381–2392 (2016) (*pp.* 29, 72, 77).

101. Grisan, E. *Boosted learned kernels for data-driven vesselness measure* in *Medical Imaging 2017: Biomedical Applications in Molecular, Structural, and Functional Imaging* (2017), 101370Z (*p.* 29).

102. Haralick, R. M., Sternberg, S. R. & Zhuang, X. Image analysis using mathematical morphology. *IEEE Transactions on Pattern Analysis and Machine Intelligence* **PAMI-9,** 532–550 (1987) (*pp.* 31–32, 34, 104).

103. Sidiropoulos, N. D., Baras, J. S. & Berenstein, C. A. Optimal filtering of digital binary images corrupted by union/intersection noise. *IEEE Transactions on Image Processing* **3,** 382–403 (1994) (*p.* 31).

104. Lantuejoul, C. *Sur le modele de Johnson-Mehl generalise* Internal Report 514 (Centre de Morphologie Mathématique, 1977) (*p.* 31).

105. Matheron, G. *Random Sets and Integral Geometry* (John Wiley & Sons, 1975) (*p.* 31).

106. Beucher, S. & Lantuejoul, C. *Use of watersheds in contour detection* in *International Workshop on Image Processing: Real-time Edge and Motion Detection/Estimation* (1979) (*p.* 31).

107. McLoughlin, N. *DR HAGIS* http://personalpages.manchester.ac.uk/staff/niall.p.mcloughlin. [Online; accessed 6-March-2019]. 2008 (*p.* 39).

108. Gonzalez, R. C. & Woods, R. E. *Digital Image Processing* 3rd edition (Prentice-Hall, Inc., 2006) (*p.* 38).

109. Bloomberg, D. S. & Maragos, P. *Generalized hit-miss operators* in *Image Algebra and Morphological Image Processing* **1350** (1990), 116–129 (*p.* 38).

110. Naegel, B., Passat, N. & Ronse, C. Grey-level hit-or-miss transforms—Part II: Application to angiographic image processing. *Pattern Recognition* **40,** 648–658 (2007) (*p.* 39).

111. Naegel, B., Passat, N. & Ronse, C. Grey-level hit-or-miss transforms—Part I: Unified theory. *Pattern Recognition* **40,** 635–647 (2007) (*p.* 39).

112. Khosravi, M. & Schafer, R. W. Template matching based on a grayscale hit-or-miss transform. *IEEE Transactions on image Processing* **5,** 1060–1066 (1996) (*p.* 39).

113. Schaefer, R. & Casasent, D. Nonlinear optical hit–miss transform for detection. *Applied optics* **34,** 3869–3882 (1995) (*p.* 39).

114. Raducanu, B. & Grana, M. *A grayscale hit-or-miss transform based on level sets* in *International Conference on Image Processing* **2** (2000), 931–933 (*p.* 39).

115. Wood, S. L., Qu, G. & Roloff, L. W. *Detection and labeling of retinal vessels for longitudinal studies* in *International Conference on Image Processing* **3** (1995), 164–167 (*p.* 39).

116. Mendonca, A. M. & Campilho, A. Segmentation of retinal blood vessels by combining the detection of centerlines and morphological reconstruction. *IEEE Transactions on Medical Imaging* **25,** 1200–1213 (2006) (*pp.* 40, 77, 79).

117. Figueiredo, M. A. & Leitao, J. M. A nonsmoothing approach to the estimation of vessel contours in angiograms. *IEEE Transactions on Medical Imaging* **14,** 162–172 (1995) (*p.* 40).

118. Eiho, S. & Qian, Y. *Detection of coronary artery tree using morphological operator* in *Computers in Cardiology* (1997), 525–528 (*p.* 40).

119. Donizelli, M. *Region-oriented segmentation of vascular structures from dsa images using mathematical morphology and binary region growing* in *Bildverarbeitung für die Medizin 1998* (Springer, 1998), 303–307 (*p.* 40).

120. Kottke, D. & Sun, Y. *Region splitting of medical images based upon bimodality analysis* in *International Conference of the IEEE Engineering in Medicine and Biology Society* (1990), 154–155 (*p.* 40).

121. Thackray, B. D. & Nelson, A. C. Semi-automatic segmentation of vascular network images using a rotating structuring element (ROSE) with mathematical morphology and dual feature thresholding. *IEEE Transactions on Medical Imaging* **12,** 385–392 (1993) (*p.* 40).

122. Fetita, C., Ortner, M., Brillet, P.-Y., Prêteux, F., Grenier, P. *et al. A morphological-aggregative approach for 3D segmentation of pulmonary airways from generic MSCT acquisitions* in *Proc. of Second International Workshop on Pulmonary Image Analysis* (2009), 215–226 (*p.* 40).

123. Fraz, M. M., Barman, S. A., Remagnino, P., Hoppe, A., Basit, A., Uyyanonvara, B., Rudnicka, A. R. & Owen, C. G. An approach to localize the retinal blood vessels using bit planes and centerline detection. *Computer methods and programs in biomedicine* **108,** 600–616 (2012) (*p.* 40).

124. Roychowdhury, S., Koozekanani, D. D. & Parhi, K. K. Iterative vessel segmentation of fundus images. *IEEE Transactions on Biomedical Engineering* **62,** 1738–1749 (2015) (*p.* 40).

125. Lo, P., Van Ginneken, B., Reinhardt, J. M., Yavarna, T., De Jong, P. A., Irving, B., Fetita, C., Ortner, M., Pinho, R. & Sijbers, J. Extraction of airways from CT. *IEEE Transactions on Medical Imaging* **31,** 2093–2107 (2012) (*p.* 42).

126. Rodriguez, A., Ehlenberger, D. B., Dickstein, D. L., Hof, P. R. & Wearne, S. L. Automated three-dimensional detection, shape classification of dendritic spines from fluorescence microscopy images. *PloS One* **3,** e1997 (2008) (*p.* 42).

127. Hadjidemetriou, S., Toomre, D. & Duncan, J. S. *Segmentation and 3D reconstruction of microtubules in total internal reflection fluorescence microscopy* in *Medical Image Computing and Computer-Assisted Intervention* (2005), 761–769 (*pp.* 42, 87).

128. Lesage, D., Angelini, E. D., Bloch, I. & Funka-Lea, G. A review of 3D vessel lumen segmentation techniques: Models, features and extraction schemes. *Medical Image Analysis* **13,** 819–845 (2009) (*p.* 42).

129. Hacihaliloglu, I., Abugharbieh, R., Hodgson, A. J. & Rohling, R. N. *Enhancement of bone surface visualization from 3D ultrasound based on local phase information* in *Ultrasonics Symposium* (2006), 21–24 (*pp.* 43, 106).

130. Saff, E. B. & Kuijlaars, A. B. Distributing many points on a sphere. *The Mathematical intelligencer* **19,** 5–11 (1997) (*p.* 44).

131. Koay, C. G. Analytically exact spiral scheme for generating uniformly distributed points on the unit sphere. *Journal of Computational Science* **2,** 88–91 (2011) (*pp.* 44, 90).

132. Kovesi, P. Image features from phase congruency. *Journal of Computer Vision Research* **1,** 1–26 (1999) (*pp.* 45–46).

133. Wang, W., Li, J., Huang, F. & Feng, H. Design and implementation of Log-Gabor filter in fingerprint image enhancement. *Pattern Recognition Letters* **29,** 301–308 (2008) (*p.* 45).

134. Ferrari, R. J., Allaire, S., Hope, A., Kim, J., Jaffray, D. & Pekar, V. Detection of point landmarks in 3D medical images via phase congruency model. *Journal of the Brazilian Computer Society* **17,** 117–132 (2011) (*p.* 46).

135. Fraz, M., Remagnino, P., Hoppe, A., Uyyanonvara, B., Rudnicka, A., Owen, C. & Barman, S. Blood vessel segmentation methodologies in retinal images – A survey. *Computer Methods and Programs in Biomedicine* **108,** 407–433 (2012) (*p.* 56).

136. Obara, B., Fricker, M. & Grau, V. *Coherence enhancing diffusion filtering based on the Phase Congruency Tensor* in *IEEE International Symposium on Biomedical Imaging* (2012), 202–205 (*pp.* 56, 121).

137. Feng, P., Pan, Y., Wei, B., Jin, W. & Mi, D. Enhancing retinal image by the Contourlet transform. *Pattern Recognition* **28,** 516–522 (2007) (*p.* 56).

138. Azzopardi, G. & Petkov, N. Automatic detection of vascular bifurcations in segmented retinal images using trainable COSFIRE filters. *Pattern Recognition Letters* **34,** 922–933 (2013) (*p.* 56).

139. Merveille, O., Talbot, H., Najman, L. & Passat, N. Curvilinear structure analysis by ranking the orientation responses of path operators. *IEEE Transactions on Pattern Analysis and Machine Intelligence* **40,** 304–317 (2018) (*p.* 56).

140. Nelson, C. *Mathematical Morphology for Quantification in Biological & Medical Image Analysis* PhD thesis (Durham University, 2017) (*pp.* 60–61).

141. The Mathworks, I. *MATLAB* www.mathworks.com. Massachusetts, USA, 2016 (*p.* 62).

142. Hoover, A., Kouznetsova, V. & Goldbaum, M. Locating blood vessels in retinal images by piecewise threshold probing of a matched filter response. *IEEE Transactions on Medical Imaging* **19,** 203–210 (2000) (*pp.* 70, 108).

143. Fawcett, T. An introduction to ROC analysis. *Pattern Recognition Letters* **27,** 861–874 (2006) (*pp.* 70, 108).

144. Otsu, N. A threshold selection method from gray-level histograms. *IEEE Transactions on Systems, Man, and Cybernetics* **9,** 62–66 (1979) (*pp.* 76–77).

145. Jiang, X. & Mojon, D. Adaptive local thresholding by verification-based multithreshold probing with application to vessel detection in retinal images. *IEEE Transactions on Pattern Analysis and Machine Intelligence* **25,** 131–137 (2003) (*pp.* 76–78).

146. Soares, J. V., Leandro, J. J., Cesar, R. M., Jelinek, H. F. & Cree, M. J. Retinal vessel segmentation using the 2-D Gabor wavelet and supervised classification. *IEEE Transactions on Medical Imaging* **25,** 1214–1222 (2006) (*pp.* 77, 79).

147. Lupascu, C. A., Tegolo, D. & Trucco, E. FABC: retinal vessel segmentation using AdaBoost. *IEEE Transactions on Information Technology in Biomedicine* **14,** 1267–1274 (2010) (*pp.* 77, 79).

148. You, X., Peng, Q., Yuan, Y., Cheung, Y.-m. & Lei, J. Segmentation of retinal blood vessels using the radial projection and semi-supervised approach. *Pattern Recognition* **44,** 2314–2324 (2011) (*pp.* 77, 79).

149. Marin, D., Aquino, A., Gegundez-Arias, M. E. & Bravo, J. M. A new supervised method for blood vessel segmentation in retinal images by using gray-

level and moment invariants-based features. *IEEE Transactions on Medical Imaging* **30,** 146–158 (2011) (*pp.* 77, 79).

150. Palomera-Perez, M. A., Martinez-Perez, M. E., Benitez-Perez, H. & Ortega-Arjona, J. L. Parallel multiscale feature extraction and region growing: application in retinal blood vessel detection. *IEEE Transactions on Information Technology in Biomedicine* **14,** 500–506 (2010) (*pp.* 77, 79).

151. Martinez-Perez, M. E., Hughes, A. D., Thom, S. A., Bharath, A. A. & Parker, K. H. Segmentation of blood vessels from red-free and fluorescein retinal images. *Medical Image Analysis* **11,** 47–61 (2007) (*pp.* 77, 79).

152. Al-Diri, B., Hunter, A. & Steel, D. An active contour model for segmenting and measuring retinal vessels. *IEEE Transactions on Medical Imaging* **28,** 1488–1497 (2009) (*pp.* 77, 79).

153. Azzopardi, G., Strisciuglio, N., Vento, M. & Petkov, N. Trainable COSFIRE filters for vessel delineation with application to retinal images. *Medical Image Analysis* **19,** 46–57 (2015) (*pp.* 77, 79).

154. Zhang, J., Dashtbozorg, B., Bekkers, E., Pluim, J. P., Duits, R. & ter Haar Romeny, B. M. Robust retinal vessel segmentation via locally adaptive derivative frames in orientation scores. *IEEE Transactions on Medical Imaging* **35,** 2631–2644 (2016) (*pp.* 77, 79).

155. Goldberg, D. *Genetic Algorithm in search Optimization and Machine Learing, Addison-WesleyPub* 1989 (*p.* 82).

156. Trzupek, M., Ogiela, M. R. & Tadeusiewicz, R. Intelligent image content semantic description for cardiac 3D visualisations. *Engineering Applications of Artificial Intelligence* **24,** 1410–1418 (2011) (*p.* 84).

157. Bijith, P. & Deepa, T. Image Enhancement and 3-D Reconstruction of Coronary Artery from Multiple Cardiac Angiograms. *Image* **6,** 10231–10236 (2017) (*p.* 87).

158. Hajian-Tilaki, K. Receiver operating characteristic (ROC) curve analysis for medical diagnostic test evaluation. *Caspian Journal of Internal Medicine* **4,** 627 (2013) (*p.* 91).

159. Hamarneh, G. & Jassi, P. VascuSynth: Simulating vascular trees for generating volumetric image data with ground truth segmentation and tree analysis. *Computerized Medical Imaging and Graphics* **34,** 605–616 (2010) (*pp.* 97–98).

160. Brown, K. M., Barrionuevo, G., Canty, A. J., De Paola, V., Hirsch, J. A., Jefferis, G. S., Lu, J., Snippe, M., Sugihara, I. & Ascoli, G. A. The DIADEM data sets: representative light microscopy images of neuronal morphology to advance automation of digital reconstructions. *Neuroinformatics* **9,** 143–157 (2011) (*p.* 99).

161. Ronse, C. & Heijmans, H. J. The algebraic basis of mathematical morphology: II. Openings and closings. *CVGIP: Image Understanding* **54,** 74–97 (1991) (*p.* 101).

162. Niemeijer, M., Staal, J., van Ginneken, B., Loog, M. & Abramoff, M. D. *Comparative study of retinal vessel segmentation methods on a new publicly available database* in *Image Processing in Medical Imaging* (2004), 648–657 (*p.* 108).

163. Hamarneh, G. & Jassi, P. VascuSynth: simulating vascular trees for generating volumetric image data with ground-truth segmentation and tree analysis. *Computerized Medical Imaging and Graphics* **34,** 605–616 (2010) (*p.* 111).

164. Maltoni, D., Maio, D., Jain, A. K. & Prabhakar, S. *Handbook of Fingerprint Recognition* (Springer Science & Business Media, 2009) (*p.* 115).

165. Gelasca, E. D., Byun, J., Obara, B. & Manjunath, B. *Evaluation and Benchmark for Biological Image Segmentation* in *IEEE International Conference on Image Processing* (2008), 1816–1819 (*p.* 116).